Theoretical Chemical Approaches for Molecular Spin Quantum Computers (分子スピン量子コンピュータに向けた理論化学的アプローチ)

理学研究科

物質分子系専攻

平成 27 年度

山本 悟

(Satoru Yamamoto)

Preface

This work has been carried out at Graduate School of Science, Osaka City University during the period of the 2010 - 2015 academic years under the supervision of Professor Kazunobu Sato and Professor Emeritus Takeji Takui. This doctoral thesis is presented by the author in partial fulfillment of the requirements of the Graduate School of Science for the Degree of Doctor of Science at Osaka City University.

Quantum computers (QCs) are one of the ultimate goals of quantum state control, which have capabilities to perform powerful computation procedure named quantum algorithm. Spectroscopy and quantum state control have deep relationship in simulations since both describe dynamics of quantum nature. Focusing on molecules, an electron magnetic resonance technique is a good representative of quantum computing by the virtue of electron and nuclear spins. In this thesis, the author has engaged in research molecular spin QCs (MSQCs) based on electron spin resonance-QCs (ESR-QCs), discussing magnetic properties of molecules and molecular spin dynamics theoretically.

After general introduction in chapter 1, chapter 2 describes the structural study of spin-labeled DNA duplexes toward Lloyd model QCs as one dimension (1D) spin chain QCs. Here, the author has determined the steric structures with conformational search techniques based on molecular mechanics (MM) calculations combined with the experiments of pulsed electron double resonance (ELDOR) measurements. As a result, the author has suggested that the four electron spins in the DNA analogue have a capacity to be controlled individually and positions of spin labels in DNA duplexes are significant toward the spin chain QCs. Therefore, MM calculations combined with ESR experiments are a powerful tool for QCs since the partial structures about spins can be determined with the help of experimental restrictions.

Research topics on theoretical chemistry for QCs include not only the structural study of molecules in static but also dynamic study of quantum properties. They also include theoretical supports of experimental procedures based on quantum mechanics in order to realize MSQC (chapters 3 and 4). In chapter 3, the author has proposed Adiabatic Quantum Computer (AQC) experiments for MSQCs. The most significant theoretical procedure is analytical decompositions in order to conquer pulse sequences, as experimental procedure of ESR-QCs, for the AQC experiments and subsequently the author has also performed numerical simulations to optimize algorithms for ESR experiments. As a result, the author figures out the difference of AQCs between ESR-QCs and nuclear magnetic resonance- (NMR-) QCs and proves that ESR-QCs can perform AQCs. In chapter 4, the author has investigated molecular design for applications of numerical pulses by GRadient Ascent Pulse Engineering (GRAPE) techniques. From the single-crystal studies of a potassium hydrogen maleate (KHM) radical and a ^{13}C- labeled malonyl radical, molecular design and suitable molecular

orientations are discussed for numerical pulses depending on spin magnetic parameters of the molecules. In the study, scalability of molecular spins is also proven with numerical simulations.

From a viewpoint of quantum computing, new quantum algorithms are desired to develop benefit of QCs. Recently, quantum chemical calculations on QCs (QCCs on QCs) have been developed into a new research area of quantum computing, which solve quantum chemical problems by QCs. In this thesis, the author has focused on the spin property of QCCs, and then proposed a new quantum algorithms to prepare configuration state functions (CSFs) as described in chapter 5. The quantum algorithm has a superpolynomial character, indicating information processing capacity which is exponentially faster than the fastest algorithm in classical computers (CCs). By applying the algorithm, there is a possibility that open-shell molecules can be efficiently treated same as closed-shell molecules in QCs despite not in CCs.

Through this doctoral thesis, the author contributes to theory of QCs in terms of the molecular system for MSQCs, proposing MSQC experiments of AQCs and GRAPE pulses and finding a new quantum algorithm. All the achievements in this work will be beneficial for the realization of the quantum computing and its experimental approach.

Contents

Chapter 3. Adiabatic Quantum Computing with Molecular Spin Quantum Computers (MSQCs)

Chapter 1

Introduction

Quantum mechanics tells us the ultimate goal of theoretical chemistry, in which complete computations of whole quantum systems derive any desired molecular feature in chemistry and physics. In my thesis, I have focused on the spin property of quantum nature in molecules since single electron/nuclear spin has the smallest degree of freedom in quantum mechanics and is conservation quantity in non-relativistic quantum theory. Although there is a simple single quantum property, the total molecular spins composed of those electron and nuclear spins (e.g. N of spin-1/2) have huge degrees of freedom (2^N) accompanying superposition and entangled states. Therefore, there are the significant applications "quantum computing" and "quantum state control".[1]

Nowadays, CCs have been essential not only theoreticians but also experimentalists due to the huge amount of data to investigate new science and to analyze experiments. Discussing the relation between information and physics, it is known that computational resources by an ensemble of atoms involved are limited[2] and the quantum feature has more capability in terms of computational ability than classical one. Quantum computing is a new paradigm, in which the superposition and entangled states of quantum bit (qubit) speed up processing.[1, 3] Mentioning computational ability of QCs, BQP (Bounded-error Quantum Polynomial time) class is known as the class which QC can solve in polynomial time against the problem size and contains some parts of NP (Non-deterministic Polynomial time) and NP-hard classes.[4] Since NP and NP-hard cannot be solved efficiently by CCs, there are several issues ought to be solved by QCs. The most interesting quantum algorithms (called superpolynomial algorithms) give the solutions of the NP and NP-hard in polynomial time[5] and the best known example is Shor's factorization algorithm[5]. In this algorithm, the solution of the factorization problem are given in polynomial time by QCs and the experiments have been invoked by (Nuclear Magnetic Resonance) NMR spin qubits[6], photonic qubits[7] and Josephson phase qubits resonators[8].

Toward QCs, many quantum systems have been proposed so far, e.g. Josephson junction qubits,[8, 9] photonic qubits,[7, 10] trapped ion,[11] NMR-QC,[5, 6, 12-19] ESR-QC,[20-25] and mixed systems in order to combine benefits of different qubits,[26] etc. Although quantum systems are struggling with decoherence (relaxation) and interaction problems, experiments for quantum state control and quantum algorithms are invoked in each system. In Josephson junction systems, interactions between qubits can be switched by external contact where charge, phase and flux qubits are proposed to control quantum states.[9] Furthermore, the system has experimented Shor's algorithms by nine qubits composed of four phase qubits and the two lowest sublevels of five superconducting co-planar waveguide (CPW) resonators[8]. Polarization qubits of photons have benefits in large decoherence time and spatial migration ability, thus quantum teleportation, switching interactions[27] and quantum algorithms[7, 10] have been investigated. In the trapped ion qubits systems, the quantum systems can contain many qubits (the current largest number is 14 qubits[28]), and Deutsch–Jozsa algorithms and quantum simulations[11] have also invoked.

Referring magnetic resonance QCs, NMR-QCs have been proven significant quantum algorithms with small qubit experiments, e.g. the first time experiments of Grover's quantum search algorithm,[12] quantum Fourier transformation,[13] Shor's algorithm,[6] adiabatic MAXCUT,[14] adiabatic Grover's algorithm[15] and adiabatic factorization of 21[16] and 143[17]. Note that the experiments of Shor's algorithm have been invoked by the NMR-QC utilizing C, H and F nuclear qubits of a dimethylfluoromalonate molecule with approximately 300 radio wave pulses.[6] Furthermore, state control with numerically computed pulses has been also experimented well by NMR spectrometers.[18, 19]

In MSQCs, molecular design for QCs is applicative from chemical point of view named *g*-tensor, pseudo *g*-tensor, *A*-tensor and *D*-tensor engineering and is interested in spectroscopy and the quantum state control, [20-25] and MSQCs have stronger interactions than NMR-QCs, which cover from order of MHz to few GHz[29]. For the earlier QC experiments, a spinor property of electron was proven by pulsed ENDOR spectroscopy,[30] A Diphenylnitroxide (DPNO) was utilized there for 3-qubit entangle experiments,[24] A nitroxide biradical was applied to perform a CNOT quantum gate,[23] and indirect state control of a hydrogen nuclear qubit was invoked with a single frequency microwave pulse[25]. Furthermore, theoretical research[31] has proven several issues to realize MSQCs including my work as described in the following chapters.[32]

Here, I introduce the earlier study and contents of each chapter. Chapter 2 is the study for periodic 1D-QCs composed of molecular spins, where triple-stranded metallo-helicates[21] and spin-labeled DNA duplexes[22] have been synthesized as models for Lloyd QCs before. Although I have studied spin-labeled DNA duplexes by virtue of the multi organic radical character in chapter 2, triple-stranded metal systems are also significant candidates of the periodic 1D-QCs in which spin sites are composed of metal ions of Mn(II) and Zn(II).[21] Lloyd model QCs[33] are one theoretical model of 1D-QCs and require individual spin operations at a periodical 3 type spins (A, B, C) and the edges of spin chain (E1, E2) to control whole spin chain. In the Lloyd model, it is proven that the QCs can be performed only with 16 pulses in an NMR case study, which number is conserved in any spin number of chains.[34] Toward Lloyd model QCs, I have focused on the steric structures of a spin-labeled DNA duplex which is composed of two radical pairwise and one DNA duplex, and the DNA duplex synthesized was characterized well by CD spectra and DNA melting point in the previous study.[22] In chapter 2, I have determined the steric structures of the spin-labeled DNA duplex by MM calculations with the help of the pulsed ELDOR technique, where the ELDOR experiments were utilized to estimate possible steric structures of the DNA duplex and the spin sites.

In chapter 3, I have proven that MSQCs have a computational ability to perform a quantum computational model for AQCs and described practical steps by calculating pulse sequences.[32] In AQCs, Hamiltonian is slowly varied in time and its ground states is computed by the change. One of the significant AQC experiments is adiabatic factorization algorithm of 21 by an NMR-QC which has

computed nuclear spins of a diethylfluoromalonate molecule with analytical pulse sequences.[16] Furthermore, the algorithm has the simulating parts of a 3-qubit interaction obviously hard to be represented by existent physical systems. As a result, this algorithm requires computational ability to perform AQCs for the general manner. In the adiabatic factorization algorithm of 21, time evolution of the adiabatic quantum algorithm (AQUA) was simulated by 3 nuclear spin qubits (H, C and F) in an analytical manner. Thus, I have applied the same approach to MSQCs in order to perform AQCs. For 3 qubit systems of MSQCs mainly discussed in chapter 3, a phtalocyanine derivative[35] and a deuterated glutacon acid radical[36] are selected to perform the AQUA with 3 electron qubits and 1 electron and 2 nuclear qubits, respectively. In chapter 2, the most parts are devoted for the analytical pulse sequence generation techniques where secular averaging approach (SAA) is adopted to discuss pulse sequences[31] and simulating procedure of quantum path is described in MSQCs for the first time. Furthermore, I have pointed out the difference between NMR-QCs and MSQCs and proposed the modification methods of experimental conditions for MSQCs by numerical simulations. As a result, I have established theoretical perspective on MSQCs toward quantum simulations of time evolution and AQCs.

In chapter 4, numerical pulse sequences are discussed for quantum gate operations. Recently, GRadient Ascent Pulse Engineering (GRAPE) techniques have been widely utilized in NMR-QCs by virtue of the accurate control and overcoming hard analytical control conditions, where the approach optimized pulse amplitude with fixed frequency in a global manner in time.[18] I reveal the relation between molecular properties of MSQCs and quantum state control by the GRAPE techniques. Simulations to estimate control difficulty have been performed by changing molecular orientations against the static magnetic field, and the following control is assumed: nuclear spins are controlled by irradiations of microwave via hyperfine interactions between electrons and nuclei, i.e. indirect state control of nuclei.[25] A KHM radical[37] and a ^{13}C- labeled malonyl radical[38] are adopted for controlled spin systems hosting one electron spin and two nuclear spins. As a result, the control difficulty is proven by controllability of the spin systems such as distinguishability of qubits and nuclear spin flip speed through hyperfine interactions. This is the first study to establish the relation between molecular properties and numerical pulse experiments.

The last chapter, chapter 5, is concerned with a quantum algorithm study for QCCs on QCs. I have established a quantum algorithm to generate a configuration state function (CSF) in a quantum register, which is the one of the superpolynomial algorithms. The CSF wavefunction has a multi-determinant property composed of exponential number of Slater determinants to satisfy a spin eigenstate. This property suggests that the CSF requires exponential time to compute in classical computers in general. However, QCs have computational capacity to generate CSFs in polynomial time by a discovered quantum algorithm in gate model QCs. The quantum algorithm suggests that open-shell molecules can be treated by a same manner with closed-shell molecules, and also offers a new starting point of QCCs.

As described above, the research area in my thesis ranges only in theory but wide: A molecular structural study (chapter 2), a pulse sequence study in ESR spectroscopy (chapter 3), a molecular design study with numerical pulses (chapter 4) and a quantum algorithm study (chapter 5). The details are shown in each chapter. Due to my research, new fundamental properties in MSQCs are concluded and few further problems are discovered.

References

[1] M. A. Nielsen and I. L. Chuang, *Quantum Computation and Quantum Information*, Cambridge University Press, **2000**.

[2] R. W. Keyes, *Rep. Prog. Phys.*, **2005**, *68*, 2701-2746; S. Lloyd, *Nature*, **2000**, *406*, 1047-1054; C.Bennett, E. Bernstein, G. Brassard and U. Vazirani, *SIAM J. Comput.*, **1997**, *26*, 1510–1523; S. Aaronson, *ACM SIGACT News*, **2005**, *36*, 30–52.

[3] R. P. Feynman, *Int. J. Theor. Phys*., **1982**, *21*, 467–488.

[4] D. Bacon and W. van Dam, *COMMUN. ACM*., **2010**, *53*, 84-93; A. Gepp and P. Stocks, *GENET PROGRAM EVOL M*, **2009**, *10*, 181-228.

[5] P. W. Shor, *SIAM J.Sci.Statist.Comput.*, **1997**, *26*, 1484-1509.

[6] L. M. K. Vandersypen, M. Steffen, G. Breyta, C. S. Yannoni, M. H. Sherwood, I. L. Chuang, *Nature*, **2001**, *414*, 883-887.

[7] C-Y. Lu, D. E. Browne, T. Yang and J-W. Pan, *Phys. Rev. Lett.*, **2007**, *99*, 250504; B. P. Lanyon, T. J. Weinhold, N. K. Langford, M. Barbieri, D. F. V. James, A. Gilchrist and A. G. White, *Phys. Rev. Lett.*, **2007**, *99*, 250505; A. Politi, J. C. F. Matthews and J. L. O'Brien, *Science*, **2009**, *325*, 1221; E. L. A. Martine-Lopez, T. Lawson, X. Q. Zhou and J. L. O'Brien, *Nature Photon*, **2012**, *6*, 773-776.

[8] E. Lucero, R. Barends, Y. Chen, J. Kelly, M. Mariantoni, A. Megrant, P. O'Malley, D. Sank, A. Vainsencher, J. Wenner, T. White, Y. Yin, A. N. Cleland, John M. Martinis, *Nature Phys.*, **2012**, *8*, 719-723.

[9] Y. Makhlin, G. Schön, A. Shnirman, *Rev. Mod. Phys*., **2001**, *73*, 357; Y. Nakamura, Y. A. Pashkin, J. S. Tsai, *Nature*, **1999**, *398*, 786-788.

[10] S. Barz, E. Kashefi, A. Broadbent, J. F. Fitzsimons, A. Zeilinger, P. Walther, *Science*, **2012**, *335*, 303-308.

[11] S. Gulde, M. Riebe, G. P. T. Lancaster, C. Becher, J. Eschner, H. Häffner, F. Schmidt-Kaler, I. L. Chuang, R. Blatt, *Nature*, **2003**, *421*, 48-50; B. P. Lanyon, C. Hempel, D. Nigg, M. Muller, R. Gerritsma, F. Zahringer, P. Schindier, J. T. Barreiro, M. Rambach, G. Kirchmair, M. Hennrich, P. Zoller, R. Blatt, C. F. Roos, *Science*, **2011**, *334*, 57-61; J. T. Barreiro, M. Muller, P. Schindler, D. Nigg, T. Monz, M. Chwalla, M. Hennrich, C. F. Roos, P. Zoller, R. Blatt, *Nature*, **2011**, *470*, 486-491.

[12] I. L. Chuang, N. Gershenfeld, and M. Kubinec, *Phys. Rev. Lett.* **1998**, *80*, 3408-3411; J. A. Jones, M. Mosca, and R. H. Hansen, *Nature*, **1998**, *393*, 344-346.

[13] Y. S. Weinstein, M. A. Pravia, E. M. Fortunato, S. Lloyd, and D. G. Cory, *Phys. Rev. Lett*., **2001**, *86*, 1889-1891.

[14] M. Steffen, W. van Dam, T. Hogg, G. Breyta, I. Chuang, *Phys. Rev. Lett.* **2003**, *90*, 067903.

[15] A. Mitra, A. Ghosh, R. Das, A. Patel, A. Kumar, *J. Magn. Reson*. **2005**, *177*, 285.

[16] X.-H. Peng, Z. Liao, N. Xu, G. Qin, X. Zhou, D. Suter and J. Du, *Phys. Rev. Lett.*, **2008**, *101*, 220405.

[17] N. Xu, J. Zhu, D. Lu, X. Zhou, X. Peng, J. Du, *Phys. Rev. Lett*. **2012**, *108*, 130501.

[18] N. Khaneja, T. Reiss, C. Kehlet, T. Schulte-Herbrüggen, and S. J. Glaser, *J. Magn. Reson*., **2005**, *172*. 296-305.

[19] Z. Wu, J. Li, W. Zheng, J. Luo, M. Feng, and X. Peng, *Phys. Rev. A*, **2011**, *84*, 042312.

[20] G. A. Timco, S. Carretta, F. Troiani, F. Tuna, R. J. Pritchard, C. A. Muryn, E. J. L. McInnes, A. Ghirri, A. Candini, P. Santini, G. Amoretti, M. Affronte and R. E. P. Winpenny, *Nat. Nanotechnol*. **2009**, *4*, 173-178.

[21] Y. Morita, Y. Yakiyama, S. Nakazawa, T. Murata, T. Ise, D. Hashizume, D. Shiomi, K. Sato, M. Kitagawa, K. Nakasuji and T. Takui, *J. Am. Chem. Soc*., **2010**, *132*, 6944-6946.

[22] H. Atsumi, K. Maekawa, S. Nakazawa, D. Shiomi, K. Sato, M. Kitagawa, T. Takui and K. Nakatani, *Chem. Eur. J*., **2012**, *18*, 178-183; H. Atsumi, S. Nakazawa, C. Dohno, K. Sato, T. Takui and K. Nakatani, *Chem. Commun*., **2013**, *49*, 6370-6372.

[23] S. Nakazawa, S. Nishida, T. Ise, T. Yoshino, N. Mori, R. Rahimi, K. Sato, Y. Morita, K. Toyota, D. Shiomi, M. Kitagawa, H. Hara, P. Carl, P. Höfer and T. Takui, *Angew. Chem. Int. Ed.*, **2012**, *51*, 9860-9864.

[24] T. Yoshino, S. Nishida, K. Sato, S. Nakazawa, R. D. Rahimi, K. Toyota, D. Shiomi, Y. Morita, M. Kitagawa and T. Takui, *J. Phys. Chem. Lett*., **2011**, *2*, 449-453.

[25] J. S. Hodges, J. C. Yang, C. Ramanathan, D. G. Cory, *Phys. Rev. A.*, **2008**, *78*, 010303.

[26] G. Vallone, G. Donati, R. Ceccalli, P. Mataloni, *Phys. Rev. A*., **2010**, *81*, 052301; P. Rabi, P. Zoller, *Phys. Rev. A*., **2007**, *76*, 042308; X. Zhu, Y. W. Zhu, S. Murali, M. D. Stollers, R. S. Ruoff, *Nature*, **2011**, *478*, 221-224; X. Zhu, S. Saito, A. Kemp, K. Kakuyanagi, S. Karimoto, H. Nakano, W. J. Munro,Y. Tokura, M. S. Everitt, K. Nemoto, M. Kasu, N. Mizuochi, K. Semba, *Nature*, **2011**, *478*, 221-224; D. Kim, Z. Shi, C. B. Simmons, D. R. Ward, J. R. Prance, T. S. Koh, J. K. Gamble, D. E. Savage, M. G. Lagally, M. Friesen, S. N. Coppersmith, M. A. Eriksson, *Nature*, **2014**, *511*, 70-74.

[27] X. Zou, J. Shu, G. Guo, *Phys. Rev. A*., **2006**, *73*, 054301.

[28] T. Monz, P. Schindler, J. T. Barreiro, M. Chwalla, D. Nigg, W. A. Coish, M. Harlander, W. Haensel, M. Hennrich, R. Blatt, *Phys. Rev. Lett*., **2011**, *106*, 130506.

[29] S. Suzuki, T. Furui, M. Kuratsu, M. Kozaki, D. Shiomi, K. Sato, T. Takui, K. Okada, *J. Am. Chem. Soc*., **2010**, *132*, 15908-15910.

[30] K. Sato, S. Nakazawa, R. Rahimi, T. Ise, S. Nishida, T. Yoshino, N. Mori, K. Toyota, D. Shiomi, Y. Yakiyama, Y. Morita, M. Kitagawa, K. Nakasuji, M. Nakahara, H. Hara, P. Carl, P. Höfer and T. Takui, *J. Mater. Chem*., **2009**, *19*, 3739-3754.

[31] *OBJECT-ORIENTED MAGNETIC RESONANCE; Classes and Objects, Calculations and Computations*, eds. M. Mehring and V. A. Weberruss, ACADEMIC PRESS, San Diego, **2001**.

[32] S. Yamamoto, S. Nakazawa, K. Sugisaki, K. Sato, K. Toyota, D. Shiomi, T. Takui, *Phys. Chem. Chem. Phys.*, **2015**, *17*, 2742-2749.

[33] S. Lloyd, *Science*, **1993**, *261*, 1569–1571; S. Lloyd, *Sci. Am.*, **1995**, *73*, 140–145.

[34] Y. Kawano, S. Yamashita, M. Kitagawa, *Phys. Rev. A*, **2005**, *72*, 012301.

[35] A. G. M. Barrett, G. R. Hanson, A. J. P. White, D. J. Williams and A. S. Micallef, *Tetrahedron*., **2007**, *63*, 5244-5250.

[36] H. R. Falle and M. A. WhiteheaA, *Can. J. Chem*., **1972**, *50*, 139-151; C. Heller and T. Cole. *J. Chem. Phys*., **1962**, *37*,243-250; L. Thomas and T. Srikrishan, *J. Chem. Crystallogr*., **2003**, *33*, 689-693; Y. Atalay, D. Avci and A. Basoglu, *J. Mol. Struct.*, **2006**, *787*, 90-95.

[37] S. F. Darlow and W. Cochran, *Acta Cryst.*, **1961**, *14*, 1250-1257.

[38] D. K. Park, G. Feng, R. Rahimi, S. Labruyère, T. Shibata, S. Nakazawa, K. Sato, T. Takui, R. Laflamme, and J. Baugh, *Quantum Inf. Process*., **2015**, *14*, 2435-2461.

Chapter 2

Structure Determination of Spin-labeled DNA Duplexes by Pulsed ELDOR Experiments and Molecular Mechanics Calculations

2-1. Introduction

DNA has been attracting researchers from its salient biological character of life,[1] but the structural features itself, i.e. the duplex well-known as a hydrogen bonding architecture and a 1D structure has also interests for chemists and physicists. Since 1D structures of DNAs can be applied to chemical modification of spin sources, DNA duplexes have been proposed to utilize periodic 1D QCs especially for Lloyd model QCs.[2-4] In the research, the electron spin sources are attached and assumed to be controlled by pulsed ESR, i.e. MSQCs are assumed.[5-7] This is the salient example of molecular designs toward electron spin-based quantum computing and quantum information processing (QC/QIP).[2-7]

Lloyd model QCs are composed of the 1D $(ABC)_n$ spin array and have a computational ability of 3n qubit systems, where the individual spin manipulations are required only for grouped spins of A, B and C and the edge spins of the 1D chain.[8] Since the individual manipulations in ESR-QCs are possible with the *g*-tensor and pseudo *g*-tensor engineering technique, which controls *g*-value and the transition frequency of the spin system by the molecular engineering.[6, 7] It is remarkably proven that universal gates, including all performable quantum operations, are possible to be performed only by 16 pulses for the 1D spin array at the NMR case study.[9]

At spin functionalized materials such as synthesized oligonucleotides, information of the structural properties is a key to the multi-qubit systems: structural flexibility of the system, orientations of spin moieties, hydrogen binding structures.[4] It is not feasible to obtain single crystals for synthesized oligonucleotides enough good ingredient to determine their structures by X-ray analyses particularly with high flexibility. Frequently, the structures should be determined by indirect experiments and theoretical calculations. In this chapter, I have invoked conformational search calculations of MM in order to determine the optimal structures with the help of the ELDOR experiments.

Molecular Mechanics is one of the theoretical structure calculation methods on chemistry, which is based on classical mechanics with given empirical parameter sets of force fields. The largest benefit is the computational speed enough to calculate energy of large molecules. However, MM calculations face an avoidable problem in determining flexible structures of oligonucleotides because there are many local minima in energy originated from the degree of freedom in atoms.

The problem seems to be critical for simulating structures around global minima, but it is still possible to acquire the structures by combining the MM calculations (Merk Molecular Force Field: MMFF)[10] with experimental information observed in ESR. Pulsed ELDOR experiment is known as one of the most reliable distance measurements to determine the spin distance about 1.5-8.0 nm between two weakly coupled unpaired electrons.[11] Pulsed ELDOR technique (PELDOR) has been widely used for the distance measurements of weakly coupled bi/tri-radicals, spin-labeled macromolecules and clusters.[12] The distance analyses of ELDOR spectra have been performed by

using DeerAnalysis 2006[13] and DEFit program packages[14], and the error of distance distributions can be estimated from the experimental data by the later program.

In addition to conformational search procedure of MM calculations, Molecular dynamics (MD) simulations[15] have been very widely used for the folded RNAs and DNAs to study the conformational structures, dynamics and thermodynamics with the help of PELDOR.[16] However, both approach should simulate same results in static structures since steric structures are time independent physical existence. Thus, I discuss only the conformational search method for the structure determination of the spin-labeled DNA duplex.

2-2. Molecular Information

2-2-1. Molecular Structures of a Spin-labeled DNA Duplex

The non-covalent type of a spin-labeled DNA duplex (D1/D2) is aimed at a Lloyd model QC, in which two pairs of stable radical moieties are labeled. The structures of D1/D2 are composed of a 22-mer duplex (D1 = 5'-GTCTC (G) GTAGACATTC (A) GTTAG-3' and D2 = 5'-CTAAC (A) GAATGTCTAC (G) GAGAC-3') and G and A in brackets denote mismatch bases as reported before.[3] The radical moieties are 2,2,6,6-tetramethylpiperidine (TEMPO) and nitronyl nitroxide (NN) which bonds to the predetermined sites with mismatch binding ligands (MBLs). A naphyridine-azaquinolone (NA) with TEMPO and a naphthyridine carbamate dimer (NCD) with NN are designated as MBLs selectively bonding with the hydrogen manner to the guanine-guanine (G-G) mismatch in a 5'-CGG-3'/5'-CGG-3' (CGG) partial peptide and the adenine-adenine (A-A) mismatch in a 5'-CAG-3'/5'-CAG-3' partial peptide, respectively (Fig. 2-2.1).[3] The moieties are named NCD-NN and NA-TEMPO and the four radical moieties in attached sites are numbered by NN(1), NN(2), TEMPO(3) and TEMPO(4).

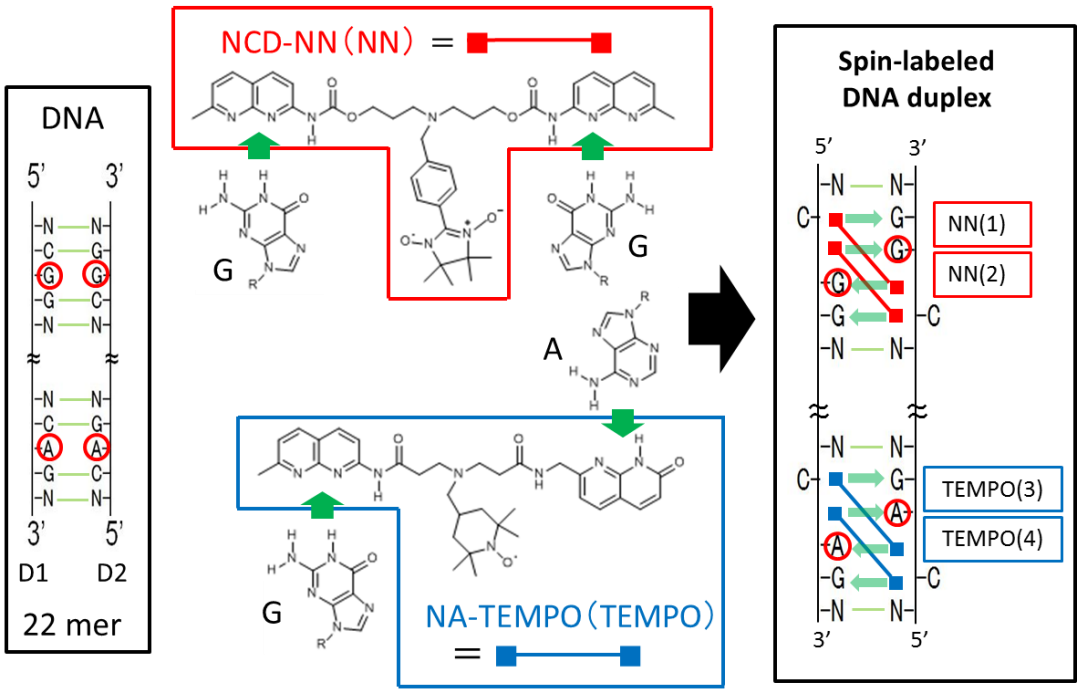

Figure 2-2.1. A molecular structure of a 22-mer DNA duplex labeled with four-spin moieties. The DNA and radical pairwise (two NCD-NN and two NA-TEMPO) in the left hand and middle sides compose a spin-labeled DNA duplex of the right hand side. Red-circles depicted in both DNA duplexes indicate mismatched bases. Green allows and lines are hydrogen bonds, and allows denote hydrogen bonds between spin-labels and DNA bases around the two mismatched sites.

2-2-2. Steric Structures around Spin-labels

As shown in Fig. 2-2.1, the synthesized spin-labeled DNA duplex has two types of spin distances expected by the molecular structure since the two radical pairwise are attached distant mismatch bases (10 DNA bases) and each pair of spin labels is attached in neighbor DNA bases. One of them is the short spin distance between each pair of radical moieties (intra-pairs), and another is the longer distance between radical pairs (inter-pairs) than that of intra-pairs. The *g*-tensor and pseudo *g*-tensor engineering has completed for the 1D chain since two radical pairs are estimated to have different *g*-tensors and the different transition frequencies in the chemical point of view.[6, 7] In this spin-labeled DNA duplex, there are only two spin sources to be aligned, and it is possible to expand same method toward three qubit cyclic chain, i.e. Lloyd model QCs.

2-3. ESR Experiments

2-3-1. Experimental Conditions of ESR Spectroscopy

Four-pulse ELDOR (PELDOR/DEER) experiments of the spin-labeled DNA duplex were performed in frozen solution of the toluene solvent at 50 K. The spectra were observed with a made-to-order Bruker ELEXSYS E580 pulsed Q-band ESR spectrometer equipped with a helium cryostat (made-to-order Optibath SXM) and a temperature control system (ITC 503) both from Oxford Instruments amplified via a pulsed traveling wave tube (1kW TWT) amplifier from Applied Systems Engineering.

2-3-2. Pulsed ELDOR Spectra

The pulse sequence in the ELDOR spectroscopy is $\pi/2(\nu_1)$-τ_1-$\pi(\nu_1)$-(τ_1+t)- $\pi(\nu_2)$-(τ_2-t)- $\pi(\nu_1)$- τ_2-echo (Fig. 2-3.1). In the ELDOR experiments, pulse duration time and pulse interval time are carefully selected in terms of selectivity of spins and relaxation effects. The pulse conditions are follows: the durations of the detection pulses (ν_1) were set to be 16 ns for the $\pi/2$ pulse at the center of the resonator dip and the duration of the pump pulse (ν_2) was set to be 80 ns and applied at 50 MHz lower frequency than that of the detection pulses, which is applied to the maximum at the nitroxide-based field-swept ESR spectra. The visual positions of the detection and pump pulses are indicated in Fig. 2-3.2. In the time conditions, time t was varied 256 points with the increments Δt of 8 ns, and τ_1 and τ_2 were set to be 200 ns and 2000 ns, respectively. The experiment repetition time of 1 ms is adopted for the accumulation as the time of the system enough relaxed. Accumulating of 80000 scans, the overall measurement time was done in 5.6 h.

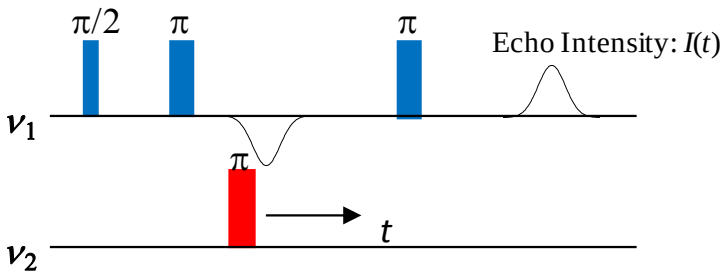

Figure 2-3.1. Pulse sequence of 4-pulse ELDOR experiments. The microwave frequency in the detection pulse is ν_1 and that in the pump pulse is ν_2.

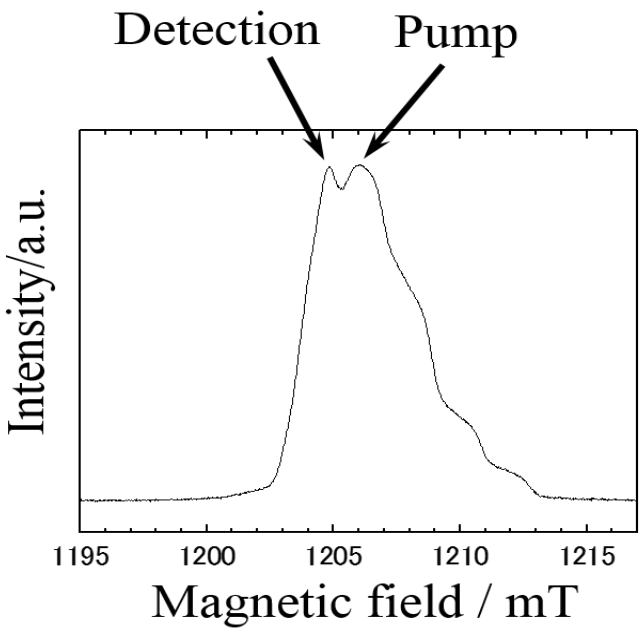

Figure 2-3.2. Field-swept ESR experiments. Positions of pump and detection pulses are shown with respect to the magnetic field.

2-3-3. Analyses of ELDOR Experiments

Experimental data were analyzed for spin distance distributions from the time domain spectra by two methods. One is DeerAnalysis2006 with Tikhonov regularization in the range of 1.6 and 8 nm using a regularization parameter of 1.[13] Another is DEFit program software developed by P. G. Fajer and coworkers,[14] which can estimate not only the distance distributions but the error rates of the distributions. Considering these results, I have determined the spin distances with reliability.

2-4. Theory of Molecular Mechanics

2-4-1. Optimization Procedure

The steric structures of the spin-labeled DNA duplexes are determined by the continuous conformational search based on MM calculations from the estimated initial structures. The structural energy is estimated by MMFF[10] with water solvent (GB/SA model)[17]. Since MMFF does not have force field parameters for radical moieties, the radical NO sites were replaced with CO. It has been reported that the CO group is suitable for the replacement of the NO group from the viewpoint of the hydrogen bonding form.[18] To my knowledge, NO and CO groups have a similarity in the crystal structures for deuterated host-guest systems, therefore the replacement are appropriate.[6]

The conformational search procedure is composed of three processes, creations of new structures, structure optimizations and sequential conformational searches. In the structure optimization process, TNCG (Truncated Newton Conjugate Gradient) method is utilized on the basis of nonlinear optimization procedure and the end of the optimization process is judged by the energy change being lower than 0.1 kJ/mol per one step.[19] An optimized structure is determined to be a new structure when RMSD (Root-Mean-Squares Deviation) as measure of the average distance between two relevant structures is within 1.0 Å. All the MM calculations were performed in Macromodel 9.8/Maestro 9.1 and 9.4.[20]

2-4-2. Conformational Search

The simulations of the continuous conformational searches were performed by using a large-scale-low mode sampling (LLMOD),[21] torsional sampling (MCMM; Monte Carlo Multiple Minimum) and a MMFF and MMFFs re-optimization process.[22] At the conformational search procedure, LLMOD and MCMM are applied to the lowest energy structure in order to pick up 10 searched structures with energy low. The re-optimization process is performed in order to relax energy of the 10 searched structures with two force field, which is sequential optimization to find the lowest energy structure: 1) optimize with MMFFs force field into the MMFF optimized structure and 2) a re-optimization with MMFF force field into the MMFFs before optimized one. Therefore, the re-optimization process certainly comes to the next to LLMOD and MCMM processes. The overall processes are performed to the initial structure for a kind of each type, e.g. Type X.

At the 1st step of the conformational search, (1) LLMOD, MCMM and the re-optimization were applied to the initial structure of Type X, say X_i, in which the hydrogen bonds were constrained. The 1st step was repeated unless the new lowest energy structure found. (2) The 2nd step is the conformational search utilizing the lowest energy structure of the 1st step without constraining hydrogen bonds. In the re-optimization of this 2nd step, we abandoned the structures in which the

hydrogen bonds between the spin-labeling units and the bases in the DNA duplex are completely cleaved. The 2nd process was also repeated unless the new lowest energy structure was found. (3) In the 3rd step, LLMOD and MCMM with MMFF were applied to the lowest energy structure of the 2nd step, in which the hydrogen bonds were not constrained in all the conformational search. This process was not repeated, giving the most stable structure optimized for a kind of type, say X_f.

2-5. Results of ELDOR Experiments

2-5-1. ELDOR Analyses by DeerAnalysis 2006

The time domain profile was obtained by the ELDOR experiments for the spin-labeled DNA duplex described above. In DeerAnalysis 2006,[13] the time domain profile is analyzed into the distance distributions between two unpaired spins, with Fourier transformation and Tikhonov regularization. Several separated peaks range from 2.5 nm to 6.3 nm, where the most intense peak appears at 4.36 nm (see Fig. 2-5.1). The best fit for the Fourier transformed spectrum was given by the superposition of eight Gaussian functions with particular weights. The details of fitted distance distributions are listed in Table 2-5.1.

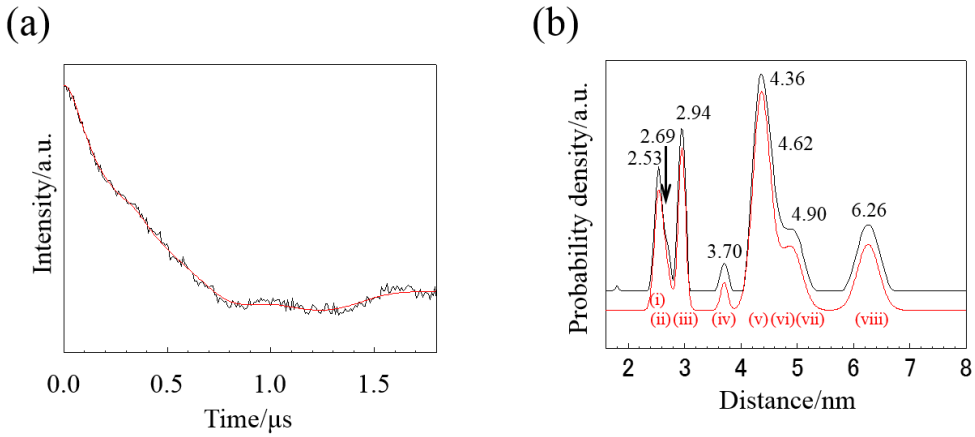

Figure 2-5.1. (a) Time domain profile of PELDOR measurements subtracted background by DeerAnalysis 2006. (b) Spin distance distributions with Tikhonov regularization (black line) and fitting (red line) composed of eight Gaussian functions. The Gaussian weights are shown in Table 2-5.1.

Table 2-5.1. Peak distances and weights of eight Gaussians. The peak numbers (i)-(viii) in the table corresponds to Fig. 2-5.1 (b). Peak weights are relative values given in %.

	(i)	(ii)	(iii)	(iv)	(v)	(vi)	(vii)	(viii)
Distance /nm	2.53	2.69	2.94	3.70	4.36	4.62	4.90	6.26
Intensity /%	8.95	5.01	12.61	2.16	37.57	6.71	11.60	15.39

2-5-2. ELDOR Analyses by DEFit

DEFit program[14] supplied by P. G. Fajer and coworkers enables to estimate distance distributions with error rates of each distribution from a time domain profile of ELDOR experiments. The analysis of error rates is based on the fitting arbitrary property, and then a number of Gaussian functions are

automatically estimated from change of error rates. Furthermore, reliability of each distance distribution is also evaluated as plots of error in χ^2 analysis. The analysis plots χ^2 values by changing the peak distance and width. If the counter plots of error were narrow (broad), the distribution is reliable (non-reliable) due to the small (large) arbitrary properties (distance and width) to fit the ELDOR experiments.

The results are shown in Fig. 2-5.2 accompanying three distributions, in which the errors for distributions of 2.0-3.5 nm and 6.0-7.0 nm were relatively larger than that of 4.3 nm, and the narrow and intense contour plots are given rise to around 4.3 nm. The results imply that the peak of 4.3 nm is the most reliable and major component of ELDOR experiments.

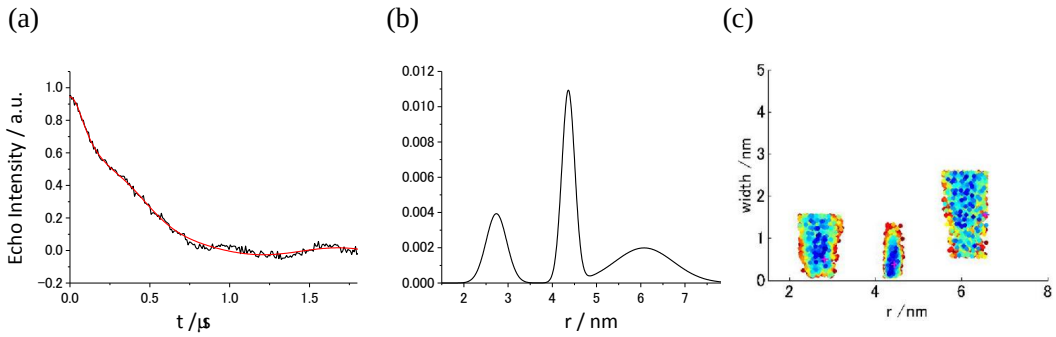

Figure 2-5.2. Analysis of PELDOR signals by DEFit program. (a) Time domain profile subtracted background (black line) and the best fit curve (red line). (b) The distance distributions in DEFit analysis with respect to the best fit curve. (c) Error in χ^2 analysis.

2-5-3. ELDOR Results

With the two analyses, DeerAnalysis 2006 and DEFit program, the ELDOR experiments are transformed into the distance distributions and error information. Both programs give approximately same distributions except for the peaks below 3.5 nm. In DEFit program, the peak below 3.5 nm has large error rate and the further Gaussian functions are not required because of small change of the error rates. Thus, I just mention only for possibility of the steric structures giving the peak below 3.5 nm which appears in DeerAnalysis 2006 results.

On the other hand, the peaks at 4.3 nm and around 6.0 nm are well consisted within the two analyses. These results suggest that there are the steric structures satisfying each distribution although the distribution around 6.0 nm has a non-negligible error rate. Therefore I have specially concentrated on the structures in which spin distances are about 4.3 nm (major), and also searched the structures with the spin distances around 6.0 nm (minor). From the structural point of view, those are corresponding to the spin distances between radicals of inter-pairs because distances between spin-labels are close enough to interact with the direct steric repulsion.

2-6. Structure Estimation

2-6-1. Scope of Simulated Structure

For the initial structures of the spin-labeled DNA duplex, I have elaborately considered the steric structures with different coordination of radical moieties as depicted in Fig. 2-2.1, in which each radical site (a ball) is inside/outside the DNA duplex and the hydrogen binding ligand (a dotted line) is bonded to the designated DNA bases.

The structural components of ELDOR results (section 2-5.) are estimated with the assumption from the molecular configurations based on steric repulsion. The steric structure neighboring the each radical pair-wise satisfies one of the three conditions: (1) a structure of the pair-wise radical in which one of hydrogen bonding sites is located inside the DNA duplex and the other located outside the DNA duplex, (2) a structure of the pair-wise radical in which both hydrogen bonding sites and radical sites are located inside the DNA duplex, (3) a structure of the pair-wise radical in which all the radical sites and hydrogen bonding sites of the radical moieties are located outside the DNA duplex. Then, I have sixteen types of structures as schematically shown in Fig. 2-6.1.

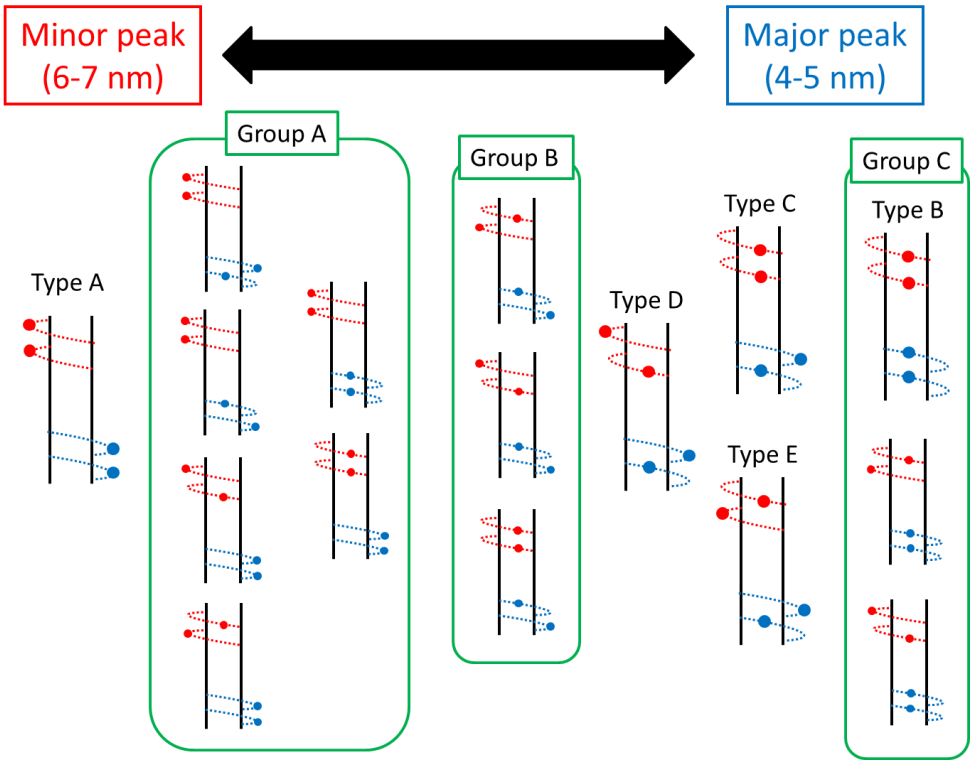

Figure 2-6.1. Schematic drawing of molecular structures of the spin-labeled DNA duplex. Red and blue dotted lines with circles denote the spin-labels of NCD-NN and NA-TEMPO, respectively. Circles designate spin sources in spin-label moieties. Group A, B and C in green boxes are named on the basis of spin distance estimations. For following discussion, Type A to E are named. See the detail in section 2-7.

2-6-2. Computed Structures

As discussed in the following subsection, the steric structures of the spin-labeled DNA duplex are estimated by the ELDOR measurements with optimized structures of MM calculations. The ELDOR experiments make restrictions for spin distances between the NN site and TEMPO site (inter-pairs), since distances between same radicals are too short to discuss two ELDOR peaks of 4-5 nm (major) and 6-7 nm (minor). From the view point of optimized/conformational searched structures (see section 2-7), 1) the structures of Type A in Fig. 2-6.1 have spin distances around 6-7 nm (minor peak of ELDOR measurements), and 2) the structures of Type B, C and D have spin distances around 4-5 nm (major peak). Where the simulated average spin distances, say simply spin distances, of the MM structures are defined as the distances between the oxygen atoms of the CO and NO groups.

Then, structures of Group A, B and C in Fig. 2-6.1 can be abandoned from the candidates of the steric structures. Group A and B are eliminated by restrictions from the distance distributions of the ELDOR experiments, and Group C can safely be eliminated by the large steric repulsions between the NA-TEMPO radical sites. In Group A, the structures should have spin distances longer than the major peak and shorter than the minor peak. These structures can be rejected from the ELDOR experiments since there are no peak between 5 nm and 6 nm. Group B can also be eliminated from the fact that the radical sites of NA-TEMPO(4) are located outside the DNA duplex and then the corresponding spin distances increase from the case of NA-TEMPO(3). Thus, the structures in Group B have also larger spin distances than that of the major peak. For Group C, the high steric repulsion between the NA-TEMPO radical sites is expected as described in the following section. This is also described below that the spin distances of Type E can be estimated from Type D and they have no consistency with the ELDOR experiments. Therefore, the probable candidates from the conformational search are limited in Type A, C and D.

2-7. Results of Conformational Search

2-7-1. Structures of Type A

Structures of Type A have the longest distance between the spin moieties, in which the hydrogen bonding sites, ligand parts of spin-labels, are located inside the DNA duplex and the radical sites are placed outside the DNA duplex. This type of structures was constructed based on the synthesis and experiments that the structure of molecule inserted DNA was determined by the NMR analyses,[2] which corresponds to the 22-mer DNA duplex with the inserted linker (NCD or NA) without the radical moieties. Thus, I carefully attached radical moieties to the linker with the structure kept as it was. The initial and final (conformational searched) structures, A_i and A_f, of Type A are depicted in Fig. 2-7.1. The energy of A_f is −46016 kJ mol^{-1} and the corresponding spin distances between inter-pairs are 6.0 to 7.0 nm (see Table 2-7.1). As a result, I assigned Type A into the minor ELDOR peak of (viii) in Fig. 2-7.2. Since each NN/TEMPO spin sites stick out the opposite directions of the DNA duplexes in A_i and A_f, the spin distances of inter-pairs are maximized.

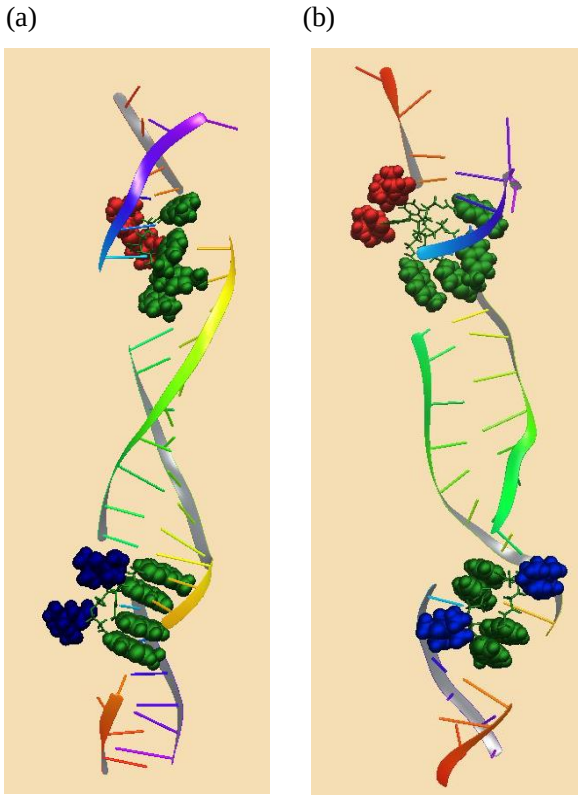

Figure 2-7.1. Computational structures of Type A. Green spheres depict hydrogen bonding sites of spin-labels and red and blue spheres are the radical sites (NNs and TEMPOs) of NCD-NN and NA-TEMPO, respectively. (a) The initial structure A_i (Energy = −45870 kJ mol^{-1}). (b) The final structure A_f (Energy = −46016 kJ mol^{-1}) of the MM searched structure.

Table 2-7.1. Energy and spin distances of A_i and A_f. The energy and distances are given in units of kJ mol^{-1} and nm, respectively. Circled number (*i*) denotes the spin moieties of NN(*i*) in *i* = 1, 2 and TEMPO(*i*) in *i* = 3, 4.

	Energy /kJ mol^{-1}	(1)-(2) / nm	(1)-(3) /nm	(1)-(4) /nm	(2)-(3) /nm	(2)-(4) /nm	(3)-(4) /nm
A_i	-45870	0.72	6.07	6.56	5.87	6.43	1.78
A_f	−46016	0.62	6.15	6.54	6.45	6.94	1.83

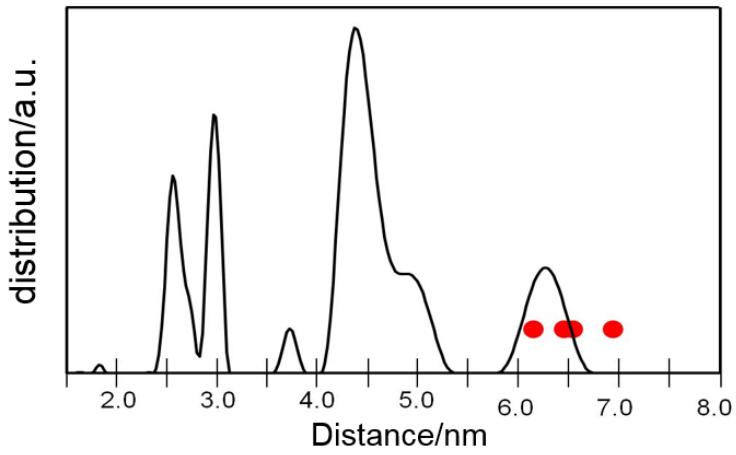

Figure 2-7.2. Distance distributions and spin distances of A_f. The spin distances between four spin-labels are shown in red filled circles. The distances corresponds a minor peak about 6.0 to 7.0 nm.

2-7-2. Structures of Type B and C

In order to construct structures with the shortest spin distances, I suggested a new concept of structures. Structures of Type B are consisted with all the hydrogen bonding sites are outside the DNA duplex and all the radical sites inside the DNA duplex. However, Type B has relatively higher energy than Type A, since the structure, e.g. the initial structure (B_i) in Fig. 2-7.3, has large steric repulsion around the radical sites of NNs. Compared to NCD-NN, NA-TEMPO has a bulky spin moiety close to NA ligand, and then this repulsion is estimated to make steric energy high in B_i. Although the spin distances are well corresponded to the major peaks (v)-(vii) of ELDOR experiments, I rejected Type B from the element of ELDOR distance distributions without searching its conformations due to the steric repulsion.

The relaxation of a sizable amount of the steric repulsions in Type B led Type C, which was constructed by modifying Type B, i.e. the radical site of TEMPO(3) was relocated outside the DNA

duplex. Resulting the conformational search from the initial structure of C_i, a final structure of C_f as the most energetically stable structure is obtained. The structures of C_i and C_f are depicted in Fig. 2-7.4 and the spin distances and energies are shown in Table 2-7.2. The spin distances in Type C correspond to the major peaks of ELDOR experiments (v)-(vii) (Fig. 2-7.5), and the relative energy of C_f is slightly smaller than that of A_f. Therefore, I suggest that Type C has contributions to the ELDOR spectra.

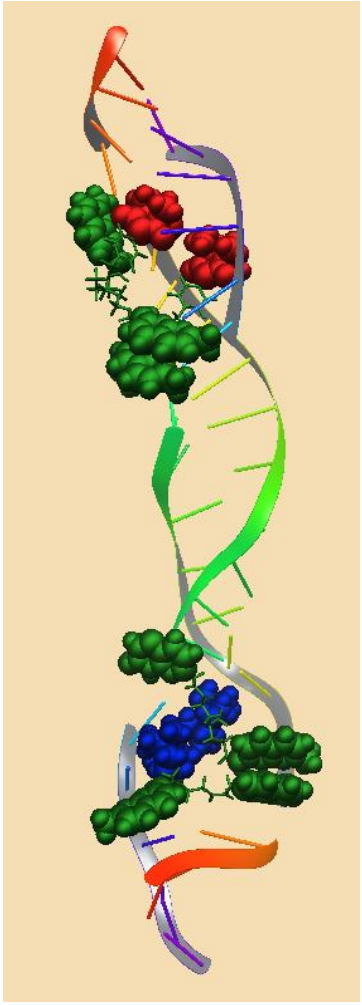

Figure 2-7.3. Computational structures of the initial structure B_i (Energy = −45753 kJ mol^{-1}). Green spheres depict hydrogen bonding sites of spin-labels and red and blue spheres are the radical sites (NNs and TEMPOs) of NCD-NN and NA-TEMPO, respectively.

(a) (b)

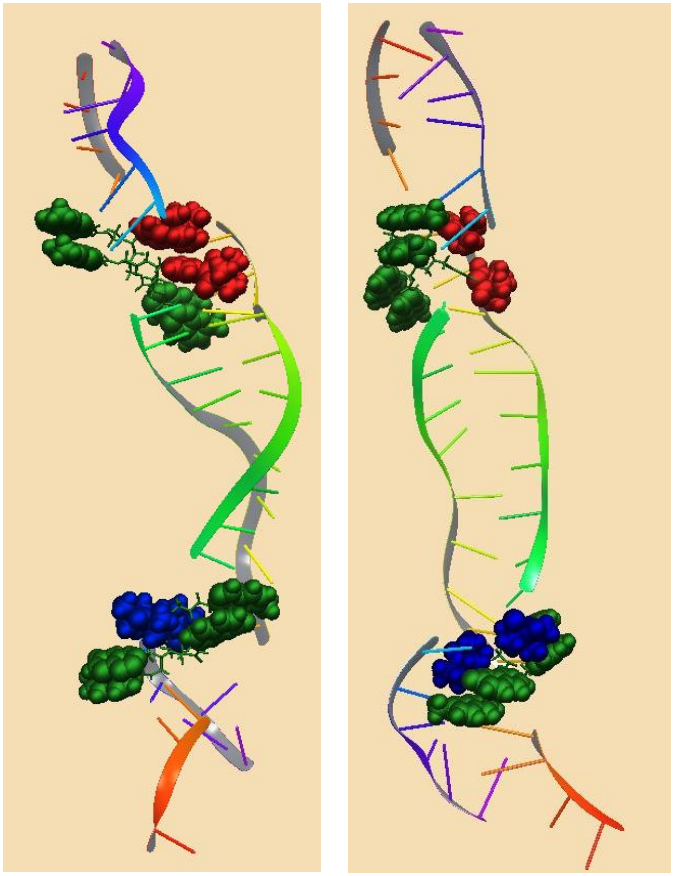

Figure 2-7.4. Computational structures of Type C. Green spheres depict hydrogen bonding sites of spin-labels and red and blue spheres are the radical sites (NNs and TEMPOs) of NCD-NN and NA-TEMPO, respectively. (a) The initial structure C_i (Energy = −45895 kJ mol^{-1}). (b) The final structure C_f (Energy = −46059 kJ mol^{-1}) of the MM searched structure.

Table 2-7.2. Energy and spin distances of C_i and C_f. The energy and distances are given in units of kJ mol^{-1} and nm, respectively. Circled number (*i*) denotes the spin moieties of NN(*i*) in *i* = 1, 2 and TEMPO(*i*) in *i* = 3, 4.

	Energy /kJ mol^{-1}	(1)-(2) / nm	(1)-(3) /nm	(1)-(4) /nm	(2)-(3) /nm	(2)-(4) /nm	(3)-(4) /nm
C_i	-45895	0.80	4.73	4.77	4.22	4.25	1.42
C_f	−46059	0.86	5.22	5.35	4.58	4.71	1.45

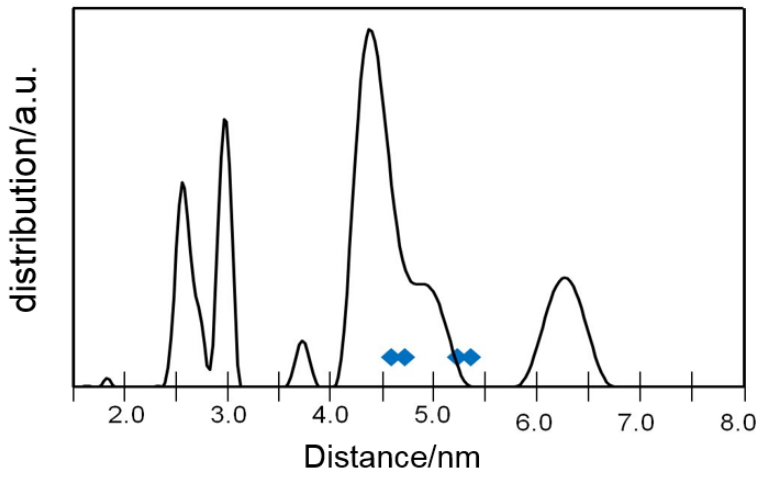

Figure 2-7.5. Distance distributions and spin distances of C_f. The spin distances between four spin-labels are shown in blue filled circles. The distances corresponds a major peak about 5.0 nm.

2-7-3. Structures of Type D and E

In order to estimate the steric repulsion between the NN spin sites, the structure of Type D was constructed, in which not only one of TEMPO(3) but also one of NN(1) were located outside the DNA duplex. From the conformational search, a final structure D_f was obtained from the initial structure D_i (Fig. 2-7.6 and Table 2-7.3). It is note worth that the spin distances of D_f are also corresponding to the peaks (v)-(vii) and the energy of D_f is almost the same as C_f and lower than that of A_f.

As mentioned in section 2.6, Type E was also considered as a steric structure of the spin-labeled DNA duplex, which radical sites of TEMPO(3) and NN(2) were located outside the DNA duplex. Figure 2-7.7 shows the structure of E_i, and Table 2-7.4 energy and spin distances. Although spin distances in Type E consistent with the major ELDOR peaks of (v)-(vii), there are also spin distances between inter-pairs, which can range uncertain and minor peaks (< 3.5 nm). This short distances are not included in Type C and D because in general NN(2) is closer to TEMPOs than NN(1). Therefore, I abandoned Type E as not the major structure consisting ELDOR distance distributions, since the structure in maximum is considered to be contained only as much as minor components. Thus, if Type E exists in the spin-labeled DNA duplex, the structures can contribute to the small amount of major peak of the ELDOR measurements.

(a) (b)

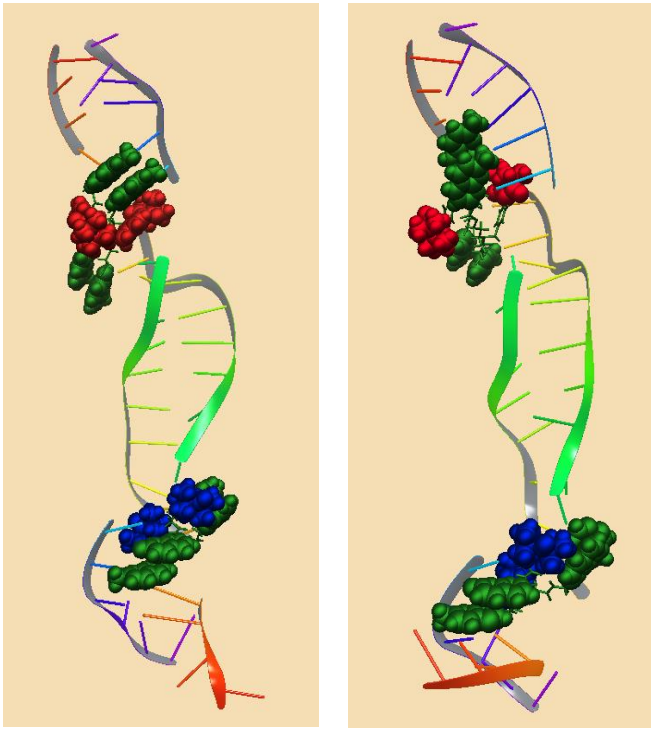

Figure 2-7.6. Computational structures of Type D. Green spheres depict hydrogen bonding sites of spin-labels and red and blue spheres are the radical sites (NNs and TEMPOs) of NCD-NN and NA-TEMPO, respectively. (a) The initial structure D_i (Energy = −45825 kJ mol^{-1}). (b) The final structure D_f (Energy = −46057 kJ mol^{-1}) of the MM searched structure.

.

Table 2-7.3. Energy and spin distances of D_i and D_f. The energy and distances are given in units of kJ mol^{-1} and nm, respectively. Circled number (*i*) denotes the spin moieties of NN(*i*) in *i* = 1, 2 and TEMPO(*i*) in *i* = 3, 4.

	Energy /kJ mol^{-1}	(1)-(2) / nm	(1)-(3) /nm	(1)-(4) /nm	(2)-(3) /nm	(2)-(4) /nm	(3)-(4) /nm
D_i	−45825	1.37	4.17	4.25	4.54	4.58	1.42
D_f	−46057	1.21	4.66	4.70	5.13	5.19	1.58

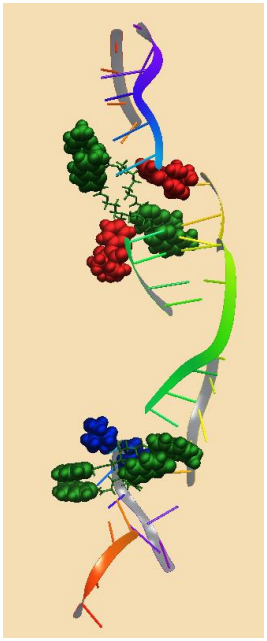

Figure 2-7.7. Computational structures of the initial structure E_i (Energy = −45859 kJ mol^{-1}). Green spheres depict hydrogen bonding sites of spin-labels and red and blue spheres are the radical sites (NNs and TEMPOs) of NCD-NN and NA-TEMPO, respectively.

Table 2-7.4. Energy and spin distances of E_i. The energy and distances are given in units of kJ mol^{-1} and nm, respectively. Circled number (*i*) denotes the spin moieties of NN(*i*) in *i* = 1, 2 and TEMPO(*i*) in *i* = 3, 4.

	Energy /kJ mol^{-1}	(1)-(2) / nm	(1)-(3) /nm	(1)-(4) /nm	(2)-(3) /nm	(2)-(4) /nm	(3)-(4) /nm
E_i	−45859	1.65	4.31	4.68	2.88	3.37	1.05

2-8. Discussion

By conformational search procedure, all the simulated structures are consistent with the PELDOR distance distributions (Type A to E, see section 2-7), and the abandoned structures of B_i and E_i have higher energy than the conformational searched structures and the short distance distributions. However, spin distances of E_i have a possibility to correspond the minor peaks below 4 nm and major peaks as described in subsection 2-7-3. Here, I discuss the energy and spin distances of A_f, C_f and D_f with Fig. 2-8.1, in which the energy and spin distances of B_i and E_i are depicted for reference. Energy of the structure A_f is higher as compared to those of C_f and D_f, and this energetic stability can explain the relatively intensity of major peaks (v)-(vii) and minor peak (viii) in Fig.2-5.1. In comparison with C_f and D_f, the energy difference is small enough, therefore I concluded that the structures C_f and D_f are the most stable ones simulated by the MM calculations.

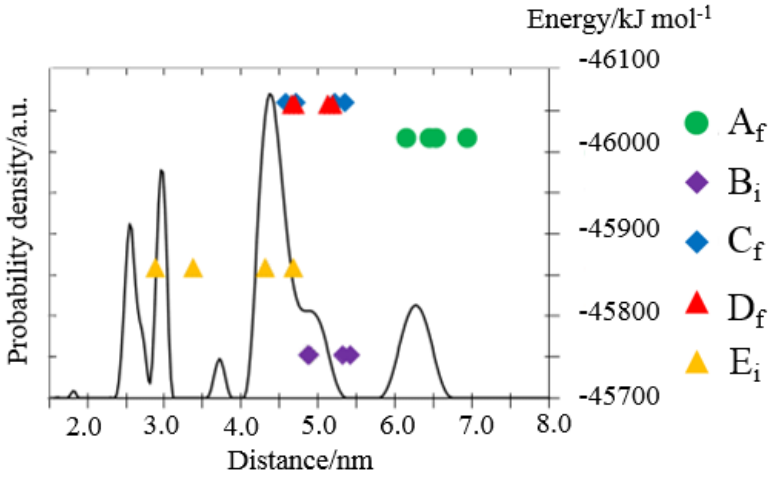

Table 2-8.1. Energy and spin distances of the strucutres of A_f, C_f, B_i, D_f. and E_i. The energy and distances are given in units of kJ mol^{-1} and nm, respectively.

The energy analysis for the structures of A_f, C_f and D_f is invoked in order to discuss the steric effects from the energetic point of view (Table 2-8.1). The principal differences are found in the solvent and electrostatic terms (> 1000 kJ mol^{-1}) related in charge distributions and surface areas, respectively. As these terms reflect the global steric differences, the conformation between them have significant difference, and the flexible DNA duplexes appear at solvent and electrostatic properties. This is also confirmed that the bonding energies of A_f, C_f and D_f are nearly the same (the difference is lower than 70 kJ mol^{-1}).

Toward molecular spin based QC/QIP systems, the accurate alignment of 1D periodicity is the most significant key. The ultimate goal of *g*-, *A*- and *D*-tensor engineering is to match tensors at the real system by the molecular design. For Lloyd model QC, the results suggest that the keys are: 1) attachment sites of spin-labels at the duplex in terms of the direction of radical moieties and 2) local structures of DNA duplex and spin-labels in terms of rigidity and orientations of the radical-pairwise.

Table 2-8.1. Energetic analyses of searched structures. Bonding terms are the sum of energy of covalent bonds. The energy is given in units of kJ mol^{-1}.

	Bonding /kJ mol^{-1}	van der Waals /kJ mol^{-1}	Electrostatic /kJ mol^{-1}	Solvent /kJ mol^{-1}	Total /kJ mol^{-1}
A_f	5825	4310	10729	−66880	−46016
C_f	5888	4383	11413	−67744	−46059
D_f	5867	4311	12689	−68926	−46057

2-9. Conclusions

The MM simulations of the 22-mer DNA duplex oligonucleotide equipped with the four electron spin moieties were carried out with the help of pulsed ELDOR spectroscopy. Two kinds of analyses of ELDOR experiments suggest two reliable peaks, i.e. major peaks (v)-(vii) in 4-5 nm and minor peak (viii) around 6.0 nm. In the MM simulations, I carefully considered 16 structures of the spin-labeled patterns which are different enough not to search by automatic calculations, and focused on structures corresponding to major and minor peaks.

The continuous conformational searches were performed to the selected three initial structures A_i, C_i and D_i representative of Type A, C and D, respectively. Those structures are composed of the different spin-label positions: all the spin sites are outside the DNA duplex for Type A, only TEMPO(3) locates outside the DNA duplex and the others are inside the DNA duplex for Type C and TEMPO(3) and NN(1) locate outside the DNA duplex and the others are inside the DNA duplex for Type D. The conformational searched structures of Type A, A_f, has spin distances of inter-pairs corresponding the minor peak (viii) of ELDOR experiments. Therefore, I conclude Type A is a minor steric structure of the spin-labeled DNA duplex. The major distributions (v)-(vii) are supplied by Type C and D, where the final structures of C_f and D_f have lower energy than that of A_f. This is because the spin sites of two radical pair-wise stick out to the opposite in Type A, then the spin distances decreased in Type C and D.

Detail analyses are performed in terms of energetic properties. Type A, C and D have large differences in solvent and electrostatic (non-bonding) terms reflecting their global structures. At the bonding energy of them, the difference is much smaller than non-bonding terms based on the flexibility of the DNA systems.

Focusing on local structures around the spin-labels, the orientations of spin sites are important for QC/QIP. The direction control of spin-labels is one of the remained problem for synthesis since *g* tensor engineering for Lloyd model QCs are strongly depending on the accurate alignment of the 1D systems. Fortunately, the spin-labeled DNA system has all radical moieties with the different direction, then the system can be utilized for four spin systems at least.

In summary, I have studied the structures of the spin-labeled DNA duplex based on MM calculations. The MM calculations combined with the PELDOR experiments have successfully suggested and supplied the structure information. As a result, the directions of the two attached radical units are different, therefore the system can be utilized for four spin system. It indicates that the subtle *g*-tensor engineering between the units is established.

2-10. References

[1] N. C. Seeman, *Nature*, **2003**, *421*, 427-431; E. Braun, Y. Eichen, U. Sivan and G. Ben-Yoseph, *Nature*, **1998**, *391*, 775-778; G. P. Mitchell, C. A. Mirkin and R. L. Letsinger, *J. Am. Chem. Soc*., **1999**, *121*, 8122-8123; J. J. Storhoff, A. A. Lazarides, R. C. Mucic, C. A. Mirkin, R. L. Letsinger and G. C. Schatz, *J. Am. Chem. Soc*., **2000**, *122*, 4640-4650.

[2] K. Nakatani, S. Hagihara, Y. Goto, A. Kobori, M. Hagihara, G. Hayashi, M. Kyo, M. Nomura, M. Mishima and C. Kojima, *Nat. Chem. Biol*., **2005**, *1*, 39-43; M. Nomura, S. Hagihara, Y. Goto, K. Nakatani and C. Kojima, *Nucleic Acids Res. Suppl*., **2005**, *49*, 213-214.

[3] H. Atsumi, K. Maekawa, S. Nakazawa, D. Shiomi, K. Sato, M. Kitagawa, T. Takui and K. Nakatani, *Chem. Eur. J*., **2012**, *18*, 178-183.

[4] H. Atsumi, S. Nakazawa, C. Dohno, K. Sato, T. Takui and K. Nakatani, *Chem. Commun*., **2013**, *49*, 6370-6372.

[5] G. A. Timco, S. Carretta, F. Troiani, F. Tuna, R. J. Pritchard, C. A. Muryn, E. J. L. McInnes, A. Ghirri, A. Candini, P. Santini, G. Amoretti, M. Affronte and R. E. P. Winpenny, *Nat. Nanotechnol*. **2009**, *4*, 173-178; K. Sato, S. Nakazawa, R. Rahimi, T. Ise, S. Nishida, T. Yoshino, N. Mori, K. Toyota, D. Shiomi, Y. Yakiyama, Y. Morita, M. Kitagawa, K. Nakasuji, M. Nakahara, H. Hara, P. Carl, P. Höfer and T. Takui, *J. Mater. Chem*., **2009**, *19*, 3739-3754; J. S. Hodges, J. C. Yang, C. Ramanathan, D. G. Cory, *Phys. Rev. A.*, **2008**, *78*, 010303.

[6] T. Yoshino, S. Nishida, K. Sato, S. Nakazawa, R. D. Rahimi, K. Toyota, D. Shiomi, Y. Morita, M. Kitagawa and T. Takui, *J. Phys. Chem. Lett*., **2011**, *2*, 449-453; S. Nakazawa, S. Nishida, T. Ise, T. Yoshino, N. Mori, R. Rahimi, K. Sato, Y. Morita, K. Toyota, D. Shiomi, M. Kitagawa, H. Hara, P. Carl, P. Höfer and T. Takui, *Angew. Chem. Int. Ed.*, **2012**, *51*, 9860-9864.

[7] Y. Morita, Y. Yakiyama, S. Nakazawa, T. Murata, T. Ise, D. Hashizume, D. Shiomi, K. Sato, M. Kitagawa, K. Nakasuji and T. Takui, *J. Am. Chem. Soc*., **2010**, *132*, 6944-6946

[8] S. Lloyd, *Science*, **1993**, *261*, 1569-1571; S. Lloyd, *Sci. Am.*, **1995**, *73*, 140-145.

[9] Y. Kawano, S. Yamashita, M. Kitagawa, *Phys. Rev. A*, **2005**, *72*, 012301.

[10] T. A. Halgren, *J. Comput. Chem*., **1996**, *17*, 490-519; T. A. Halgren, *J. Comput. Chem*., **1996**, *17*, 520-552; T. A. Halgren, *J. Comput. Chem.*, **1996**, *17*, 553-586; T. A. Halgren, *J. Comput. Chem*., **1996**, *17*, 587-615; T. A. Halgren, *J. Comput. Chem*., **1996**, *17*, 616-641; T. A. Halgren, *J. Comput. Chem.*, **1999**, *20*, 720-729; T. A. Halgren, *J. Comput. Chem*., **1999**, *20*, 730-748.

[11] Y. D. Tsvetkov, A. D. Milov and A. G. Maryasov, *Russ. Chem. Rev.*, **2008**, *77*, 487-520.

[12] *Distance measurements in biological systems by EPR; Biological magnetic resonance, Vol. 19*, eds. L. J. Berliner, G. R. Eaton and S. S. Eaton, Kluwer, New York, **2000**; G. Sicoli, F. Wachowius, M. Bennati and C. Höbartner, *Angew. Chem. Int. Ed.*, **2010**, *49*, 6443-6447; D. Margraf, P. Cekan, T.F. Prisner, S. Th. Sigurdsson and O. Schiemann, *Phys. Chem. Chem. Phys*., **2009**, *11*, 6708-

6714; B. E. Bode, D. Margraf, J. Plackmeyer, G. Drner, T. F. Prisner and O. Schiemann, *J. Am. Chem. Soc.*, **2007**, *129*, 6736-6745; Ye. Polyhach, A. Godt, C. Bauer and G. Jeschke, *J. Magn. Reson.*, **2006**, *185*, 118-129.

[13] G. Jeschke, V. Chechik, P. Ionita, A. Godt, H. Zimmermann, J. Banham, C. R. Timmel, D. Hilger and H. Jung, *Appl. Mag. Res*., **2006**, *30*, 473-498.

[14] K. I. Sen, T. M. Logan and P. G. Fajer, Biochemistry, **2007**, *46*, 11639-11649.

[15] T. Schlick, R. Collepardo-Guevara, L. A. Halvorson, S. Jung and X. Xiao, *Q. Rev. Biol*., **2011**, *44*, 191-228; G. W. S. C. Holn, M. V. Chubynsky, H. W. de Hann, A. Dube, K. Grass, O. A. Hickey, C. Kingsburry, D. Sean, T. N. Shendruk and L. X. Nhan, *Electrophoresis*, **2009**, *30*, 792-818; T. E. Cheatham III, *Annu. Rev. Phys. Chem*., **2000**, *51*, 435-471.

[16] H. Yu, Y. Mu, L. Nordenskiöld and G. Stock, *J. Chem. Theory. Comput*., **2008**, *4*, 1718-1787; O. Schiemann, N. Piton, Y. Mu, G. Stock, J. W. Engels and T. F. Prisner, *J. Am. Chem. Soc.*, **2004**, *126*, 5722-5729; O. Schiemann, P. Gekan, D. Margraf, T. F. Prisner and S. T. Sigurdsson, *Angew. Chem. Int. Ed*., **2009**, *48*, 3292-3295; G. Sicoli, G. Mathis, S. Aci-Sèche, C. Saint-Pierre, Y. Boulard, D. Gasparutto and S. Gambarelli, *Nucleic Acids Res*., **2009**, *37*, 3165-3176; E. A. Price, B. T. Sutch, Q. Cai, P. Z. Qin and I. S. Haworth, *Biopolymers*, **2007**, *87*, 40-50.

[17] W. C. Still, A. Tempczyk, R. C. Hawley and T. Hendrickson, *J. Am. Chem. Soc*., **1990**, *112*, 6127-6129; A. Cheng, S. A. Best, K. M. Jr. Merz and C. H. Reynolds, J. *Mol. Graphics Model*., **2000**, *18*, 273-282.

[18] D. Hartmann, R. Philipp, K. Schmadel, J. J. Birktoft, L. J. Banaszak and W. E. Trommer, *Biochemistry*, **1991**, *30*, 2782-2790.

[19] J. W. Ponder and F. M. Richards, *J. Comput. Chem*., **1987**, *8*, 1016-1024.

[20] *MacroModel, version 9.8, Schrödinger, LLC, New York, NY, 2010; Maestro, version 9.1, Schrödinger, LLC, New York, NY,* **2010***; Maestro, version 9.4, Schrödinger, LLC, New York, NY,* **2013**.

[21] G. M. Keseru and I. Kolossváry, *J. Am. Chem. Soc.*, **2001**, *123*, 12708-12709.

[22] G. Chang, W. C. Guida and W. C. Still, *J. Am. Chem. Soc*., **1989**, *111*, 4379-4386; M. Saunders, K. N. Houk, Y.-D. Wu, C. W. Still, M. Lipton, G. Chang and W. C. Guida, *J. Am. Chem. Soc*., **1990**, *112*, 1419-1427.

Chapter 3

Adiabatic Quantum Computing with Molecular Spin Quantum Computers (MSQCs)

3-1. Introduction

Recently, quantum state control has been the major subject of quantum science, and one of the ultimate goals is the quantum computing requiring full control of the subspace for the quantum states. In mathematics and physics, controllability of quantum systems is considered as a basic framework of quantum mechanics in Lie algebra representation.[1-3] Although fundamental theory of controllability can answer the problem whether the quantum system can be controlled or not, the concrete procedure how to control the system are not given.[2, 3] Therefore, to figure out the concrete approach is essential for achieving quantum state control by both analytical and numerical techniques. In this chapter, I introduce an analytical technique to perform adiabatic quantum computing by MSQCs (ESR-QCs).[4] A numerical state control technique for ESR is discussed with GRAPE methods[5] in chapter 4.

As described in introduction of my thesis (chapter 1), Shor's factorization algorithm encouraged the quantum computing field,[6] and the adiabatic factorization algorithms[7, 8] have general aspects of adiabatic quantum computing. In magnetic resonance QCs, the concrete control procedure is given in the forms of pulse sequences. Since the standard QCs are achievable only with the pulse sequences of CNOT gates and single spin rotations such as $\pi/8$ pulses,[1] the all analytical pulse sequences of MSQCs for standard QCs have already proposed by the work of M. Yu. Volkov and K. M. Salikhov.[9] However, there are alternative QC models to the standard QCs, i.e. AQC,[10] one-way QC,[11] etc.[12] AQC is one of the quantum computer/quantum computation models of QCs, which performs the ground state control based on adiabatic theorem and has not been investigated theoretically in MSQCs before.[10]

In NMR-QCs, adiabatic factorization algorithms have been experimented for composite number 21[7] and 143[8]. Although NMR/ESR systems cannot change the Hamiltonian themselves, those systems can perform AQC by simulating the time evolution operator. In this work, I derived analytical pulse sequences of AQCs controlled by ESR spectrometers for the first time. The SAA was applied in the time evolution period of spin systems and a qubit interaction between nuclear spins is simulated by substitution into interactions between electron and nuclear spins to conquer sequences with fast computational ability. As a result, I elucidate the difference between NMR-QCs and ESR-QCs and the most significant properties are found in evolution time due to the difference of spin interaction strengths between NMR and ESR.[4] In order to optimize pulse sequences for MSQC experimental conditions, numerical simulations were invoked to investigate a proper adiabatic path for MSQCs and Trotter formulas. Although modification of AQC conditions makes computational time larger, it is proven that MSQCs have ability to perform AQCs with analytical pulse sequences.

Following the convention in magnetic resonance spectroscopy appeared in standard theoretical textbooks and papers, I use unit of $\hbar = 1$ in both chapters 3 and 4. Since units giving important features in magnetic resonance systems are only frequency, angular frequency, energy and time, the coefficients by fixing $\hbar = 1$ can put into the weight dimension. As a result, energy is the same unit as angular

frequency (ω /rad $\cdot$ s^{-1}) and others do not change unit in frequency (v /Hz), the magnetic field ($\boldsymbol{B}$ /T) and time (t /s). In chapters 3 and 4, Hamiltonian is written in angular frequency and the difference between angular frequency and frequency is the coefficient of 2π.

3-2. Adiabatic Quantum Algorithms

The purpose of this section is to introduce an adiabatic model of quantum computing and its algorithms. In subsection 3-2-1, I introduce the quantum computation model and the example algorithm shown in subsection 3-2-2 and 3-2-3, respectively. Application procedure for magnetic resonance experiments is shown in the subsection 3-2-4, in which an AQC form is changed into the time evolution picture from the time dependent Hamiltonian manipulation picture. Strictly speaking, Hamiltonian and time have arbitrary unit as long as the product has unit of action in this section.

3-2-1. Adiabatic Quantum Computers (AQCs)[10]

Algorithms of AQCs are named adiabatic quantum algorithm (AQUA) and based on time evolution of the ground states (Figure 3-2.1). Adiabatic theorem is briefly explained that if Hamiltonian is varied slowly and then the quantum system remains its ground state. Describing the details of theorem, let us assume following dynamics of a quantum system: 1) An initial quantum state is a ground state of System Hamiltonian, 2) System Hamiltonian is varied slowly from the initial one to the final one and 3) There is no intersection between the ground state and transitable exited states while the evolution period. With three conditions, adiabatic theorem indicate that the quantum systems remain in the ground states of the time dependent Hamiltonian.

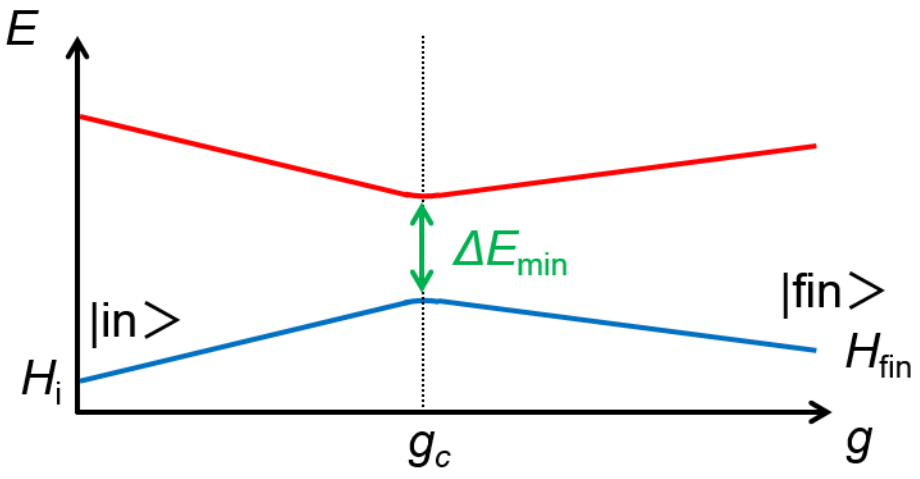

Figure 3-2.1. Schematic view of AQC. The blue and red lines indicate the ground and first excited states of a quantum system, respectively. The system Hamiltonian moves from the initial Hamiltonian (H_i) to the final one (H_f). g denotes a variable changing from 0 to 1 and corresponding to the initial state ($g = 0$) and final one ($g = 1$). The minimum energy gap is ΔE_{min} at $g = g_c$.

From a point of view of the quantum computing, adiabatic theorem proposes a way to find a ground state of the Hamiltonian. Note that developing slowly to the arbitrary Hamiltonian, but the ground state is unknown, allows us to prepare its ground state. This is the computational process of AQC. Since the inverse of energy gap (ΔE) between the ground state and transitable exited states is proportional to the evolution speed of time dependent Hamiltonian, the computational time of AQC becomes longer when the energy gap is small. In most AQUA, the computational time of AQC is unknown because the problem to estimate energy gap is harder than solving the ground state of Hamiltonian. Although there are algorithms with known computational time, the path is extremely simple to discuss AQC in a general manner. For instance, the adiabatic searching algorithm can be performed with $\sqrt{N}$ against the problem size N[13] as same order of Grover's algorithm in standard QCs. Excepting a problem of computational complexity, AQC has same properties as QCs: 1) AQC is equivalent to standard QCs,[14] 2) AQC has error correcting codes.[15]

3-2-2. Three-qubit Hamiltonian for Adiabatic Factorization Algorithm of 21[4, 6]

Here, I introduce adiabatic factorization algorithms of 21 with 3-qubit. The 2-qubit algorithm is simplified from the 3-qubit one, thus the 3-qubit algorithm is discussed in first. In the following section, the derivations of equations are written mostly for the 3-qubit algorithm, because it is easy to apply the same approach for the 2-qubit algorithm. The 3-qubit version of this algorithm is proposed by X. Peng et al. and the ideal final/problem Hamiltonian is Eq. (3-2.1),

$$\hat{H}_{\mathrm{f}} = \left(\hat{N} - \hat{x}\hat{y}\right)^2 \tag{3-2.1}$$

where $\hat{N} = 21\hat{I}$ and ($\hat{x}$, $\hat{y}$) is the binary representation of natural numbers by qubits as described later in Eqs. (3-2.3) and (3-2.4). Clearly, Eq. (3-2.2) is derived from 21 = *xy* giving a minimum value of Hamiltonian.

$$\left\langle \hat{H}_{\mathrm{f}} \right\rangle = 0 \Leftrightarrow \left(\langle \hat{x} \rangle, \langle \hat{y} \rangle\right) = (7, 3) \text{ or } (3, 7) \tag{3-2.2}$$

Without loss of generality, $\hat{x}$ and $\hat{y}$ can assume as $\langle \hat{x} \rangle \le \langle \hat{y} \rangle$ and both are odd. Then Eqs. (3-2.3) and (3-2.4) are derived, since $\langle \hat{x} \rangle^2 \le \hat{N}$ and $\langle \hat{y} \rangle^2 \ge \hat{N}$ are derived from the relation of $\langle \hat{x} \rangle \times \langle \hat{y} \rangle \approx \hat{N}$,

$$3 \le \langle \hat{x} \rangle \le \sqrt{21} \quad \Rightarrow \quad \hat{x} = \left(\hat{I} - \hat{\sigma}_z^1\right) + \hat{I} \tag{3-2.3}$$

$$\sqrt{21} \le \langle \hat{y} \rangle \le 21/3 \quad \Rightarrow \quad \hat{y} = 2\left(\hat{I} - \hat{\sigma}_z^2\right) + \left(\hat{I} - \hat{\sigma}_z^3\right) + \hat{I} \tag{3-2.4}$$

where $\hat{\sigma}_z^i$ is the $\hat{\sigma}_z$ value of the *i*th spin. A number 3 in Eqs. (3-2.3) and (3-2.4) indicates the minimum prim number. Note that since the adiabatic path of algorithm is an imaginary pathway, each

unit of time and Hamiltonian is arbitrary within the product of them consisting correct units. Thus, I do not discuss about the unit in adiabatic paths.

The ground state of $\hat{H}_{\mathrm{f}}$ in Eq. (3-2.1) is |↓↓↓>, in which the expectation values of $\hat{x}$ and $\hat{y}$ give $\left(\langle\hat{x}\rangle,\langle\hat{y}\rangle\right)=(3,7)$. Remembering whole scheme of AQC, a development of unknown ground state Hamiltonian $\hat{H}_{\mathrm{f}}$ supplies the ground state of |↓↓↓>. Then one can calculate $\left(\langle\hat{x}\rangle,\langle\hat{y}\rangle\right)$ with classical computers or by hand, and obtains the answer (3, 7) as a factorization result of 21.

Note that the computational speed of this algorithm is still unknown with large qubits although there are an estimation until 16 qubits. And this adiabatic algorithm is not always efficient when the solutions of $\hat{x}$ and $\hat{y}$ need the same bit length leading two solutions of $\left(\langle\hat{x}\rangle,\langle\hat{y}\rangle\right)$ and $\left(\langle\hat{y}\rangle,\langle\hat{x}\rangle\right)$ with $\Delta E_{\min}$ = 0. However, these problems should be investigated with quantum experiments. Developing $\hat{H}_{\mathrm{f}}$, Eq. (3-2.5) is obtained,

$$\hat{H}_{\mathrm{f}} \sim 84\hat{\sigma}_z^1+88\hat{\sigma}_z^2+44\hat{\sigma}_z^3-20\hat{\sigma}_z^1\hat{\sigma}_z^2-10\hat{\sigma}_z^1\hat{\sigma}_z^3-20\hat{\sigma}_z^2\hat{\sigma}_z^3-16\hat{\sigma}_z^1\hat{\sigma}_z^2\hat{\sigma}_z^3 \tag{3-2.5}$$

and is utilized for implementing pulse sequences. In this transformation, an identity operator $\hat{I}$ is neglected. The initial Hamiltonian which is arbitrary operator is selected as follows,

$$\hat{H}_{\mathrm{i}} = 30\sum_{i=1}^{3}\sigma_x^i \tag{3-2.6}$$

where the ground state is |*x*-, *x*-, *x*->. Adopting the adiabatic path, described in subsection 3.2.4, fidelity i.e. the success probability of the algorithm is known as 0.91.

3-2-3. Two-qubit Hamiltonian for Adiabatic Factorization Algorithm of 21

The adiabatic factorization described in subsection 3-2-2 is possible to perform by 2-qubit systems with one assumption. Although this approach solves one part of the factorization problem, it is possible to reduce several qubits. In this subsection, I utilize multiplication figure to reduce about 0 to 2 qubits.

Multiple of (*x*, *y*) sometimes has a simple structure. Fig. 3-2.2 shows multiplication figure of 21, where q_i is a binary representation of a bit and z_{ij} is career to the j^{th} order from i^{th} order. As shown in figure, the relation of $q_2 + q_3 = 0$ suggests obviously $q_2 = q_3$ in mod. 2. Therefore, one can reduce one qubit by replacing Eqs. (3-2.3) and (3-2.4) into Eqs. (3-2.7) and (3-2.8), and then the final Hamiltonian changes into Eq. (3-2.9).

$$3 \le \langle\hat{x}\rangle \le \sqrt{21} \quad \Rightarrow \quad \hat{x} = \left(\hat{I}-\hat{\sigma}_z^1\right)+\hat{I} \tag{3-2.7}$$

$$\sqrt{21} \le \langle\hat{y}\rangle \le 21/3 \quad \Rightarrow \quad \hat{y} = 2\left(\hat{I}-\hat{\sigma}_z^2\right)+\left(\hat{I}-\hat{\sigma}_z^1\right)+\hat{I} \tag{3-2.8}$$

$$\hat{H}_{\mathrm{f}} \sim 68\hat{\sigma}_z^1+132\hat{\sigma}_z^2-30\hat{\sigma}_z^1\hat{\sigma}_z^2 \tag{3-2.9}$$

Since the initial Hamiltonian is arbitrary, I set the initial Hamiltonian as Eq. (3-2.10).

$$\hat{H}_{\mathrm{i}} = 100\sum_{i=1}^{2}\sigma_x^i \tag{3-2.10}$$

where the ground state is |*x*-, *x*-> and the fidelity with the adiabatic path of subsection 3.2.4 is 0.97. At the following section, although I discuss mostly the 3-qubit algorithms only, clearly same approach can apply for the 2-qubit algorithm.

	16	8	4	2	1
			q_2	q_3	1
				q_1	1
			q_2	q_3	1
		q_1q_2	q_1q_3	q_1	
carriers →		$z_{2,3}$	$z_{1,2}$		
21 ≡	1	0	1	0	1

Figure 3-2.2. Multiplication figure of 21 in binary representation. The 1st, 2nd and 3rd qubits corresponds to Eqs. (3-2.3) and (3-2.4). z_{ij} is the career from i^{th} to j^{th}.

3-2-4. Adiabatic Path for Numerical Pulse Sequences

In subsections 3-2-2 and 3-2-3, the initial and final Hamiltonians are defined. Performing AQC, the adiabatic path connecting both Hamiltonians is required in order to define the time dependent Hamiltonian. In this subsection, I describe the conditions of slowly varying Hamiltonian. Dynamics of quantum system can be written by time evolution operator given in Eq. (3-2.11).

$$\hat{U} = \hat{\mathrm{T}}\exp\left(-i\int_{t_{\mathrm{i}}}^{t_{\mathrm{f}}}\hat{H}(t)dt\right) \tag{3-2.11}$$

Where $\hat{\mathrm{T}}$ is time ordered product, $\hat{H}(t_{\mathrm{f}}) = \hat{H}_{\mathrm{f}}$, $\hat{H}(t_{\mathrm{i}}) = \hat{H}_{\mathrm{i}}$ and t_{i} is the initial time, and t_{f} is the final time of evolution. Approximating the finite time step for pulse calculations,

$$\hat{U} = \prod_{m=1}^{5}\exp\left(-\Delta t \times i\hat{H}_m\right) \tag{3-2.12}$$

$$\hat{H}_m = (m/5)^2\hat{H}_{\mathrm{f}} + \{1-(m/5)^2\}\hat{H}_{\mathrm{i}} \tag{3-2.13}$$

where Δt is 0.028 for 3-qubit algorithm and 0.014 for 2-qubit algorithm, and the time evolution in both cases is divided into discrete 5 steps. Note that $\hat{H}_{\mathrm{i}}$ should be non-commutative operator with $\hat{H}_{\mathrm{f}}$

(Eq. (3-2.13)) to avoid the crossing of energy levels between the ground state and transitable exited states. If $\hat{H}_m$ was composed of only $\hat{\sigma}_z^i$ operators, the operator $\hat{U}$ never flip the spins. Therefore, Trotter expansion into the commutative operator sets is always required, because ESR/NMR systems cannot vary Hamiltonian of molecules directly. The details are discussed in section 3-3.

Here, I limit the quantum algorithm only for the 3-qubit one. Each exponent product composed of only the commutative operator set is written in Eqs. (3-2.14) utilized by Trotter expansion.

$$\hat{U} = \prod_{m=1}^{5} \hat{U}_{mi} \times \hat{U}_{mf} \times \hat{U}_{mi} \tag{3-2.14a}$$

$$\hat{U}_{mi} = \exp(-i0.028\{1-(m/5)^2\}\hat{H}_i/2) \tag{3-2.14b}$$

$$\hat{U}_{mf} = \exp(-i0.028(m/5)^2 \hat{H}_f) \tag{3-2.14c}$$

The concrete Eqs. (3-2.14b) and (3-2.14c) are as follows:

$$\hat{U}_{mi} = \prod_{i=1}^{3} \exp\left(-i0.42\{1-s_m\}\hat{\sigma}_x^i\right) \tag{3-2.15a}$$

$$\begin{aligned}\hat{U}_{mf} = {} & \exp\left(-i2.352 s_m \hat{\sigma}_x^1\right) \times \exp\left(-i2.464 s_m \hat{\sigma}_x^2\right) \times \exp\left(-i1.232 s_m \hat{\sigma}_x^3\right) \\ & \times \exp\left(-i0.56 s_m \hat{\sigma}_x^1 \hat{\sigma}_x^2\right) \times \exp\left(-i0.56 s_m \hat{\sigma}_x^2 \hat{\sigma}_x^3\right) \times \exp\left(-i0.28 s_m \hat{\sigma}_x^3 \hat{\sigma}_x^1\right) \\ & \times \exp\left(-i0.448 s_m \hat{\sigma}_x^1 \hat{\sigma}_x^2 \hat{\sigma}_x^3\right)\end{aligned} \tag{3-2.15b}$$

$$s_m = (m/5)^2 \tag{3-2.15c}$$

Eqs. (3-2.14) and (3-2.15) suggest different methods to perform from varying the system Hamiltonian. The suggestion is that AQC can also be performed by simulating adiabatic path with the time dependent Hamiltonian. In ESR/NMR system, former one is almost impossible to perform since the system Hamiltonian including interaction terms between electron/nuclear spins cannot change the strengths. Thus, the application problem is changed for the pulse sequences how to simulate the time evolution of time dependent Hamiltonian.

3-3. Mathematical Techniques for Pulsed ESR Sequence Calculations

Secular approximation for 3-electron systems and 1-electron and 2-nuclear systems is introduced in this section toward the 3-qubit algorithm of adiabatic quantum computing. The approximation is significant in the next section 3-4 since the analytical calculations require the approximated Hamiltonian for the time evolution period. These approaches are well introduced in Mehring book.[16]

3-3-1. Theoretical Approaches in Pulsed ESR

For an analytical pulse sequence study, the several approaches are proposed as theoretical techniques due to the difficulties of calculations of time evolution. A common part of all approaches, e.g. Floquet Approach (FA),[17] variations of perturbation theory[9, 16, 18] and Secular Averaging Approach (SAA) [16], is to find the approximated spin Hamiltonian in time evolution periods. I have adopted the simplest analytical technique, SAA, to perform AQCs. The simple form of the effective spin Hamiltonian is due to approximated interaction picture called rotational frame approaches. In the perturbation theory[9], the theory can calculate time evolution part with more accurate manner, and requires larger number of pulses than that applied in the pulse sequence of SAA. In principle, a lot of pulses can develop systems more accurately but the accuracy is limited by analytical solvable equations.

3-3-2. Spin Hamiltonian in Pulsed ESR

Spin Hamiltonian of open-shell molecules is written by Eq. (3-3.1) in Schrödinger picture.

$$\hat{H}_{\mathrm{MSQC}} = \sum_{i=1}^{N} \mathbf{S}^i g_{\mathrm{e}}^i \beta_{\mathrm{e}} \mathbf{B} - \sum_{i=1}^{M} \mathbf{I}^i g_{\mathrm{n}}^i \beta_{\mathrm{n}}^i \mathbf{B} + 2\pi \sum_{i<j}^{N,N} \mathbf{S}^i (j + D)_{\mathrm{e}}^{ij} \mathbf{S}^j + 2\pi \sum_{i=j=1}^{N,M} \mathbf{S}^i A^{ij} \mathbf{I}^j + 2\pi \sum_{i<j}^{M,M} \mathbf{I}^i (j + D)_{\mathrm{n}}^{ij} \mathbf{I}^j \qquad (3\text{-}3.1)$$

where, N and M are the spin number of electrons and nuclei, respectively. Hamiltonian terms with $\boldsymbol{B}$ include two parts, the static magnetic field and the pulse magnetic field by irradiation of micro/radio waves. In the first and second Zeeman terms, g^i is a 2nd rank tensor which is related to the Larmor frequency $\omega_0/2\pi$ of the ith spin, i.e. $\omega_{0,\mathrm{e}}^i = g_{zz}^i \beta_{\mathrm{e}} B_{\mathrm{z}}$ and $\omega_{0,\mathrm{n}}^i = -g_{zz}^i \beta_{\mathrm{n}}^i B_{\mathrm{z}}$. The other terms are interactions between spins which are also described by 2nd rank tensors of J, D and A, exchange, spin-dipolar and hyperfine interactions, respectively.

Although SAA contains the approximation picture, SAA is widely used for time evolution of spin systems by analytical calculations. Thus, I restrict the system satisfying conditions as follows: 1) small anisotropy of g-tensors for electrons and nuclei, 2) strong magnetic field limit for electrons, i.e. Zeeman term is much larger than others, but not for nuclei and 3) co-axis properties for hyperfine tensors. 1) and 3) are adopted in order to apply theory for solid state systems.

In the following section, I discuss the pulse generation methods for 3-spin systems in single crystals. Almost the same methods are applicable for the pulse sequences of solution ESR systems which will be also described. In solution ESR, the spin Hamiltonian can be simpler than that of single crystal systems.

3-3-3. Approximated Spin Hamiltonian in 3-electron Systems

Spin Hamiltonian in Schrödinger picture corresponding to Eq. (3-3.1) is written by Eq. (3-3.2) for the three electron system.

$$\hat{H}_{3e} = \sum_{i=1}^{3} \hat{\mathbf{S}}^i g^i \beta_e \mathbf{B} + 2\pi \sum_{i<j}^{3,3} \hat{\mathbf{S}}^i (J+D)^{ij} \hat{\mathbf{S}}^j \tag{3-3.2}$$

Assuming time evolution period, first term only contains static magnetic field along *z*-direction ($\boldsymbol{B} = (0,0,B_z)$). Then, the few of Zeeman terms are vanished as Eq. (3-3.3).

$$\hat{H}_{3e} = \sum_{i=1}^{3} \left(\sum_{k=x,y,z} \hat{S}_k^i g_{kz}^i \beta_e B_z \right) + 2\pi \sum_{i<j}^{3,3} \hat{\mathbf{S}}^i (J+D)^{ij} \hat{\mathbf{S}}^j \tag{3-3.3}$$

There are two methods to transform the rotational frame: 1) individual rotating frame and 2) common rotating frame. Although the latter one is often used in ESR, the former one can be used in future like the NMR. Here, I mention the individual rotating frame first. The non-perturbed Hamiltonian and the perturbed Hamiltonian in the rotating frame are given by Eqs. (3-3.4) and (3-3.5), respectively. And the time dependent spin operators are given by Eqs. (3-3.6).

$$\hat{H}_{3e}^0 = \sum_{i=1}^{3} \omega_{0,e}^i \hat{S}_z^i \tag{3-3.4}$$

$$\hat{H}_{3e}^{int} = \sum_{i=1}^{3} \left(\sum_{k=x,y} \hat{S}_k^i(t) g_{kz}^i \beta_e B_z \right) + 2\pi \sum_{i<j}^{3,3} \left(\sum_{k,l=x,y,z} \hat{S}_k^i(t) (J+D)_{kl}^{ij} \hat{S}_l^j(t) \right) \tag{3-3.5}$$

$$\hat{S}_x^i(t) = \cos(\omega_{0,e}^i t)\hat{S}_x^i - \sin(\omega_{0,e}^i t)\hat{S}_y^i \tag{3-3.6a}$$

$$\hat{S}_y^i(t) = \sin(\omega_{0,e}^i t)\hat{S}_x^i + \cos(\omega_{0,e}^i t)\hat{S}_y^i \tag{3-3.6b}$$

$$\hat{S}_z^i(t) = \hat{S}_z^i \tag{3-3.6c}$$

Equations above have no approximation, and zeroth order SAA of the individual rotating frame is as follows assuming time averaging by fast Larmor rotations of individual spins, and then neglects all anisotropic terms of the perturbed Hamiltonian. This is on the basis of smaller amplitude of the perturbed Hamiltonian against the non-perturbed one, i.e. small interaction terms between spins against the Zeeman terms[16]. Therefore Eq. (3-3.5) is transformed into Eq. (3-3.7) in individual rotating frame.

$$\hat{H}_{3e}^{int} = 2\pi \sum_{i<j}^{3,3} \hat{S}_z^i (J+D)_{zz}^{ij} \hat{S}_z^j \tag{3-3.7}$$

The perturbed Hamiltonian of Eq. (3-3.7) is adopted for the following pulse sequence study (section 3-4) as effective spin Hamiltonian of the qubit system.

The interaction forms in the common rotating frame are slightly different from equations above. The interaction picture focusing on the single Larmor frequency of the 1st electron is described by Eqs. (3-3.4'), (3-3.5') and (3-3.6').

$$\hat{H}_{3e}^{0} = \sum_{i=1}^{3} \omega_{0,e}^{1} \hat{S}_z^i \tag{3-3.4'}$$

$$\hat{H}_{3e}^{int} = \sum_{i=1}^{3}\left(\sum_{k=x,y} \hat{S}_k^i(t) g_{kz}^i \beta_e B_z \right) + 2\pi \sum_{i<j}^{3,3}\left(\sum_{k,l=x,y,z} \hat{S}_k^i(t)(J+D)_{kl}^{ij} \hat{S}_l^j(t) \right) + \sum_{i=2}^{3} \hat{S}_z^i \left(g_{zz}^i - g_{zz}^1 \right) \beta_e B_z \tag{3-3.5'}$$

$$\hat{S}_x^i(t) = \cos(\omega_{0,e}^1 t)\hat{S}_x^i - \sin(\omega_{0,e}^1 t)\hat{S}_y^i \tag{3-3.6a'}$$

$$\hat{S}_y^i(t) = \sin(\omega_{0,e}^1 t)\hat{S}_x^i + \cos(\omega_{0,e}^1 t)\hat{S}_y^i \tag{3-3.6b'}$$

$$\hat{S}_z^i(t) = \hat{S}_z^i \tag{3-3.6c'}$$

As mentioned all spins are rotating in a common Larmor frame of the 1st spin, the subtracted frequency for the 2nd and the 3rd spins based on the rotational speed appears in Eq. (3-3.5') as the result. By applying SAA, the following equation is obtained as the approximated perturbed Hamiltonian. The extra terms given in Eq. (3-3.7') can be also eliminated with the short pulse sequences (see subsection 3-4-2).

$$\hat{H}_{3e}^{int} = 2\pi \sum_{i<j}^{3,3} \hat{S}_z^i (J+D)_{zz}^{ij} \hat{S}_z^j + \sum_{i=2}^{3} \hat{S}_z^i \left(g_{zz}^i - g_{zz}^1 \right) \beta_e B_z \tag{3-3.7'}$$

3-3-4. Approximated Spin Hamiltonian in 1-electron and 2-nuclear Systems

Analytical approaches for the 1-elecctron and 2-nuclear systems are slightly different in 3-electron systems due to the hetero-spin properties. The spin Hamiltonian of this system can be written by Eq. (3-3.8) in Schrödinger picture.

$$\hat{H}_{1e+2n} = \hat{\mathbf{S}}^1 g^1 \beta_e \mathbf{B} - \sum_{i=2}^{3} \hat{\mathbf{I}}^i g^i \beta_n^i \mathbf{B} + 2\pi \sum_{j=2}^{3} \hat{\mathbf{S}}^1 A^{1j} \hat{\mathbf{I}}^j + 2\pi \hat{\mathbf{I}}^2 (J+D)^{23} \hat{\mathbf{I}}^3 \tag{3-3.8}$$

With the static magnetic field $\boldsymbol{B} = (0,0,B_z)$,

$$\hat{H}_{1e+2n} = \sum_{k=x,y,z} \hat{S}_k^1 g_{kz}^1 \beta_e B_z - \sum_{i=2}^{3}\left(\sum_{k=x,y,z} \hat{I}_k^i g_{kz}^i \beta_n B_z \right) + 2\pi \sum_{j=2}^{3} \hat{\mathbf{S}}^1 A^{1j} \hat{\mathbf{I}}^j + 2\pi \hat{\mathbf{I}}^2 (J+D)^{23} \hat{\mathbf{I}}^3 \tag{3-3.9}$$

is obtained. In the individual rotating frame case, the Larmor frequency is selected to be $\omega_{0,e}^1 = g_{zz}^1 \beta_e B_z$ and $\omega_{0,n}^i = -g_{zz}^i \beta_n^i B_z$, then the Hamiltonian in interaction picture is given by Eqs. (3-3.10) and (3-3.11),

$$\hat{H}^{0}_{1e+2n} = \omega^{1}_{0,e}\hat{S}^{1}_{z} + \sum_{i=2}^{3}\omega^{i}_{0,n}\hat{I}^{i}_{z} \tag{3-3.10}$$

$$\hat{H}^{int}_{1e+2n} = \sum_{k=x,y}\hat{S}^{1}_{k}(t)g^{1}_{kz}\beta_{e}B_{z} - \sum_{i=2}^{3}\left(\sum_{k=x,y}\hat{I}^{i}_{k}(t)g^{i}_{kz}\beta_{n}B_{z}\right) + 2\pi\sum_{j=2}^{3}\left(\sum_{k,l=x,y,z}\hat{S}^{1}_{k}(t)A^{1j}_{kl}\hat{I}^{j}_{l}(t)\right) + 2\pi\sum_{k,l=x,y,z}\hat{I}^{2}_{k}(t)(J+D)^{23}_{kl}\hat{I}^{3}_{l}(t) \tag{3-3.11}$$

where the time dependent spin operator for the electron is written by Eqs. (3-3.6) and for nuclear spins is given by Eqs. (3-3.12).

$$\hat{I}^{i}_{x}(t) = \cos(\omega^{i}_{0,n}t)\hat{I}^{i}_{x} - \sin(\omega^{i}_{0,n}t)\hat{I}^{i}_{y} \tag{3-3.12a}$$

$$\hat{I}^{i}_{y}(t) = \sin(\omega^{i}_{0,n}t)\hat{I}^{i}_{x} + \cos(\omega^{i}_{0,n}t)\hat{I}^{i}_{y} \tag{3-3.12b}$$

$$\hat{I}^{i}_{z}(t) = \hat{I}^{i}_{z} \tag{3-3.12c}$$

Discussing the rotating frame in the 1-electron and 2-nuclear system, the same approach is possible for the electron part. But for nuclei, their Larmor terms are not large enough against hyperfine couplings to reach the SAA limit, thus the rotating terms do not vanish in nuclear case. As a result,

$$\hat{H}^{int}_{1e+2n} = 2\pi\sum_{j=2}^{3}\left(\sum_{l=x,y,z}\hat{S}^{1}_{z}A^{1j}_{zl}\hat{I}^{j}_{l}(t)\right) + 2\pi\hat{I}^{2}_{z}(J+D)^{23}_{zz}\hat{I}^{3}_{z} \tag{3-3.13}$$

Eq. (3-3.13) is obtained as time dependent perturbed Hamiltonian. Since the time dependent parts of $\hat{I}^{i}_{x,y}(t)$ make hard to calculate a pulse sequence with analytical techniques, I selected the static magnetic field (B_0) parallel to the principal axis of both hyperfine tensors, i.e. coaxes. Note that the coaxes properties are significant only in single crystal systems not but for solution systems by virtue of the isotropic tensor character. In the conditions mentioned above, the perturbed Hamiltonian in time evolution operator is written by Eq. (3-3-4.7).

$$\hat{H}^{int}_{1e+2n} = 2\pi\sum_{j=2}^{3}\hat{S}^{1}_{z}A^{1j}_{zz}\hat{I}^{j}_{z} + 2\pi\hat{I}^{2}_{z}(J+D)^{23}_{zz}\hat{I}^{3}_{z} \tag{3-3-4.7}$$

And the Eq. (3-3-4.7) does not depend on time explicitly.

In the common rotating frame that two nuclei rotate in the same frame, Eqs. (3-3.10'), (3-3.11') and (3-3.12') are given.

$$\hat{H}^{0}_{1e+2n} = \omega^{1}_{0,e}\hat{S}^{i}_{z} + \sum_{i=2}^{3}\omega^{2}_{0,n}\hat{I}^{i}_{z} \tag{3-3.10'}$$

$$\hat{H}^{int}_{1e+2n} = \sum_{k=x,y}\hat{S}^{1}_{k}(t)g^{1}_{kz}\beta_{e}B_{z} - \sum_{i=2}^{3}\left(\sum_{k=x,y}\hat{I}^{i}_{k}(t)g^{i}_{kz}\beta_{n}B_{z}\right) + 2\pi\sum_{j=2}^{3}\left(\sum_{k,l=x,y,z}\hat{S}^{1}_{k}(t)A^{1j}_{kl}\hat{I}^{j}_{l}(t)\right) + 2\pi\sum_{k,l=x,y,z}\hat{I}^{2}_{k}(t)(J+D)^{23}_{kl}\hat{I}^{3}_{l}(t) + I^{3}_{z}\left(g^{3}_{zz} - g^{2}_{zz}\right)\beta^{3}_{n}B_{z} \tag{3-3.11'}$$

$$\hat{I}^{2}_{x}(t) = \cos(\omega^{2}_{0,n}t)\hat{I}^{i}_{x} - \sin(\omega^{2}_{0,n}t)\hat{I}^{i}_{y} \tag{3-3.12a'}$$

$$\hat{I}^{2}_{y}(t) = \sin(\omega^{2}_{0,n}t)\hat{I}^{i}_{x} + \cos(\omega^{2}_{0,n}t)\hat{I}^{i}_{y} \tag{3-3.12b'}$$

$$\hat{I}^{i}_{z}(t) = \hat{I}^{i}_{z} \tag{3-3.12c'}$$

The last offset (*g*-shift) is the only difference between Eqs. (3-3.11) and (3-3.11'). By taking the same procedure, Eq. (3-3.13') is obtained for single crystal systems. This extra term can be also eliminated with the short pulse sequences (see subsection 3-4-2).

$$\hat{H}^{\text{int}}_{1e+2n} = 2\pi\sum_{j=2}^{3}\hat{S}^{1}_{z}A^{1j}_{zz}\hat{I}^{j}_{z} + 2\pi\hat{I}^{2}_{z}(J+D)^{23}_{zz}\hat{I}^{3}_{z} + I^{3}_{z}\left(g^{3}_{zz} - g^{2}_{zz}\right)\beta^{3}_{n}B_{z} \qquad \text{(3-3.13')}$$

3-4. Analytical Calculations of Pulse Sequences for AQCs

Here, I describe the analytical calculations of 3-qubit AQC pulse sequences. All the components in adiabatic time evolution operator are decomposed into the following a set of ESR spin operations. The set of operations with ESR-QC is assumed 1) arbitrary spin rotations in *x*- and *y*-axis directions for individual spins and 2) time evolution with the SAA spin Hamiltonian for molecules ($\hat{H}_{3e}^{int}$ and $\hat{H}_{1e+2n}^{int}$) discussed in subsections 3-3-3 and 3-3-4. Since both spin Hamiltonians have Ising type 3-qubits with individual manipulations, the systems can perform universal quantum gate (UQG) which can perform all unitary operations.[1, 16] Thus, the remained problem is how to simulate time evolution of AQUA written in subsection 3-2-4.

The operation set is gevin by S. (3-4.1) and (3-4.2),

$\{\sigma_x^i, \sigma_y^i, \hat{H}_{3e}^{int}\}$ for the three electron system S. (3-4.1)

$\{\sigma_x^i, \sigma_y^i, \hat{H}_{1e+2n}^{int}\}$ for the one electron and two nuclear system S. (3-4.2)

and the required 3-qubit AQC operations are as follows:

$$\hat{U}_{mi} = \prod_{i=1}^{3} \exp\left(-i0.42\{1-s_m\}\hat{\sigma}_x^i\right) \tag{3-4.3a}$$

$$s_m = (m/5)^2 \tag{3-4.3b}$$

$$\hat{U}_z = \exp\left(-i2.352 s_m \hat{\sigma}_z^1\right) \times \exp\left(-i2.464 s_m \hat{\sigma}_z^2\right) \times \exp\left(-i1.232 s_m \hat{\sigma}_z^3\right) \tag{3-4.4a}$$

$$\hat{U}_{zz} = \exp\left(-i0.56 s_m \hat{\sigma}_z^1 \hat{\sigma}_z^2\right) \times \exp\left(-i0.56 s_m \hat{\sigma}_z^2 \hat{\sigma}_z^3\right) \times \exp\left(-i0.28 s_m \hat{\sigma}_z^3 \hat{\sigma}_z^1\right) \tag{3-4.4b}$$

$$\hat{U}_{zzz} = \exp\left(-i0.448 s_m \hat{\sigma}_z^1 \hat{\sigma}_z^2 \hat{\sigma}_z^3\right) \tag{3-4.4c}$$

$$\hat{U}_{zz2} = \exp\left(-i0.56 s_m \hat{\sigma}_z^2 \hat{\sigma}_z^3\right) \tag{3-4.4d}$$

All the equations are discussed in subsection 3-2-2 and 3-2-4.

The contents of section 3-4 are,

1) Simulations of single qubit rotations with arbitrary angles. (subsection 3-4-1)
    1. Simulations of single qubit rotations around x-/y-axis : Eq. (3-4.4a)
    2. Simulations of single qubit rotations around z-axis: Eq. (3-4.4b)
2) Simulations of two qubit interactions depending on interaction picture. (subsection 3-4-2)
    1. Two qubit interactions in individual rotating frame: Eq. (3-4.4b)
    2. Two qubit interactions in common rotating frame.
3) Simulations of three qubit interactions and higher order qubit interactions. (subsection 3-4-3)
    1. Three qubit interactions: Eq. (3-4.4c).
    2. Higher order (>3) qubit interactions.
4) Simulation techniques for fast two qubit interactions between the nuclei. (subsection 3-4-4)
    1. Fast Simulation for two qubit interactions between the nuclei: Eq. (3-4.4d).
5) Constructions of Pulse sequences for AQC. (subsection 3-4-5)
    1. AQC pulse sequence in a 3-electron system.

2. AQC pulse sequence in a 1-electron and 2-nuclear system.

6) Discussions. (subsection 3-4-6)

Subsection 3-4-1 to 3-4-4 describes whole sequence decomposition methods for AQC. In subsection 3-4-5, pulse sequences of AQC are described. Most parts of ESR-AQC studies are supported by this section. Although the theoretical procedure is slightly complicated, almost all parts are utilized for pulse sequence calculations.

Figures 3-4.1 depicts notations of pulses in the sequences study. Black/red blocks indicates x-/y-direcction, filled/empty blocks indicate minus/pulse angle and oblong/square blocks are (π/2)-/π-pulses, respectively. Although there are two types of pulses, i.e. selective and non-selective pulses, I discussed the pulse sequences of AQCs only with selective pulses.

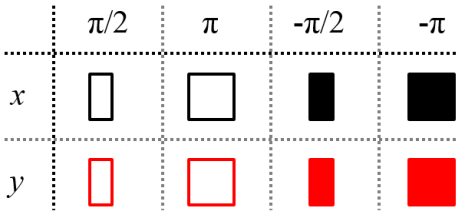

Figure 3-4.1 Notation of pulse operations. Black/red blocks are the rotation around the *x*-/*y*-axis. Oblong/square blocks indicate the rotational angles of (π/2)/π. The filled block means a minus angle operation. The other pulse operations around the *x*- and *y*- axes are written by blue blocks with a number or word.

3-4-1. Simulations of Single Qubit Rotations

Simulations of Single Qubit Rotations Around *x*-/*y*-axis

The most basal qubit operation is a single spin rotation performed by irradiation of a microwave pulse in ESR-QC experiments. Strictly discussing the pulse effects into spin systems are difficult to estimate and enough worth to investigate in another spin science aspect. Thus in section 3-4, I simply assumed an operation set of S. (3-4.1) and (3-4.2) due to the essence of AQC. By definition, $\theta = 2\alpha$ /rad rotation to the k^{th} spin with selective pulses around *x*-/*y*-axes is written as follows:

$$\exp\left(-i\alpha\sigma_x^k\right), \exp\left(-i\alpha\sigma_y^k\right) \qquad \text{S. (3-4.5)}$$

Thus, Eq. (3-4.3a) can obviously be performed and the parameter angle θ is given by Eq. (3-4.6).

$$\theta = 2\alpha = 0.84\{1 - s_m\} \qquad (3\text{-}4.6)$$

Simulations of Single Qubit Rotations Around *z*-axis

Simulations of single qubit rotations around *z*-axis are performed by combinations of single spin rotations around *x*- and *y*- axes. The spin rotations ($\theta = 2\alpha$ radians) around the *z*-axis are written by Eqs. (3-4.7) and (3-4.8). The corresponding pulses are shown in Fig. 3-4.2.

$$\exp\left(-i\alpha\sigma_z^k\right)=\exp\left(i\frac{\pi}{4}\sigma_y^k\right)\cdot\exp\left(-i\alpha\sigma_x^k\right)\cdot\exp\left(-i\frac{\pi}{4}\sigma_y^k\right) \tag{3-4.7}$$

$$\exp\left(-i\alpha\sigma_z^k\right)=\exp\left(-i\frac{\pi}{4}\sigma_x^k\right)\cdot\exp\left(-i\alpha\sigma_y^k\right)\cdot\exp\left(i\frac{\pi}{4}\sigma_x^k\right) \tag{3-4.8}$$

Adopting those equations, spin rotation angle θ_i /rad for the i^{th} spins in Eq. (3-4.4a) are described in Eq. (3-4.9).

$$\theta_1 = 4.704s_m, \theta_2 = 4.928s_m \text{ and } \theta_3 = 2.464s_m \tag{3-4.9}$$

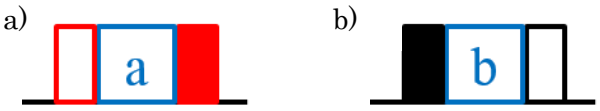

Figure 3-4.2. Pulse sequences for single qubit operations, a) Corresponding to Eq. (3-4.7) and b) Corresponding to Eq. (3-4.8). Blue blocks of a and b are $\theta = 2\alpha$ /rad rotation around the *x*- and *y*- axes, respectively.

3-4-2. Simulations of two qubit interactions

Simulations of Two Qubit Interactions in Individual Rotating Frame

In general, the simulations of two qubit interactions require the time evolution period with effective spin Hamiltonian. This part speeds up quantum algorithms by generation of entanglement. In this subsection, I describe the method to perform the arbitrary two-spin interactions between σ_z^i and σ_z^j ($i \neq j$) in 3 spins with individual rotating frame. There are a couple of target effective Hamiltonians written by Eqs. (3-4.10) and (3-4.11). The derivation is shown in subsection 3-3-3 and 3-3-4.

$$\hat{H}_{3e}^{\text{int}} = 2\pi\sum_{i<j}^{3,3}\hat{S}_z^i(J+D)_{zz}^{ij}\hat{S}_z^j \tag{3-4.10}$$

$$\hat{H}_{1e+2n}^{\text{int}} = 2\pi\sum_{j=2}^{3}\hat{S}_z^1 A_{zz}^{1j}\hat{I}_z^j + 2\pi\hat{I}_z^2(J+D)_{zz}^{23}\hat{I}_z^3 \tag{3-4.11}$$

In both systems, the simulating operator $\exp(-i\alpha^{ij}\sigma_z^i\sigma_z^j t)$ is derived by Eqs. (3-4.12),

$$\exp(-i\alpha^{ij}\sigma_z^i\sigma_z^j t)|_{i\neq k\neq l} = \exp(-iHt/2)\cdot\exp(-iH^{-k}t/2) \tag{3-4.12a}$$

$$= \exp(-iH^{-k}t/2)\cdot\exp(-iHt/2) \tag{3-4.12b}$$

where, $H = \sum_{i<j}^{3} \alpha^{ij} \sigma_z^i \sigma_z^j$ and $H^{-k} = \sum_{i<j}^{3} \alpha^{ij} \sigma_z^i \sigma_z^j |_{i \neq k \neq j} - \sum_{i \neq k}^{3} \alpha^{ik} \sigma_z^i \sigma_z^k$ in which α^{ij} corresponds to the coefficients of spin Hamiltonian. The operator $\exp(-i2\pi H^{-k} t)$ is possible to be simulated with Eqs. (3-4.13).

$$\exp(-iH^{-k}t/2) = \exp\left(-i\frac{\pi}{2}\sigma_x^k\right)\cdot\exp(-iHt)\cdot\exp\left(i\frac{\pi}{2}\sigma_x^k\right) \quad \text{(3-4.13a)}$$

$$= \exp\left(i\frac{\pi}{2}\sigma_x^k\right)\cdot\exp(-iHt)\cdot\exp\left(-i\frac{\pi}{2}\sigma_x^k\right) \quad \text{(3-4.13b)}$$

$$= \exp\left(-i\frac{\pi}{2}\sigma_y^k\right)\cdot\exp(-iHt)\cdot\exp\left(i\frac{\pi}{2}\sigma_y^k\right) \quad \text{(3-4.13c)}$$

$$= \exp\left(i\frac{\pi}{2}\sigma_y^k\right)\cdot\exp(-iHt)\cdot\exp\left(-i\frac{\pi}{2}\sigma_y^k\right) \quad \text{(3-4.13d)}$$

As described in the equations, all decomposed forms give the same operators. The calculated pulse sequence corresponding to Eqs. (3-4.12a) with (3-4.13a) is shown in Fig. 3-4.3.

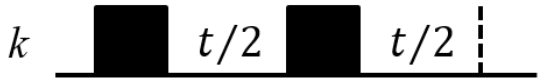

Figure 3-4.3. An example sequence for a two qubit interaction. The operation $\exp(-i\alpha^{ij}\sigma_z^i\sigma_z^j t)$ ($i \neq k$, $k \neq j$, $j \neq i$) is decomposed by Eqs. (3-4.12a) and (3-4.13a). The right vertical line is the end of the sequence.

If one does not consider global phase, the following any pattern of π pulses with the same direction are permitted (Eqs. (3-4.14)). Although I have not used the following equations in the sequence study, it is also recommended for usage. Because global phase is not significant on quantum computing.

$$-\exp(-iH^{-k}t/2) = \exp\left(-i\frac{\pi}{2}\sigma_x^k\right)\cdot\exp(-iHt)\cdot\exp\left(-i\frac{\pi}{2}\sigma_x^k\right) \quad \text{(3-4.14a)}$$

$$= \exp\left(i\frac{\pi}{2}\sigma_x^k\right)\cdot\exp(-iHt)\cdot\exp\left(i\frac{\pi}{2}\sigma_x^k\right) \quad \text{(3-4.14b)}$$

$$= \exp\left(-i\frac{\pi}{2}\sigma_y^k\right)\cdot\exp(-iHt)\cdot\exp\left(-i\frac{\pi}{2}\sigma_y^k\right) \quad \text{(3-4.14c)}$$

$$= \exp\left(i\frac{\pi}{2}\sigma_y^k\right)\cdot\exp(-iHt)\cdot\exp\left(i\frac{\pi}{2}\sigma_y^k\right) \quad \text{(3-4.14d)}$$

It is significant to simulate interactions with opposite coefficients, i.e. simulating the interaction of $-\alpha^{ij}$. In the case of the operator, $\exp(i\alpha^{ij}\sigma_z^i\sigma_z^j t)$, they can be written by Eqs. (3-4.15), utilizing an $\exp(-i\alpha^{ij}\sigma_z^i\sigma_z^j t)$ operation.

$$\exp(i\alpha^{ij}\sigma_z^i\sigma_z^j t) = \exp\left(-i\frac{\pi}{2}\sigma_x^i\right)\cdot\exp(-i\alpha^{ij}\sigma_z^i\sigma_z^j t)\cdot\exp\left(i\frac{\pi}{2}\sigma_x^i\right) \tag{3-4.15a}$$

$$= \exp\left(i\frac{\pi}{2}\sigma_x^i\right)\cdot\exp(-i\alpha^{ij}\sigma_z^i\sigma_z^j t)\cdot\exp\left(-i\frac{\pi}{2}\sigma_x^i\right) \tag{3-4.15b}$$

$$= \exp\left(-i\frac{\pi}{2}\sigma_y^i\right)\cdot\exp(-i\alpha^{ij}\sigma_z^i\sigma_z^j t)\cdot\exp\left(i\frac{\pi}{2}\sigma_y^i\right) \tag{3-4.15c}$$

$$= \exp\left(i\frac{\pi}{2}\sigma_y^i\right)\cdot\exp(-i\alpha^{ij}\sigma_z^i\sigma_z^j t)\cdot\exp\left(-i\frac{\pi}{2}\sigma_y^i\right) \tag{3-4.15d}$$

These equations also have the corresponding forms with some change in global phase.

Simulations of Two Qubit Interactions in Common Rotating Frame

From the experimental point of view, common rotating frame should be investigated as described in subsection 3-3-3 and 3-3-4. The Hamiltonian difference between individual and common rotating frame is the single spin rotating terms around *z*-axis, see Eqs. (3-4.16) and (3-4.17). Here, I show two methods in order to vanish the difference by annihilating extra terms. This problem does not related to the essence of AQC, thus those two techniques are just introduced here and not adopted in pulse sequence study. Conditions of example pulse sequences are selected as written in subsection 3-3-3 and 3-3-4.

$$\hat{H}_{3e}^{int} = 2\pi\sum_{i<j}^{3,3}\hat{S}_z^i(J+D)_{zz}^{ij}\hat{S}_z^j + \sum_{i=2}^{3}\hat{S}_z^i\left(g_{zz}^i - g_{zz}^1\right)\beta_e B_z \tag{3-4.16}$$

$$\hat{H}_{1e+2n}^{int} = 2\pi\sum_{j=2}^{3}\hat{S}_z^1 A_{zz}^{1j}\hat{I}_z^j + 2\pi\hat{I}_z^2(J+D)_{zz}^{23}\hat{I}_z^3 + I_z^3\left(g_{zz}^3 - g_{zz}^2\right)\beta_n^3 B_z \tag{3-4.17}$$

The first method is affecting minus rotations of the difference. This method requires selective pulses. Let me assume the time evolution $\exp(-i\hat{H}^{zz}\Delta t)$ for individual rotating frame and $\exp(-i\hat{H}^{int}\Delta t)$ for common rotating frame. In order to simulate $\exp(-i\hat{H}^{zz}\Delta t)$ by $\exp(-i\hat{H}^{int}\Delta t)$, subtracting the last terms are enough from Eqs. (3-4.16) and (3-4.17). The resulting time evolution is given in Eqs. (3-4.18) where the rotation angle ($2\alpha^k$ pulses) for the k^{th} spin is given in Table 3-4.1. For instance, A pulse sequence given in Fig. 3-4.4 is calculated from the conditions of Eqs. (3-4.7) and (3-4.18b).

$$\exp(-i\hat{H}^{zz}\Delta t) = \exp(-i\hat{H}^{int}\Delta t)\cdot\exp(-i\sum_{k=2}^{3}\alpha^k\sigma_z^k) \tag{3-4.18a}$$

$$= \exp(-i\sum_{k=2}^{3}\alpha^k\sigma_z^k)\cdot\exp(-i\hat{H}^{\mathrm{int}}\Delta t) \tag{3-4.18b}$$

Table 3-4.1. Rotation angles of the spins while time evolution of $\exp(-i\hat{H}^{\mathrm{int}}\Delta t)$ in the condition of subsection 3-3-3 and 3-3-4.

	Rotation angles ($\theta^2 = 2\alpha^2$) /rad	Rotation angles ($\theta^3 = 2\alpha^3$) /rad
3-electron system	$\left(g_{zz}^2 - g_{zz}^1\right)\beta_e B_z \Delta t$	$\left(g_{zz}^3 - g_{zz}^1\right)\beta_e B_z \Delta t$
1-electron and 2-nuclear system	0	$-\left(g_{zz}^3 - g_{zz}^1\right)\beta_n^3 B_z \Delta t$

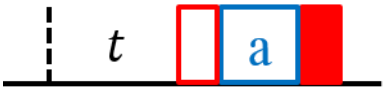

Figure 3-4.4. A simulation method of $\exp(-i\hat{H}^{zz}\Delta t)$ by the spin rotation around *z*-axis with Eq. (3-4.7) and (3-4.18b). The blue block a is the spin rotation around *x*-axis which spin number and angles (θ^k) are shown in Table 3-4.1.

The second method is based on annihilating odd order interactions of spins. This simulations are possible to be performed with two non-selective pulses and does not depend on the evolution time $\exp(-i\hat{H}^{\mathrm{int}}\Delta t)$. At first, we define $\hat{H}^{\mathrm{int},-s}$ as spin flipped Hamiltonian of all spins written in Eq. (3-4.19). The Hamiltonian is easily achieved with Eqs. (3-4.20).

$$\hat{H}^{\mathrm{int},-s}(\sigma_z^i) = \hat{H}^{\mathrm{int}}(-\sigma_z^i) \tag{3-4.19}$$

$$\exp(-i\hat{H}^{\mathrm{int},-s}\Delta t) = \exp\left(-i\frac{\pi}{2}\sum_{k=1}^{3}\sigma_x^k\right)\cdot\exp(-i\hat{H}^{\mathrm{int}}\Delta t)\cdot\exp\left(i\frac{\pi}{2}\sum_{k=1}^{3}\sigma_x^k\right) \tag{3-4.20a}$$

$$= \exp\left(i\frac{\pi}{2}\sum_{k=1}^{3}\sigma_x^k\right)\cdot\exp(-i\hat{H}^{\mathrm{int}}\Delta t)\cdot\exp\left(-i\frac{\pi}{2}\sum_{k=1}^{3}\sigma_x^k\right) \tag{3-4.20b}$$

$$= \exp\left(-i\frac{\pi}{2}\sum_{k=1}^{3}\sigma_y^k\right)\cdot\exp(-i\hat{H}^{\mathrm{int}}\Delta t)\cdot\exp\left(i\frac{\pi}{2}\sum_{k=1}^{3}\sigma_y^k\right) \tag{3-4.20c}$$

$$= \exp\left(i\frac{\pi}{2}\sum_{k=1}^{3}\sigma_y^k\right)\cdot\exp(-i\hat{H}^{\mathrm{int}}\Delta t)\cdot\exp\left(-i\frac{\pi}{2}\sum_{k=1}^{3}\sigma_y^k\right) \tag{3-4.20d}$$

If you do not consider global phase, any patterns of π pulses with the same direction are permitted. The time evolution $\exp(-i\hat{H}^{zz}\Delta t)$ in individual rotating frame is simulated by Eqs. (3-4.21), and the example of pulse sequences is shown in Figure 3-4.5.

$$\exp(-i\hat{H}^{zz}\Delta t) = \exp(-i\hat{H}^{\text{int},-s}\Delta t/2)\cdot\exp(-i\hat{H}^{\text{int}}\Delta t/2) \quad \text{(3-4.21a)}$$

$$= \exp(-i\hat{H}^{\text{int}}\Delta t/2)\cdot\exp(-i\hat{H}^{\text{int},-s}\Delta t/2) \quad \text{(3-4.21b)}$$

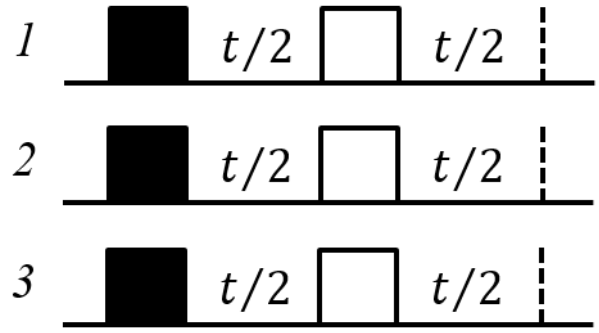

Figure 3-4.5. Simulations of $\exp(-i\hat{H}^{zz}\Delta t)$ by Eq. (3-4.20a) and (3-4.21b) in three spin systems.

3-4-3. Simulations of Three Qubit Interactions and Higher Order Qubit Interactions

Simulations of Three Qubit Interactions

Generally UQG can simulate *n* qubit interactions. Here, we discuss a 3 qubit interaction[19] which appears in the 3-qubit algorithm of AQC. Three qubit interaction is decomposed by following procedure in Eqs. (3-4.22).

$$\exp(-i\alpha^{12}\sigma_z^1\sigma_z^2\sigma_z^3 t) = \exp\left(-i\frac{\pi}{4}\sigma_x^1\right)\cdot\exp(-i\alpha^{12}\sigma_y^1\sigma_z^2\sigma_z^3 t)\cdot\exp\left(i\frac{\pi}{4}\sigma_x^1\right) \quad \text{(3-4.22a)}$$

$$= \exp\left(-i\frac{\pi}{4}\sigma_x^1\right)\cdot\exp\left(i\frac{\pi}{4}\sigma_x^1\sigma_z^3\right)\cdot\exp(-i\alpha^{12}\sigma_z^1\sigma_z^2 t)\cdot\exp\left(-i\frac{\pi}{4}\sigma_x^1\sigma_z^3\right)\cdot\exp\left(i\frac{\pi}{4}\sigma_x^1\right) \quad \text{(3-4.22b)}$$

$$= \exp\left(-i\frac{\pi}{4}\sigma_x^1\right)\cdot\exp\left(-i\frac{\pi}{4}\sigma_y^1\right)\cdot\exp\left(i\frac{\pi}{4}\sigma_z^1\sigma_z^3\right)\cdot\exp\left(i\frac{\pi}{4}\sigma_y^1\right)\cdot\exp(-i\alpha^{12}\sigma_z^1\sigma_z^2 t)$$

$$\cdot\exp\left(-i\frac{\pi}{4}\sigma_y^1\right)\cdot\exp\left(-i\frac{\pi}{4}\sigma_z^1\sigma_z^3\right)\cdot\exp\left(i\frac{\pi}{4}\sigma_y^1\right)\cdot\exp\left(i\frac{\pi}{4}\sigma_x^1\right) \quad \text{(3-4.22c)}$$

The Eq. (3-4.22c) contains only two components: the single qubit rotations and two qubit interactions, thus the equation has a fully decomposed form to simulate 3-qubit interactions for the pulse sequence studies. As the preparation to the following subsection (see fast simulations for two qubit interaction between nuclei), we denote the other two expressions of Eqs. (3-4.23) to (3-4.26) which are the permutation of Eq. (3-4.22c).

$$= \exp\left(-i\frac{\pi}{4}\sigma_x^2\right)\cdot\exp\left(-i\frac{\pi}{4}\sigma_y^2\right)\cdot\exp\left(i\frac{\pi}{4}\sigma_z^1\sigma_z^2\right)\cdot\exp\left(i\frac{\pi}{4}\sigma_y^2\right)\cdot\exp(-i\alpha^{12}\sigma_z^2\sigma_z^3 t)$$

$$\cdot\exp\left(-i\frac{\pi}{4}\sigma_y^2\right)\cdot\exp\left(-i\frac{\pi}{4}\sigma_z^1\sigma_z^2\right)\cdot\exp\left(i\frac{\pi}{4}\sigma_y^2\right)\cdot\exp\left(i\frac{\pi}{4}\sigma_x^2\right) \quad \text{(3-4.23)}$$

$$t = \alpha^{23} t' / \alpha^{12} \tag{3-4.24}$$

$$= \exp\left(-i\frac{\pi}{4}\sigma_x^3\right)\cdot\exp\left(-i\frac{\pi}{4}\sigma_y^3\right)\cdot\exp\left(i\frac{\pi}{4}\sigma_z^2\sigma_z^3\right)\cdot\exp\left(i\frac{\pi}{4}\sigma_y^3\right)\cdot\exp(-i\alpha^{12}\sigma_z^1\sigma_z^3 t)$$

$$\cdot\exp\left(-i\frac{\pi}{4}\sigma_y^3\right)\cdot\exp\left(-i\frac{\pi}{4}\sigma_z^2\sigma_z^3\right)\cdot\exp\left(i\frac{\pi}{4}\sigma_y^3\right)\cdot\exp\left(i\frac{\pi}{4}\sigma_x^3\right) \tag{3-4.25}$$

$$t = \alpha^{13} t' / \alpha^{12} \tag{3-4.26}$$

Note that time *t'* and *t''* can range to negative values. In the negative case, simulate inverse sign two qubit interactions as discussed in subsection 3-4-2, and then sign of time changes into the positive value. The same approach is also applied for the simulation of $\exp(i\alpha^{12}\sigma_z^1\sigma_z^2\sigma_z^3 t)$. The examples of pulse sequence of Eq. (3-4.22c) with Eqs. (3-4.12b), (3-4.13b) and (3-4.15b) are shown in Figure 3-4.6. In this pulse sequence, the sign of α^{13}, coupling constants of 1st and 3rd spins, are assumed to be as positive.

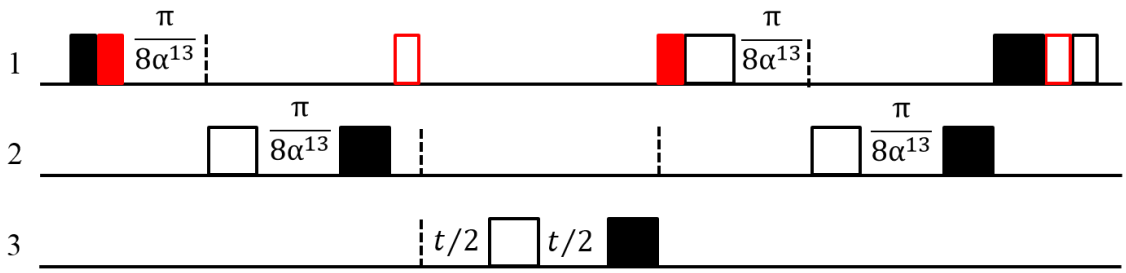

Figure 3-4.6 A pulse sequence for the simulations of a three spin interaction. The qubit operation $\exp(-i\alpha^{12}\sigma_z^1\sigma_z^2\sigma_z^3 t)$ is decomposed by Eqs. (3-4.12b), (3-4.13b), (3-4.15b) and (3-4.22c). $\alpha^{13} > 0$ is assumed in the generation of the pulse sequence.

Simulations of Higher (*n* > 3) Qubit Interactions

The higher qubit interaction (*n* > 3) is also possible to generate with the same procedure of the 3-qubit interaction. Repeating the decomposition, *n*-qubit interactions are simulated and the computational costs of *n*-qubit interactions are estimated to be 2n+1 times higher than that of two qubit operation. The example of four qubit interaction is shown in Eq. (3-4.27).

$\exp(-i\alpha^{12}\sigma_z^1\sigma_z^2\sigma_z^3\sigma_z^4 t)$

$$= \exp\left(-i\frac{\pi}{4}\sigma_x^1\right)\cdot\exp\left(-i\frac{\pi}{4}\sigma_y^1\right)\cdot\exp\left(i\frac{\pi}{4}\sigma_z^1\sigma_z^4\right)\cdot\exp\left(i\frac{\pi}{4}\sigma_y^1\right)\cdot\exp(-i\alpha^{12}\sigma_z^1\sigma_z^2\sigma_z^3 t)$$

$$\cdot\exp\left(-i\frac{\pi}{4}\sigma_y^1\right)\cdot\exp\left(-i\frac{\pi}{4}\sigma_z^1\sigma_z^4\right)\cdot\exp\left(i\frac{\pi}{4}\sigma_y^1\right)\cdot\exp\left(i\frac{\pi}{4}\sigma_x^1\right) \tag{3-4.27}$$

3-4-4. Simulation Techniques for Fast Two Qubit Interactions between Nuclei

Two spin interactions between nuclei (< kHz) are much smaller than those between electrons (~ MHz) and between an electron and a nucleus (~ MHz). The small interactions in spin Hamiltonian slows down the computational speed of quantum computer below kHz. In order to conserve the computational speed about MHz, I employed the following equation. Let me assume the 1-electron and 2-nuclear system and the nuclei 2 and 3 have only weak or no interaction. Transforming Eqs. (3-4.22c) and (3-4.23), the spin interaction between nuclei is achieved without utilizing its direct interaction in Eq. (3-4.28).

$$\begin{aligned}\exp(-i\alpha^{12}\sigma_z^2\sigma_z^3 t) = {} & \exp\left(-i\frac{\pi}{4}\sigma_y^2\right)\cdot\exp\left(-i\frac{\pi}{4}\sigma_z^1\sigma_z^2\right)\cdot\exp\left(i\frac{\pi}{4}\sigma_y^2\right)\cdot\exp\left(i\frac{\pi}{4}\sigma_x^2\right)\cdot\exp\left(-i\frac{\pi}{4}\sigma_x^1\right) \\ & \cdot\exp\left(-i\frac{\pi}{4}\sigma_y^1\right)\cdot\exp\left(i\frac{\pi}{4}\sigma_z^1\sigma_z^3\right)\cdot\exp\left(-i\alpha^{12}\sigma_z^1\sigma_z^2 t\right)\cdot\exp\left(-i\frac{\pi}{4}\sigma_y^1\right)\cdot\exp\left(-i\frac{\pi}{4}\sigma_z^1\sigma_z^3\right)\cdot\exp\left(i\frac{\pi}{4}\sigma_y^1\right) \\ & \cdot\exp\left(i\frac{\pi}{4}\sigma_x^1\right)\cdot\exp\left(-i\frac{\pi}{4}\sigma_x^2\right)\cdot\exp\left(-i\frac{\pi}{4}\sigma_y^2\right)\cdot\exp\left(i\frac{\pi}{4}\sigma_z^1\sigma_z^2\right)\cdot\exp\left(i\frac{\pi}{4}\sigma_y^2\right)\end{aligned} \tag{3-4.28}$$

The right side of Eq. (3-4.28) does not contain the interaction between 2nd and 3rd spins. The equation costs much number of single and two qubit interactions but possible to be performed with high computational speed about MHz. The same approach is also applied for the simulations of $\exp(i\alpha^{12}\sigma_z^1\sigma_z^2\sigma_z^3 t)$. The example pulse sequence of Eq. (3-4.28) with Eqs. (3-4.12b), (3-4.13b) and (3-4.15b) is shown in Fig. 3-4.7. In this pulse sequence, the signs of α^{12} and α^{13} are assumed to be positive.

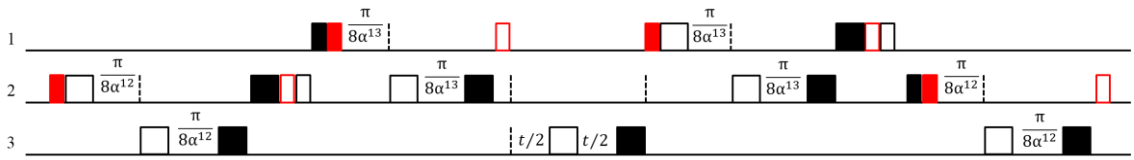

Figure 3-4.7. A pulse sequence simulating a two spin interaction between the nuclei. The operation $e^{-\alpha^{12}\sigma_z^2\sigma_z^3 t}$ is composed of Eqs. (3-4.12b), (3-4.13b), (3-4.15b) and (3-4.28). $\alpha^{12},\alpha^{13}>0$ are assumed at the pulse sequence decomposition.

3-4-5. AQC Pulse Sequences

AQC Pulse Sequence in 3-electron System

The pulse operations of each Hamiltonian term of AQC are described above subsection. Here, I write down the whole sequence toward the adiabatic factorization problem of 21. The connected pulse sequence is conquered in the case that all spin interactions are negative (Fig. 3-4.8), corresponding to

the case of the spin Hamiltonian of a phthalocyanine derivative molecule as described in subsection 3-5-1.

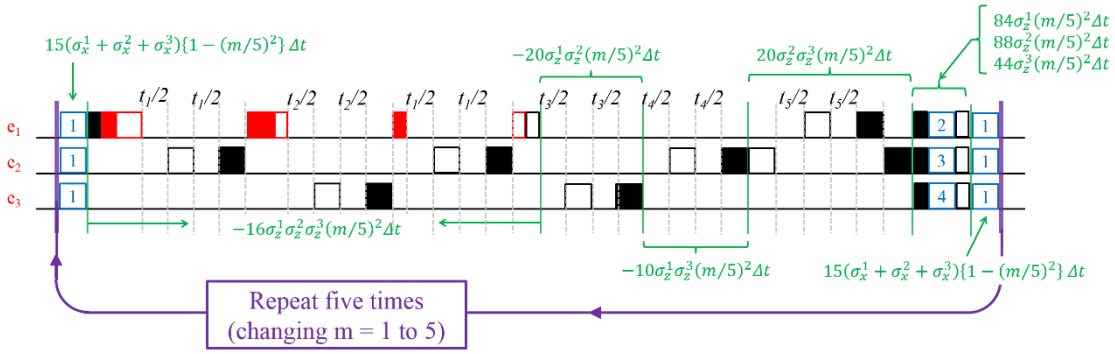

Figure 3-4.8 A pulse sequence for a 3-electron system which coupling constants are $\alpha^{12},\alpha^{23},\alpha^{31}<0$. This sequence requires five time repetition with changing the value of m = 1 to 5 (see subsection 3-2-4), where Δt = 0.028. The details of pulse intervals (t_1 to t_5) and blue blocks are described in Table 3-4.2 and 3-4.3.

Table 3-4.2 Analytical pulse intervals (t_1 to t_5) in the 3-electron system, where $a_{\mathrm{m}}=0.028(m/5)^2$.

Interval	t_1	t_2	t_3	t_4	t_5
Analytical time /s	$-\pi\eta/(D_{zz}+J)^{13}$	$-64a_m/(D_{zz}+J)^{12}$	$-80a_m/(D_{zz}+J)^{12}$	$-40a_m/(D_{zz}+J)^{13}$	$-80a_m/(D_{zz}+J)^{23}$

Table 3-4.3 Analytical operation angles and directions (Block 1 to 5) in the 3-electron system, where $b_{\mathrm{m}}=0.028\{1-(m/5)^2\}$ and $c_{\mathrm{m}}=0.028(m/5)^2$.

Pulse block	1	2	3	4	5
Angle /rad	$30b_{\mathrm{m}}$	$168c_{\mathrm{m}}$	$176c_{\mathrm{m}}$	$88c_{\mathrm{m}}$	$30b_{\mathrm{m}}+\pi/2$
Direction	x	y	y	y	x

AQC Pulse Sequence in 1-electron and 2-nuclear System

As the same as the 3-electron system case, the whole sequence toward the adiabatic factorization problem of 21 is conquered in the 1-electron and 2-nuclear system. The connected pulse sequence is for the coupling constants of $\alpha^{12}>0,\alpha^{31}<0$ (Fig. 3-4.9), corresponding to the case of the spin Hamiltonian of a glutaconic acid radical as described in subsection 3-5-2.

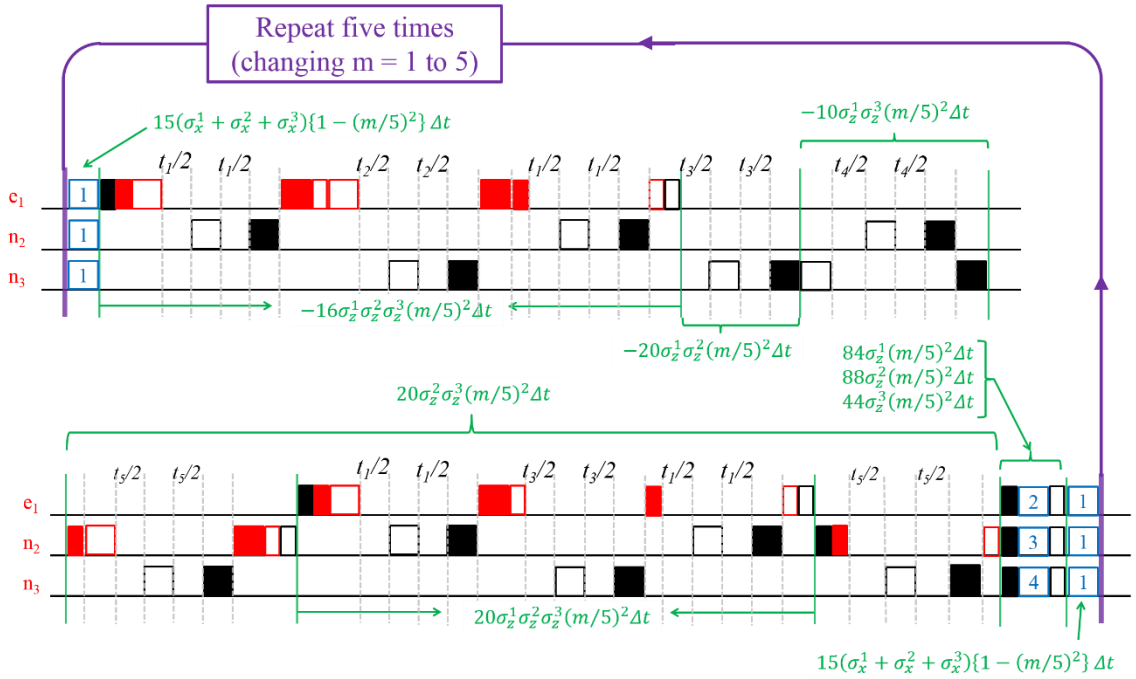

Figure 3-4.9. A pulse sequence for a 1-electron and 2-nuclear system. The coupling constants are $\alpha^{12}>0, \alpha^{31}<0$. The sequence requires five time repetitions with changing m = 1 to 5 (see subsection 3-2-4), where Δt = 0.028. The details of pulse interval (t_1 to t_5) and blue blocks are shown in Table 3-4.4 and 3-4.5.

Table 3-4.4. Analytical pulse interval (t_1 to t_5) in the 1-electron and 2-nuclear system, where, $a_m = 0.028\eta(m/5)^2$.

Interval	t_1	t_2	t_3	t_4	t_5
Analytical time /s	$-\pi\eta/A_{zz}^{13}$	$64a_m/A_{zz}^{12}$	$80a_m/A_{zz}^{12}$	$-40a_m/A_{zz}^{13}$	$\pi\eta/A_{zz}^{12}$

Table 3-4.5. Analytical operation angles and directions (Block 1 to 5) in the 1-electron and 2-nuclear system, where $b_m = 0.028\{1-(m/5)^2\}$ and $c_m = 0.028(m/5)^2$.

Pulse block	1	2	3	4	5
Angle /rad	$30b_m$	$168c_m$	$176c_m$	$88c_m$	$30b_m+\pi/2$
Direction	x	y	y	y	x

3-4-6. Discussion of Analytical Sequence Calculations.

In this subsection, I described sequence calculation methods with SAA Hamiltonian. Since single spin rotations are assumed for x-/y-directions, the simulations of single qubit rotations are calculated with simple methods. However, the simulations between qubit interactions requires some pulses and time evolution parts. The basics of simulating qubit interactions are to simulate arbitrary two qubit interactions discussed in subsection 3-4-2. If it was done, the following technique discussed in subsection 3-4-3 to 3-4-5 can generate pulse sequences which have a capability to perform any AQUA.

Expansion for non-SAA Hamiltonian is also possible by replacement of pulse calculation technique of two qubit interactions as discussed in subsection 3-4-2. More accurate approximation of spin Hamiltonian can provide better quality of time evolution for ESR-AQC experiments. However, these approaches require a larger pulse operation number in general in order to annihilate off-diagonal elements of spin Hamiltonian.

3-5. Pulse Sequence of 3-qubit AQC with Single Crystal Systems

In this section, I present the pulse sequences analytically calculated from the section above. All the detail results in pulse sequences are shown in this section. Contents are:

3-5-1. Pulse sequence of 3-qubit AQC with a single crystal of a phthalocyanine derivative[4]

3-5-2. Pulse sequence of 3-qubit AQC with a single crystal of a glutaconic acid radical[20]

3-5-3. Pulse sequence of 2-qubit AQC with a single crystal of a biradical **1**[21]

3-5-4. Pulse sequence of 2-qubit AQC with a single crystal of a malonic acid radical[22]

In the last subsection 3-5-5, I discussed the feature of pulse sequences toward ESR-AQC.

3-5-1. Pulse Sequence of 3-qubit AQC with a Single Crystal of a Phthalocyanine Derivative

A phthalocyanine derivative[4] is adopted for a 3-electron qubit system, which one electron spin is quenched by a hydrogen atom. The direction of static magnetic field is selected in order to make the system have strong spin interactions, and the resultant coupling constants with respect to subsection 3-3-3 and the direction is shown in Table 3-5.1 and Fig. 3-5.1. The *J* couplings and *D* tensors are calculated by quantum chemical calculations (UB3LYP/6-31G* level) based on an expanded broken symmetry methods and point dipole approximation with the optimized structure.

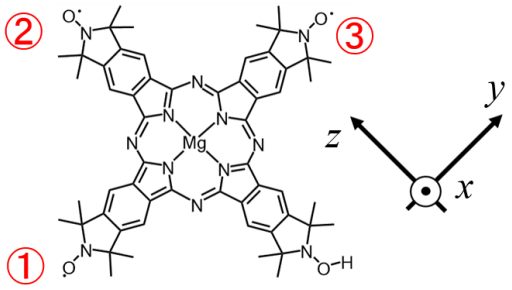

Figure 3-5.1. A molecular structure of a phthalocyanine derivative. One radical sites are designated by the red numbers. The magnetic field is applied from *z*-direction.

Table 3-5.1. Interaction strengths between spin sites estimated by theoretical calculations.

	1-2	2-3	3-1
J /MHz	-12.01	-12.01	-66.03
θ /rad	$5\pi/4$	$-5\pi/4$	$\pi/2$
D_{zz} /MHz	−16.55	−16.55	11.71
$(D_{zz}+J)$ /MHz	−28.56	−28.56	−54.32

A pulse sequence shown in Fig. 3-5.2 is simplified from the sequence of subsection 3-4-5 by connecting same type of pulses neighboring. This technique does not change the computational time but reduce the number and total angles of spin rotations. The notation is the same as the sequence of subsection 3-4-5, and the new parameters and the numerical values are shown in Table 3-5.2.

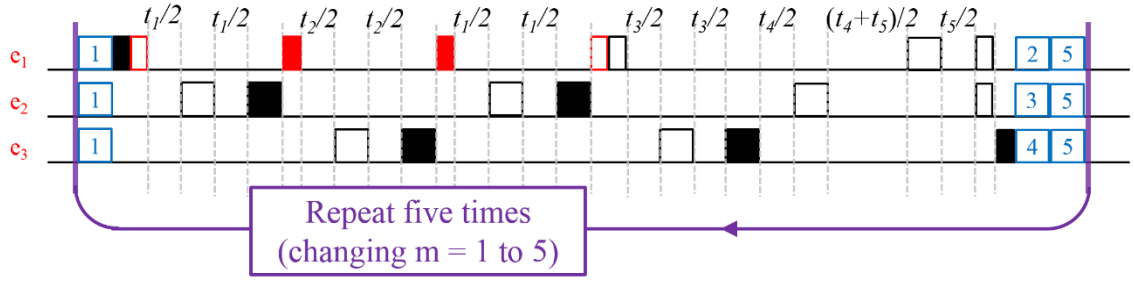

Figure 3-5.2. A pulse sequence for a phtalocyanine derivative. The magnetic field is applied from *z*-direction. The parameters of time intervals and pulse rotations are shown in Table 3-5.2.

Table 3-5.2. Analytical pulse intervals and rotation angles. (a) Analytical pulse intervals with interaction values of systems in $(D_{zz} + J)^{ij} < 0$. (b) Analytical pulse intervals in the phthalocyanine derivative. (c) Analytical pulse rotation angles and directions.

(a) Analytical pulse intervals in $(D_{zz} + J)^{ij} < 0$

Interval	t_1	t_2	t_3	t_4	t_5
Analytical time /s	$-\pi/(D_{zz}+J)^{13}$	$-64a_m/(D_{zz}+J)^{12}$	$-80a_m/(D_{zz}+J)^{12}$	$-40a_m/(D_{zz}+J)^{13}$	$-80a_m/(D_{zz}+J)^{23}$

(b) Analytical pulse intervals in the phthalocyanine derivative

Intervals	t_1	t_2	t_3	t_4	t_5
Analytical value /ns	9.158	0.4017	0.5021	0.1306	0.5021

(c) Analytical pulse rotation angles and directions

Pulse block	1	2	3	4	5
Angle /rad	$30b_m$	$168c_m$	$176c_m$	$88c_m$	$30b_m+\pi/2$
Direction	x	y	y	y	x

As a result, the pulse sequence is composed of 140 pulses, which totally rotates electron 1, 2 and 3 for 29.8π, 35.0π and 28.2π radians, respectively. The computational time is 0.176 μs. Since the experiments of the 3-nuclear spin QC took 50 ms with 95 pulses, the 3-electron spin QC can improve the computational time about 2.84×10^5 times. The results are shown in Table 3-5.3.

Table 3-5.3. Total operation angles of each spin and required time with Fig. 3-5.2.

Qubits	e_1	e_2	e_1
Operation angles /rad	29.8π	35.0π	28.2π
Required time /μs	0.176		

3-5-2. Pulse Sequence of 3-qubit AQC with a Single Crystal of a Glutaconic Acid Radical

In the 1-electron and 2-nuclear system, a 2-deuterated glutaconic acid radical (e_1, H_2 and H_3)[20] are adopted due to the coaxial properties in two hyperfine tensors. The interaction parameters of the system are utilized the set of ESR experiments of the glutaconic acid radical, where $A_{zz}^{12} = +7.0$ MHz and $A_{zz}^{31} = -37.9$ MHz.[20] The direction of magnetic field is parallel to one of the hyperfine coaxes as shown in Fig. 3-5.3.

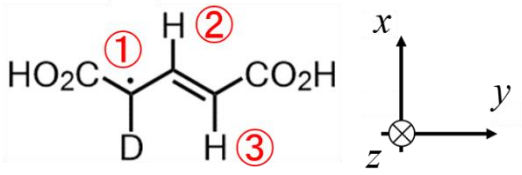

Figure 3-5.3. A molecular structure of a glutaconic acid radical. One hydrogen is deuterated and the direction of the static magnetic field and one of principal coaxes of hyperfine tensors is along the *z*-direction. The coupling constants between the electron and 2nd and 3rd hydrogen nuclei are +7.0 MHz and −36.0 MHz, respectively.

A pulse sequence shown in Fig. 3-5.4 is simplified from the sequence of subsection 3-4-5 by connecting same type of pulses neighboring. The parameters are shown in Table 3-5.4 and in subsection 3-4-5, in which numerical values are also shown.

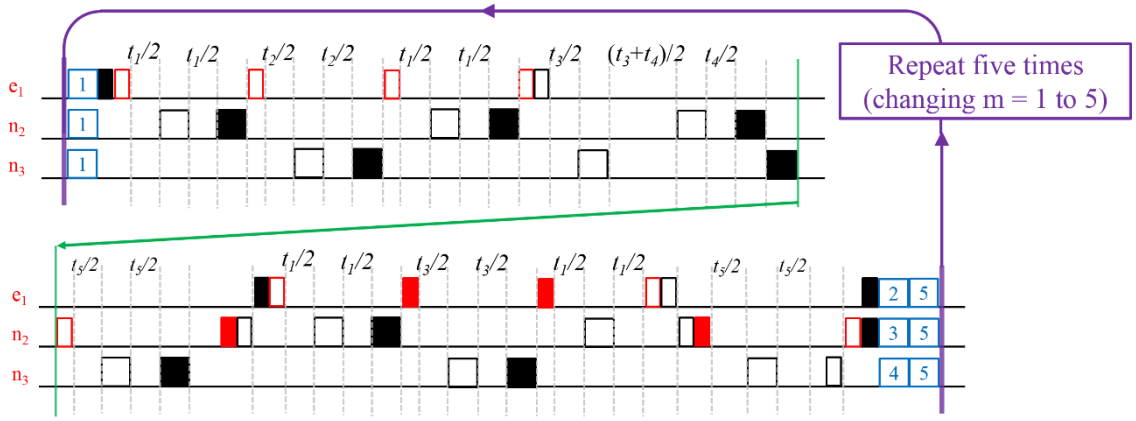

Figure 3-5.4. A pulse sequence for a glucotanic acid radical. The magnetic field is applied from *z*-direction. The parameters of time intervals and pulse rotations are shown in Table 3-5.4.

Table 3-5.4. Analytical pulse intervals and rotation angles. (a) Analytical pulse intervals with interaction values of systems in $A^{12} > 0$ and $A^{13} < 0$. (b) Analytical pulse intervals in the glucotanic acid radical. (c) Analytical pulse rotation angles and directions.

a) Analytical pulse intervals in $A^{12} > 0$ and $A^{13} < 0$

Interval	t_1	t_2	t_3	t_4	t_5
Analytical time /s	$-\pi / A_{zz}^{13}$	$64a_m / A_{zz}^{12}$	$80a_m / A_{zz}^{12}$	$-40a_m / A_{zz}^{13}$	π / A_{zz}^{12}

b) Analytical pulse intervals in the glucotanic acid radical

Interval	t_1	t_2	t_3	t_4	t_5
Analytical value /ns	13.89	1.630	2.037	0.1981	71.43

c) Analytical pulse rotation angles and directions

Pulse block	1	2	3	4	5
Angle /rad	$30b_m$	$168c_m$	$176c_m$	$88c_m$	$30b_m + \pi/2$
Direction	x	y	y	y	x

As a result, the pulse sequence is composed of 240 pulses, which totally rotates electron and nuclei 1, 2 and 3 for 39.8π, 70.0π and 53.2π radians, respectively. The computational time is 1.31 μs. Since the experiments of the 3-nuclear spin QC took 50 ms with 95 pulses, the 1-electron and 2-nuclear spin QC can improve the computational time about 3.82×10^4 times. The results are shown in Table 3-5.5.

Table 3-5.5. Total operation angles of each spin and required time with the sequence Fig. 3-5.4.

Qubit	e_1	n_2	n_3
Operation angles /rad	39.8π	70.0π	53.2π
Required time /μs	1.31		

3-5-3. Pulse Sequence of 2-qubit AQC with a Single Crystal of a Biradical 1

In the case of the 2-qubit algorithm, the pulse sequence is much simplified from the 3-qubit one, because there are only one spin interaction as much as AQC algorithm, i.e. no 3-qubit interaction and decrease two of the 2-qubit interactions. For the 2-electron study, biradical **1**[21] (Fig. 3-5.5) is adopted for the sequence study including 5 time repetition as shown in Fig. 3-5.6. Although whole sequences require 32 pulses, utilizing non-selecting pulses the sequence can performed with only 21 pulses. The computational time, 63 ns, is approximately twice faster than that of the 3-qubit case as shown in Table 3-5.6.

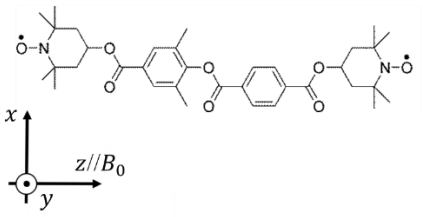

Figure 3-5.5. Biradical **1** and the static magnetic field direction. In this orientation, dipole interaction between electron spins are −18.5 MHz.

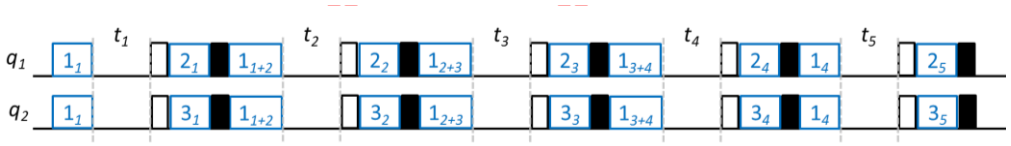

Figure 3-5.6. A pulse sequence for 2-qubit adiabatic quantum computing with molecules which interaction sign is minus. biradical **1**. Time intervals are $t_i = 60a_i/|(D_{zz}+J)^{12}|$ for the 2-electron systems and $t_i = 60a_i/|(A_{zz})^{12}|$ for the 1-electron and 1-nucleus system.

Table 3-5.6. Total operation angles and required time in biradical **1**.

Pulse type of operation	e_1	e_2	Non-selective
Operation angles /rad	0.86π	1.4π	5.8π
Required time /μs	1.31		

3-5-4. Pulse Sequence of 2-qubit AQC with a Single Crystal of a Malonic Acid Radical

A maronic acid radical (Fig. 3-5.7) is utilized for a 1-electron and 1-nucleus system.[22] Since there is no interaction in the 2-qubit systems, the pulse sequence is the same as that of the 2-electron system (Fig. 3-5.6) and there is no requirement of coaxes properties. Thus, the experiments for the system is much simplified from the 1-electron and 2-nuclear system in terms of spin rotations (see Table 3-5.7). Whole sequences are performed with 32 pulses. The computational time is 13 ns due to the strong hyperfine interaction, −91 MHz, between the electron and hydrogen nucleus.

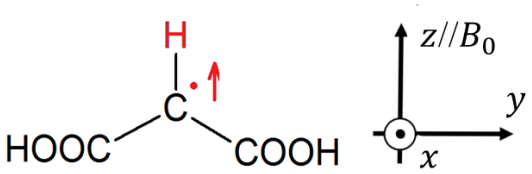

Figure 3-5.7. A maronic acid radical and the static magnetic field direction.

Table 3-5.7. Total operation angles and required time in a maronic acid radical.

Qubit	e_1	n_2
Operation angles /rad	6.7π	7.2π
Required time /μs	1.31	

3-5-5. Discussion in Pulse Sequence Study.

In section 3-5, I have calculated analytical pulse sequences in order to perform AQC with molecular spin QCs. The sequences for 2-/3-qubits with corresponding molecular qubits have different features in the required time, number of pulses and rotating angles. As a consequence, it is established that molecular spin QCs have capability to perform AQC with SAA Hamiltonian, and the sequences have fast computational ability in terms of computational time than NMR-QCs.

However, the time intervals (~ 0.1 ns) between pulses are much shorter than NMR-QCs when the same algorithms as NMR-QCs are applied into ESR-QCs due to the strength of spin interactions. Assuming standard X-band pulse ESR spectrometers (9.5 GHz), the intervals are too short to perform QC-experiments from the both experimental and theoretical points of view for the pulse control and SAA. Thus, the solving time interval problem is essential for ESR-AQCs. Note that the above issue appears particularly in AQC, but not in gate model QC approaches because pulse intervals in gate model QCs appeare in only controlled gates, e.g. CNOT gates, with the fixed amounts of time. The short time intervals are the essence of slight change in time dependent Hamiltonian of AQUA. At the following section, I discuss this problem by numerical simulations.

3-6. Numerical Simulations for AQUA

The last topic of adiabatic quantum computing is the simulations of theoretical conditions of the algorithm. This section includes two contents: 1) how to achieve high fidelity, i.e. success probability of AQC, with an adiabatic path conditions, 2) how to solve the time evolution problem discussed in section 3-5. In subsection 3-6-1, I introduce the basics of the AQC time evolution period and Trotter decomposition. Subsection 3-6-2 is concerned in the numerical simulations to find good theoretical conditions without Trotter decomposition. Since Trotter decomposition are one of the approximation methods, the feature of Trotter decomposition is discussed in subsection 3-6-3. Note that there are Trotter formulas with some arbitrary parameters. The application is the time interval problem, in which the Trotter parameters can extend time intervals (in subsection 3-6-4), and the last subsection 3-6-5 gives discussions.

3-6-1. Time Evolution Period and Trotter Decomposition in AQUA

Let me assume that evolution time, whole computational time, of AQUA ranges 0 to *T*. Time steps of AQCs are briefly described in subsection 3-2-4, and Fig. 3-6.1 depicts two evolution periods: 1) Time evolution steps of AQUA as described in Eqs. (3-2.12) and (3-2.13) and 2) Trotter decomposition steps in Eqs. (3-2.14). The Trotter steps are discussed below. Evolution periods related in steps of AQUA (*M*) and Trotter steps (*N*) are depicted in Fig. 3-6.1 with red and blue colors, respectively.

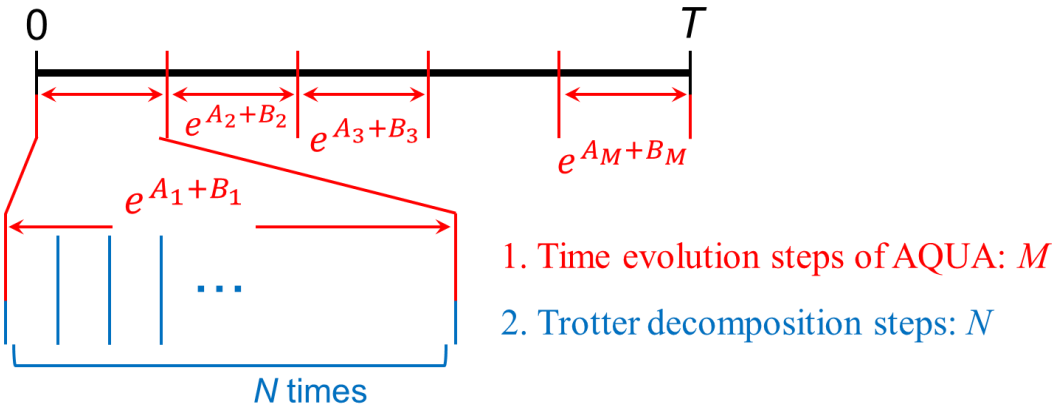

Figure 3-6.1. Two time steps in AQCs. *M* is the time evolution steps which mean the quantum computational accuracy of time evolution. *N* is Trotter decomposition steps which reflect the accuracy of the Trotter formula in each evolution time step *N*.

Trotter decompositions have several formula, in which each decomposition approximates the matrix exponential composed of non-commutative operators. Although the simple 2nd order formula (Eqs. (3-2.14) and Eq. (3-6.1a)) has been adopted in a standard AQC study, there are higher order and arbitrary parameterized formulas in Trotter decompositions (Eqs. (3-6.1)).[23]

・2nd formula

$$\mathrm{e}^{A+B} = \left[e^{A/2N} \cdot e^{B/N} \cdot e^{A/2N}\right]^N + O(N^2) \tag{3-6.1a}$$

$$\mathrm{e}^{A+B} = \left[e^{(1-\gamma)A/N} \cdot e^{B/2\gamma N} \cdot e^{\gamma A/N} \cdot e^{(1-1/2\gamma)B/N}\right]^N + O(N^2) \tag{3-6.1b}$$

・3rd formula

$$e^{A+B} = \left[e^{(1-\gamma)A/N} \cdot e^{\left(\frac{4}{3}-\gamma\pm\Gamma\right)B/2\gamma(\gamma\pm\Gamma)N} \cdot e^{(\gamma\pm\Gamma)A/2N} \cdot e^{(3-4\gamma)B/2(2-3\gamma)N} \cdot e^{(\gamma\mp\Gamma)A/2N} \cdot e^{\left(1-\left(3\gamma-\frac{4}{3}\mp\Gamma\right)/(2\gamma(\gamma\mp\Gamma))\right)B/N}\right]^N + O(N^3) \tag{3-6.1c}$$

$$\Gamma = [(-12\gamma^3 + 45\gamma^2 - 48\gamma + 16)/(-12\gamma + 9)]^{1/2} \tag{3-6.1c'}$$

・4th formula

$$e^{A+B} = \left[e^{\beta A/2N} \cdot e^{B/2\left(2-\sqrt[3]{2}\right)N} \cdot e^{\left(1-\sqrt[3]{2}\right)\beta A/2N} \cdot e^{-\sqrt[3]{2}B/N} \cdot e^{\left(1-\sqrt[3]{2}\right)\beta A/2N} \cdot e^{B/2\left(2-\sqrt[3]{2}\right)N} \cdot e^{\beta A/2N}\right]^N + O(N^{-4}) \tag{3-6.1d}$$

Note that Eqs. (3-6.1b) and (3-6.1c) have an arbitrary parameter γ which is a complex number. However, γ and Γ should be selected in a real value because the time evolution period should be composed of a set of unitary operators. Thus, One should be careful utilizing Eq. (3-6.1c) by the restriction of Eq. (3-6.1c') not to make Γ with the imaginary part.

There is another caution for Trotter orders. The order in Trotter decompositions is described with respect to N which is discussed in Fig. 3-6.1. If there is no iteration period, i.e. N = 1, higher order Trotter does not make sense. If one utilizes large N, the higher order formulas have efficiency.

The accuracy of AQC is evaluated by fidelity,[1] which represent "a distance" between two matrices.

$$F(\rho,\sigma) = \mathrm{Tr}\left[\sqrt{\sqrt{\rho}\cdot\sigma\cdot\sqrt{\rho}}\right] \tag{3-6.2}$$

Tr(A) is the trace of a matrix A. The simplest formula is given when both ρ and σ (Eq. (3-6.3a)) are pure as shown in Eq. (3-6.3b).

$$\rho = |\varphi><\varphi|, \ \ \sigma = |\psi><\psi| \tag{3-6.3a}$$

$$F(\rho,\sigma) = |<\varphi|\psi>| \tag{3-6.3b}$$

When ρ and σ are pure density matrices, the fidelity represents the overlap of wavefunction. Thus, fidelity ranges 0 to 1 and large fidelity means two matrices are well resembled. In the typical QC study as same as this study, fidelity suggests computational accuracy (f = 1 is complete accuracy of control and f = 0 is completely wrong control).

3-6-2. Time Evolution Period and Trotter Decomposition in AQUA

First numerical simulations are performed in order to estimate which adiabatic path is suitable to AQCs. Fidelity was plotted in Fig. 3-6.2, where the 3-qubit algorithm is adopted with changing parameters of time evolution steps (M) and the whole computational time (T). The detail Hamiltonian and time step are shown in Eqs. (3-6.4) and (3-6.5).

$$\hat{U} = \prod_{m=1}^{M} \exp\left(-(T/M) \times i\hat{H}_m\right) \tag{3-6.4}$$

$$\hat{H}_m = (m/M)^2 \hat{H}_{\mathrm{f}} + \{1-(m/M)^2\}\hat{H}_{\mathrm{i}} \tag{3-6.5}$$

Although there are several lines with low fidelity in Fig. 3-6.2, fidelity becomes larger with the increase of evolution steps (M) in general. The tendency of evolution steps against computational time is significant for Trotter decompositions discussed in subsection 3-6-3. The slop is smaller than 1, therefore the evolution time in each step increases against the computational time.

Figure 3-6.3 shows the small computational time (T) domain of Fig. 3-6.2. There is a region ($T \lesssim$ 0.2) in which fidelity cannot reach to 1 by increasing evolution step (M). This is the adiabatic limits. Performing AQC with fast computational time, the excitation can be occurred as mentioned in section 3-2. Figure 3-6.3 suggests that the recommended computational time (T) is larger than 0.5.

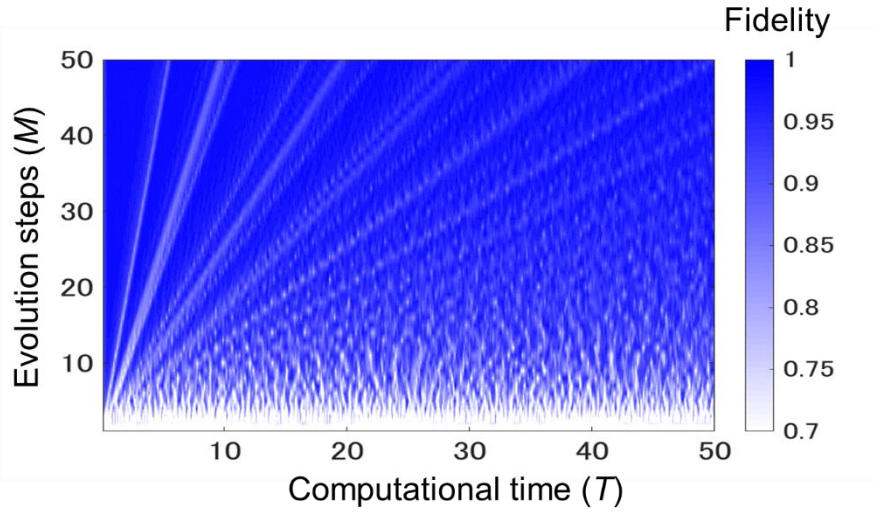

Figure 3-6.2. Fidelity plots with computational time (T) and evolution steps (M).

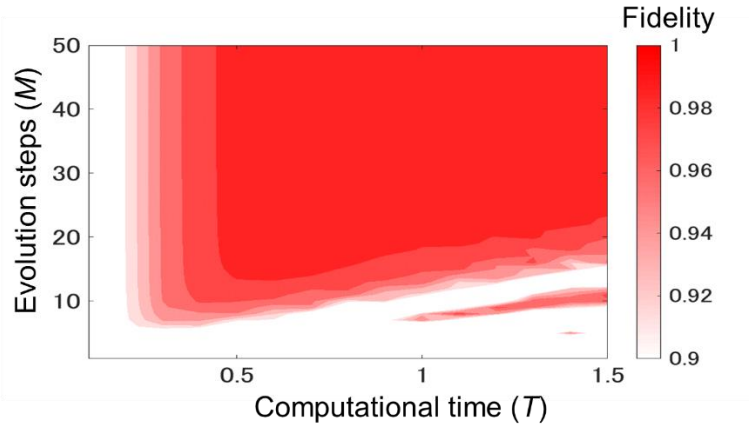

Fig. 3-6.3. Fidelity plots in low computational time (T) area with evolution steps (M).

3-6-3. Feature of Trotter Decompositions in AQUA

Accuracy of Trotter decompositions is evaluated, in which the evolution steps (M) are selected in each computational time (T) to make the fidelity of discrete adiabatic path 0.99. All the Trotter formula Eqs. (3-6.1) are utilized in the simulations. In simulations, Hamiltonian operators in Trotter formulas, A and B, are taken one or both of the following equations, which minimize the operations of H_{f}.

$$A = -i(T/M)\{1-(m/M)^2\}\hat{H}_{\mathrm{i}}, \quad B = -i(T/M)(m/M)^2\hat{H}_{\mathrm{f}} \tag{3-6.6a}$$

$$A = -i(T/M)(m/M)^2\hat{H}_{\mathrm{f}}, \quad B = -i(T/M)\{1-(m/M)^2\}\hat{H}_{\mathrm{i}} \tag{3-6.6b}$$

Since the number of A and B are same in Eqs. (3-6.6b) and (3-6.6c), both equations are utilized.

The resultant fidelity is depicted in Fig. 3-6.4 and Fig. 3-6.5 with Trotter steps $N = 1$ and $N = 4$, respectively. Comparing Fig. 3-6.5 with Fig. 3-6.4, there is a high fidelity area in low computational time region (below $T < 5$). Since Trotter decomposition is failed in the case of large exponent terms, small Trotter time steps, $(T/M)/N$, makes fidelity high (see subsection 3-6-1). Figure 3-6.5 does not make differences in the Trotter order. I therefore concluded that only the Trotter time steps are significant in these low fidelity cases.

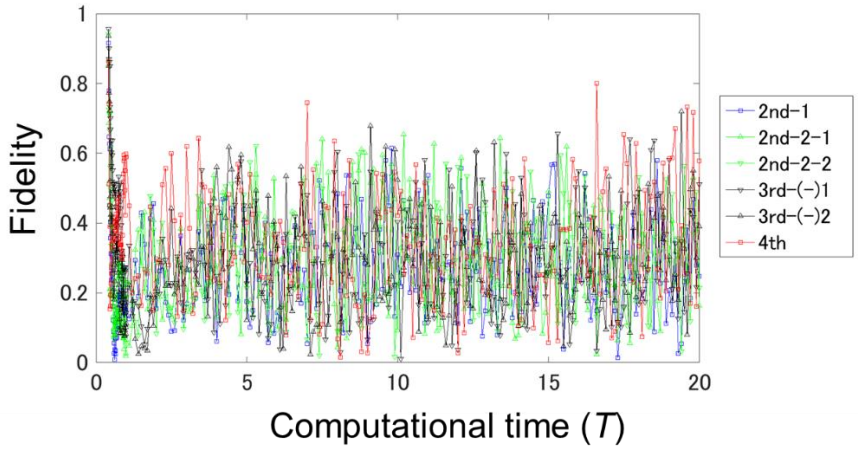

Figure 3-6.4. Fidelity plots against computational time (T) in the case of N = 1. In the calculation, evolution steps (M) is selected in order to make fidelity without Trotter decomposition 0.99.

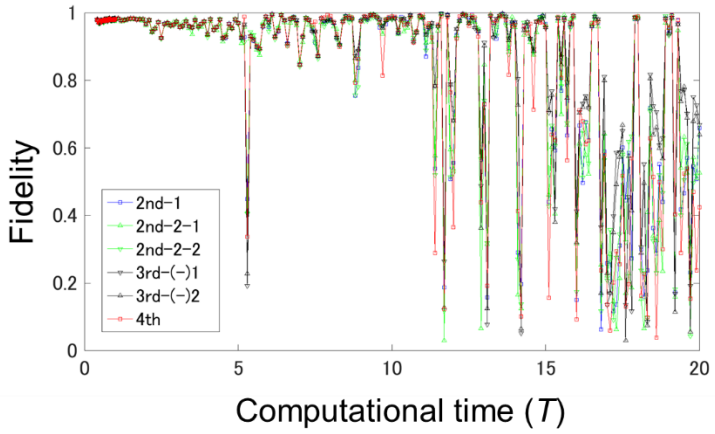

Figure 3-6.5. Fidelity plots against computational time (T) in the case of N = 4. In the calculation, evolution steps (M) is selected in order to make fidelity without Trotter decomposition 0.99.

3-6-4. Feature of Trotter Decompositions in AQUA

As discussed in section 3-5, ESR-AQCs have an experimental/theoretical problem for short time intervals in its pulse sequence. I have solved this problem by modifying AQUA of the Trotter decomposition part. Employing Eq. (3-6.1b) instead of Eq. (3-6.1a).

From: $\mathrm{e}^{A+B} = \left[e^{A/2N} \cdot e^{B/N} \cdot e^{A/2N}\right]^N + O(N^2)$ (3-6.1a)

To: $\mathrm{e}^{A+B} = \left[e^{(1-\gamma)A/N} \cdot e^{B/2\gamma N} \cdot e^{\gamma A/N} \cdot e^{(1-1/2\gamma)B/N}\right]^N + O(N^2)$ (3-6.1b)

where A and B are written as follows:

$$A = -i(T/M)(m/M)^2 \hat{H}_\mathrm{f}, \quad B = -i(T/M)\{1-(m/M)^2\}\hat{H}_\mathrm{i} \qquad (3\text{-}6.6b)$$

In numerical simulations, parameter M is set to 15 in order to improve algorithm fidelity to 0.99. Plots of γ vs fidelity are shown in Fig. 3-6.6.

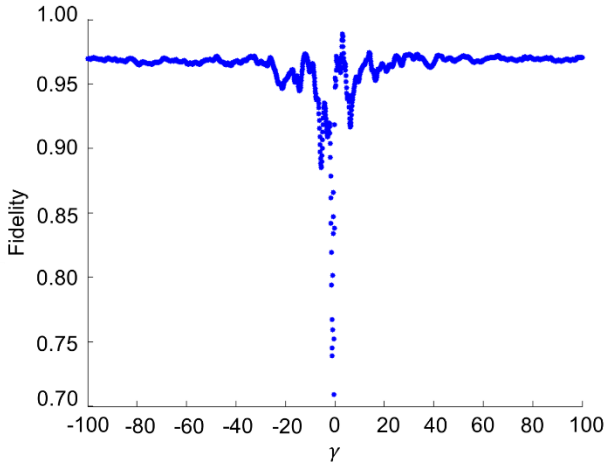

Figure 3-6.6. Scalability of time interval depicting fidelity and γ.

As shown in Fig. 3-6.6, the change of the Trotter decomposition method suggests that can expand time intervals for 99 times with enough fidelity. The low fidelity region can be caused due to the change of the adiabatic pathway. Since M = 15 is adopted, the ratio between expanded time intervals and original algorithm (M = 5) one is 33. Toward the experiments of ESR-AQC, Trotter decompositions should be carefully applied with this expansion techniques of time evolution period.

3-6-5. Discussion of Numerical Simulations for AQUA

The numerical simulations have been performed in order to discuss the AQUA of 3-qubit algorithm for factorization of 21 focusing on the discrete time evolution period (subsection 3-6-2), fidelity of Trotter formula (subsection 3-6-3) and the arbitrary parameter of Trotter formula (subsection 3-6-4). In subsection 3-6-2, discrete time evolution has simulated in terms of time evolution steps (M) and the whole computational time (T). The significant feature is that the evolution time of each step is increased if one increase T. As discussed in subsection 3-6-3, the long evolution time in each decomposed step make Trotter decompositions hard. Thus, Trotter time intervals, (T/M)/N, should be smaller by Trotter iteration number N. However, Trotter decompositions can be useful in terms of the adjustment of time intervals in pulse sequences by virtue of the arbitrary parameter (see subsection 3-6-4). As a result, I proved that the time interval problem can be solved by modifying Trotter decompositions.

3-7. Conclusions

In chapter 3, I have established experimental procedure to perform AQCs with MSOCs, which contain the adiabatic algorithm for 2-qubit systems, pulse sequence and numerical studies. The 2-qubit algorithm is developed in order to relax the difficulty of MSQC experiments with the multiplication assumption.

The most significant part of this chapter is pulse sequence calculations adopting SAA with single crystal ESR spectroscopic technique. Comparing it with the previous NMR-QC experiments, MSQCs have a capability to perform AQCs fast. However, the computational ability of MSQCs has different aspects from gate model QCs (standard QCs). Since AQCs require short time evolution in the spin systems, the intervals between pulses can be too short to manipulate both experimentally and theoretically in typical ESR conditions. Assuming X-band (9.5 GHz) ESR spectrometers, it is impossible to apply time evolution below 0.1 ns and SAA gives proper Hamiltonian in the case of much larger evolution than 0.1 ns. Thus, the time intervals related in the fast computing ability of MSQCs can cause the problem performing AQCs.

On the other hand, MSQCs have significant ability in the systems composed of electron spins with nuclear spins via hyperfine interactions. The systems can create interactions between nuclear spins, and the systems have the same order of computational speed with the systems composed of only electrons. This is the reason why both systems have faster computational ability (interaction strengths ~ MHz) than that of the NMR-QC experiments.

The numerical simulations are invoked to find the good experimental conditions, in which adiabatic path and Trotter formula are calculated. As a result, Trotter decompositions are found to be significant in AQCs because of Trotter decomposition steps. Furthermore, much larger time evolution steps are required to reach AQC fidelity 0.99 stably. Note that the problem in short time intervals is non-essential. This is because the intervals are adjustable in the Trotter decomposition process. Thus, I have overcomed all barrier of AQCs based on adiabatic computation nature.

3-8. References

[1] M. A. Nielsen and I. L. Chuang, *Quantum Computation and Quantum Information*, Cambridge University Press, **2000**.

[2] V. Ramakrishna, M. V. Salapaka, M. Dahleh, H. Rabitz, and A. Peirce, *Phys. Rev. A*, **1995**, *51*, 960; S. G. Schirmer, H. Fu, and A. I. Solomon, *Phys. Rev. A*, **2001**, *63*, 063410.

[3] C. Altafini, *J. Math. Phys*., **2002**, *43*, 2051; G. Turinici and H. Rabitz, *Chem. Phys*., **2001**, *267*, 1.

[4] S. Yamamoto, S. Nakazawa, K. Sugisaki, K. Sato, K. Toyota, D. Shiomi, T. Takui, *Phys. Chem. Chem. Phys.*, **2015**, *17*, 2742-2749.

[5] N. Khaneja, T. Reiss, C. Kehlet, T. Schulte-Herbrüggen, and S. J. Glaser, *J. Magn. Reson*., **2005**, *172*. 296-305.

[6] P. W. Shor, *SIAM J.Sci.Statist.Comput.*, **1997**, *26*, 1484-1509.

[7] X.-H. Peng, Z. Liao, N. Xu, G. Qin, X. Zhou, D. Suter and J. Du, *Phys. Rev. Lett.*, **2008**, *101*, 220405.

[8] N. Xu, J. Zhu, D. Lu, X. Zhou, X. Peng, J. Du, *Phys. Rev. Lett*. **2012**, *108*, 130501.

[9] M. Yu. Volkov, K. M. Salikhov, *Appl. Magn. Reson.,* **2011**, *41*, 145-154.

[10] E. Farhi, J. Goldstone, S. Gutman and M. Sipser, arXiv:quant-ph/0001106.

[11] R. Raussendorf, D.E. Browne, H.J. Briegel, *Phys. Rev. A.*, **2003**, *68*, 022312.

[12] C. Nayak, S. Simon, A. Stern, S. Das Sarma, *Rev. Mod. Phys.*, **2008**, *80*, 1083.

[13] J. Roland, N. J. Cerf, *Phys. Rev. A*., **2002**, *65*, 042308.

[14] D. Aharonov, W. van Dam, J. Kempe, Z. Landau, S. Lloyd, O. Regev, *SIAM J. Comput*., **2007**, *37*, 166-194.

[15] S. P. Jordan, E. Farhi, P. W. Shor, *Phys. Rev. A.*, **2006**, *74*, 052322.

[16] *OBJECT-ORIENTED MAGNETIC RESONANCE; Classes and Objects, Calculations and Computations*, eds. M. Mehring and V. A. Weberruss, ACADEMIC PRESS, San Diego, **2001**.

[17] M. M. Maricq, *Phys. Rev. B*., **1982**, *25*, 6622; A. Llor, *Chem. Phys. Lett*., **1993**, *204*, 217.

[18] P. P. Borbat, J. H. Freed, *Structural Information from Spin-Labels and Intrinsic Paramagnetic Centres in the Biosciences Structure and Bonding*, Springer, **2013**, *152*, 1-82.

[19] C. H. Tseng, S. Somaroo, Y. Sharf, E. Knill, R. Laflamme, T. F. Havel and D. G. Cory, *Phys. Rev. A.,* **1993**, *61*, 012302.

[20] H. R. Falle and M. A. WhiteheaA, *Can. J. Chem*., 1972, **50**, 139-151; C. Heller and T. Cole. *J. Chem. Phys*., 1962, **37**,243-250.

[21] S. Nakazawa, S. Nishida, T. Ise, T. Yoshino, N. Mori, R. Rahimi, K. Sato, Y. Morita, K. Toyota, D. Shiomi, M. Kitagawa, H. Hara, P. Carl, P. Höfer and T. Takui, *Angew. Chem. Int. Ed.*, **2012**, *51*, 9860-9864.

[22] H. M. McConnell, C. Heller, T. Cole, R. W. Fessenden, *J. Am. Chem. Soc.*, **1960**, *82*,766

[23] W. Janke, T. Sauer, *Phys. Lett. A.*, **1992**, *165*, 199-205.

Chapter 4

Nuclear Spin State Control with Microwave Irradiation to an Unpaired Electron by GRAPE Simulation Approach

4-1. Introduction

A quantum state control is the most significant part in QC experiments since any QC models control physical reality in quantum nature. Controllability is known as one aspect of quantum state control described by Lie algebra,[1] and the complete controllability allows quantum system to perform universal quantum gate, abbreviated as UQG.[1] Since QCs require any special unitary control (SU(N_d)) of quantum systems, UQG and complete controllability are essential for QCs composed of N_d dimension of Hilbert space. As described in chapter 1, in order to acquire controllability of MSQCs, spin Hamiltonian engineering has been investigated, i.e. *g*-tensor,[2] pseudo *g*-tensor,[3] *A*-tensor[4] and *D*-tensor[2] engineering, which enable to distinguish qubits with adjusting interaction strength between spins.

However, there are other aspects of a state control since controllability cannot predict the control procedure and required control time while it can predict whether the system is controllable or not.[1, 5] The control procedure and difficulty must be proven in another theory. Although there are analytical and numerical methods to calculate a concrete quantum pathway, analytical one has a limitation of analyzable equations (see chapter 3). Therefore, numerical optimized pulses give significant perspective of control difficulty.

Recently, Krotov[6-8] and GRAPE[9-13] numerical pulses/pulse sequences have been developed as the powerful tools for QC experiments. Both approaches optimize time dependent irradiation wave amplitude with fixed frequency pulses in magnetic resonance. Since Krotov approach arose in 1983,[6] Krotov theory in NMR has been studied for dynamical nuclear polarization (DNP)[7] and magnetic resonance imaging (MRI)[8]. However, experiments of Krotov approach are few due to the pulse optimization method.[6-8] While Krotov approach optimizes pulses in stepwise about time,[6] GRAPE approach optimizes pulses with a global manner in time.[10] The GRAPE approach has been applied to Deutsch-Jozsa algorithm[11] and AQUA[12] of factoring 143 by using molecular systems, ^{13}C- labeled crotonic acid and 1-Bromo-2-Chlorobenzene, respectively. In terms of MSQCs, there is one of the most sophisticated experiments for a CNOT gate between the electron and nucleus and simulations of ^{13}C-labeled malonyl radical aiming indirectly control by microwave.[13] It is noteworthy that those experiments are hard with analytical pulses due to the analyzable equations.

In this chapter, I have established molecular design in order to control molecular spins with pulses numerically simulated, where two nuclear spins are controlled by microwave GRAPE pulses, i.e. the indirect state control is invoked by pulsed ESR spectroscopy. Although the controllability is known for the system, control difficulty has not been described yet. Thus, control difficulty depending on molecular orientations and the molecular optimization for numerical pulses are investigated.

4-2. Theory

Theoretical approaches related to numerical simulations are given in this section. In subsection 4-2-1 and 4-2-2, spin Hamiltonian and Hamiltonian parameters of one electron and two nuclear systems are described, respectively. Controllability of the spin qubits is mentioned in subsection 4-2-3 and importance of hyperfine tensor parameters is noted. A GRAPE method is briefly introduced in subsection 4-2-4, and the computational conditions are shown in subsection 4-2-5.

4-2-1. Spin Hamiltonian in One Electron and Two Nuclear Systems.

Here, I discuss spin Hamiltonian of one electron and two nuclear spin systems with microwave irradiation and SAA[14] (see chapter 3) was applied only for the electron. A generalized Hamiltonian is described in Eq. (4-2.1), where H_0 and H_{ctrl} are time independent, and an open-shell molecular part of Hamiltonian (molecular Hamiltonian) and a control pulse part of Hamiltonian (control Hamiltonian), respectively.

$$H(t) = H_0 + c(t)H_{ctrl} \tag{4-2.1}$$

The coefficient c (t) is the time dependent control amplitude of the pulse part, which is automatically adjusted by the GRAPE optimization process. Eq. (4-2.2) is derived from analogue procedure as described at subsection 3-3-4 in chapter 3. Each term is,

$$\begin{aligned} H_0 = {} & (\omega_0(B_0) - \omega_{\mathrm{MW}})S_Z - \gamma_{n1}B_0I_Z^1 - \gamma_{n2}B_0I_Z^2 \\ & + 2\pi(A_{ZX}^1 S_Z I_X^1 + A_{ZY}^1 S_Z I_Y^1 + A_{ZZ}^1 S_Z I_Z^1) + 2\pi(A_{ZX}^2 S_Z I_X^2 + A_{ZY}^2 S_Z I_Y^2 + A_{ZZ}^2 S_Z I_Z^2) \end{aligned} \tag{4-2.2}$$

$$H_{ctrl} = \omega_1 S_X \tag{4-2.3}$$

where, Zeeman terms in Eq. (4-2.2) are composed of the microwave frequency ($\omega_{\mathrm{MW}}/2\pi$), the strength of a static magnetic field (B_0 // Z), Zeeman frequency ($\omega_0(B_0)/2\pi$), and nuclear gyromagnetic ratios γ_{n1}, and S and I^{k} denote spin operator of the electron and k$^{\mathrm{th}}$ nucleus, respectively. Here, Hamiltonian is written in unit of angular frequency (rad/s) and the hyperfine coupling constants are written in unit of frequency (Hz). The other terms in Eq. (4-2.2) are derived from anisotropy of hyperfine coupling tensors (A) between the electron and each nucleus. The microwave amplitude of $\omega_1/2\pi$ is given in Eq. (4-2.3), although the GRAPE control amplitude is automatically optimized with respect to $c(t)$.

4-2-2. Molecular Conditions.

A potassium hydrogen maleate (KHM) radical system[15] is composed of one electron spin and two hydrogen nuclear spins (^{1}H2, ^{1}H3), and a ^{13}C- labeled malonyl radical system [16] is composed of one electron spin and one hydrogen and ^{13}C nuclear spins (^{1}H2, ^{13}C3). Figure 4-2.1 shows the molecular structures and molecular coordinates of both KHM and malonyl radicals. (a) A KHM radical is a homo-nuclear system and (b) a malonyl radical is a hetero-nuclear system. The spin Hamiltonian of

each system is employed from the past studies with single-crystal experiments.

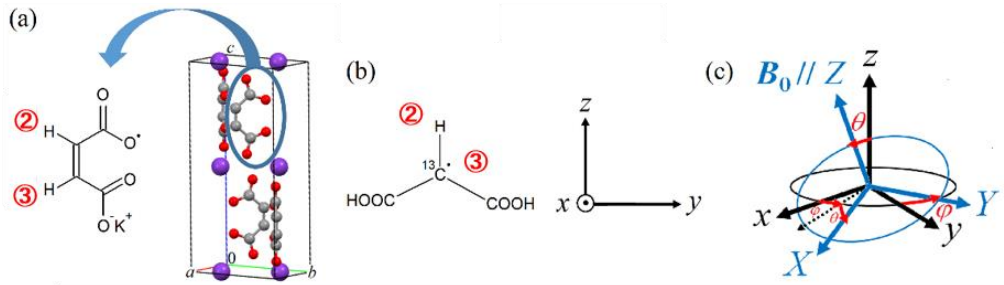

Figure 4-2.1 Molecular structures and *XYZ* coordinate. (a) A molecular structure of a potassium hydrogen maleate (KHM) radical. The molecular coordinate *xyz* is same as a crystallographic coordinate *abc*. The 1st qubit is an electron spin and the 2nd and 3rd qubits are hydrogen (^{1}H2, ^{1}H3) atoms depicted in the figure. (b) A molecular structure of a ^{13}C- labeled malonyl radical. The 1st qubit is an electron spin and the 2nd and 3rd qubits are hydrogen (α-proton) and ^{13}C atoms (^{1}H2, ^{13}C3) depicted in the figure, respectively. The coordinate (*xyz*) is the principal axes of the hyperfine tensor of α-proton. (c) Definition of *XYZ* computational coordinate with respect to *xyz* coordinate. Euler angles φ and θ are defined in the figure. The static magnetic field (B_0) is applied parallel to the *Z* axis.

In the orthorhombic KHM radical, the hyperfine tensors in a crystallographic coordinate system *abc* (= the Cartesian molecular coordinate system (*xyz*)) are given by Eqs. (4-2.4a) and (4-2.4b), where electron, ^{1}H2 and ^{1}H3 spins are numbered as 1st, 2nd and 3rd qubit, respectively. In the malonyl radical, hyperfine tensors with respect to molecular coordinate (*xyz*) are given by Eqs. (4-2.5a) and (4-2.5b), and the coordinate axes (*xyz*) are set to the principal axes of hyperfine tensor of α-proton as shown in Fig. 4-2.1b. In the malonyl radical, I utilized electron, ^{1}H2 and ^{13}C3 spins as qubits numbered 1st, 2nd and 3rd, respectively.

In the orientation study, the static magnetic field (B_0) is applied from the *Z*-direction, in which Fig. 4-2.1c shows Cartesian coordinate (*XYZ*) with respect to the molecular coordinate (*xyz*) depicted in Figs. 4-2.1a and 4-2.1b.

$$\boldsymbol{A}_{\mathrm{KHM}}(^1\mathrm{H2}) = \begin{pmatrix} -14.6 & -3.7 & 7.4 \\ -3.7 & -16.0 & -6.3 \\ 7.4 & -6.3 & -23.0 \end{pmatrix} /\mathrm{MHz} \qquad (4\text{-}2.4a)$$

$$\boldsymbol{A}_{\mathrm{KHM}}(^1\mathrm{H3}) = \begin{pmatrix} -14.6 & -3.7 & -7.4 \\ -3.7 & -16.0 & 6.3 \\ -7.4 & 6.3 & -23.0 \end{pmatrix} /\mathrm{MHz} \qquad (4\text{-}2.4b)$$

$$\boldsymbol{A}_{\mathrm{mal}}(^{1}\mathrm{H2}) = \begin{pmatrix} -56.0 & 0.0 & 0.0 \\ 0.0 & -91.5 & 0.0 \\ 0.0 & 0.0 & -26.6 \end{pmatrix} /\mathrm{MHz} \quad \text{(4-2.5a)}$$

$$\boldsymbol{A}_{\mathrm{mal}}(^{13}\mathrm{C3}) = \begin{pmatrix} 211.8 & 1.0 & -8.9 \\ 1.0 & 24.6 & -1.3 \\ -8.9 & -1.3 & 43.4 \end{pmatrix} /\mathrm{MHz} \quad \text{(4-2.5b)}$$

4-2-3. Controllability

Complete controllability of one electron and multi-nuclear spin-1/2 systems with microwave is established by a closed Lie group SU(2^{1+Nd}) in the earlier study[13] which is simulated by GRAPE algorithm with SAA spin Hamiltonian and experimented with an X-ray irradiated malonyl radical (one electron and one hydrogen nuclear system). Where N_d denotes the nuclear number of qubits. Assuming non-equivalent nuclear spins at the proof, the graph connectivity[17] of quantum states is considered in order to make transitions between the states, and then the controllability of the system is ensured excepting no off-diagonal elements in hyperfine tensors. This is because in one electron and two nuclei spin systems, the nuclear spins are applied spin rotations around (*x*-/*y*- axes) only via hyperfine interactions as described in spin Hamiltonian at subsection 4-2-1, i.e. off-diagonal elements of hyperfine interactions ($A_{zx}I_x$ and $A_{zy}I_y$) are essential to flip nuclear spins. This implies that the hyperfine interactions are significant role also in control difficulty.

4-2-4. GRAPE Algorithm

Numerical simulations with GRAPE algorithm are performed by DYNAMO toolbox[18] on MATLAB software. The algorithm optimizes control amplitude $u(t)$ with fixed frequency pulses targeting quantum states and gates. In the optimization process, a GRAPE method calculates gradient of fidelity (f) against the control amplitude ($\partial f/\partial u$), and the extremum is searched in order to maximize fidelity. Fidelity represents 'a distance' between two matrices, which ranges 0 to 1 and large fidelity indicates two matrices are well resembled (see subsection 3-6-1 in chapter 3). In the standard QC study, fidelity suggests computational accuracy ($f = 1$ is complete accuracy of control and $f = 0$ is completely wrong control). Broyden-Fletcher-Goldfarb-Shanno (BFGS) scheme is adopted for the optimization algorithm.

4-3. Simulation Conditions

Simulations with microwave GRAPE pulses are invoked in *XYZ* coordinate and the parameters were described in subsection 4-2-2. Toward universal control, off-diagonal elements of hyperfine tensors in *XYZ* coordinate system are required the restrictions as described in subsection 4-2-3. In each molecule, fidelity is a function of two sets of conditions, i.e. GRAPE conditions (target gates, computational time steps and gate operation time) and spin Hamiltonian conditions (strength of the static magnetic field (B_0), subtracted frequency between microwave and Zeeman frequency).

Table 4-3.1. Reference conditions of simulations.

Static magnetic field strength (B_0)	1.1 T
Offset frequency ($(\omega_0 - \omega_{MW})/2\pi$)	10 MHz
Computational time step (Δt)	5 ns
Gate operation time (the KHM radical)	0.5 μs
Gate operation time (the malonyl radical)	0.3 μs

In the molecular orientation study, we fixed several physical parameters to the reference conditions (Table 4-3.1) excepting target gates and molecular orientations. Computational time steps is fixed for 5 ns due to the experimental and SAA points of view. B_0 is set 1.1 T for Q-band ESR experiments. The gate operation time is selected as 0.5 μs and 0.3 μs for the KHM radical and ^{13}C labeled malonyl radical, respectively, where fidelity is estimated to increase monotonically against the gate operation time due to the selectable number of pulse operations. Offset frequency of MW is selected as 10 MHz in order to enhance fidelity (Fig. 4-3.1).

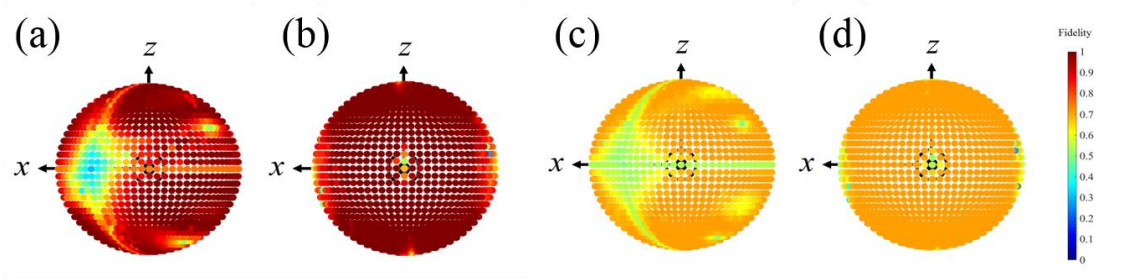

Figure 4-3.1. Offset frequency with fidelity. The static magnetic field is applied from the original points to each plots. (a) A fidelity plots of the KHM radical with offset frequency 10 MHz. (b) A fidelity plots of the malonyl radical with offset frequency 10 MHz. (c) A fidelity plots of the KHM radical with offset frequency 0 MHz. (d) A fidelity plots of the malonyl radical with offset frequency 0 MHz.

Three quantum gates (CNOT1, CNOT2, and SWAP1) are simulated in order to estimate control difficulty of molecular orientations, which unitary matrices are written by Eqs. (4-3.1), (4-3.2) and (4-3.3), respectively. CNOT1 (or CNOT2) flips the 3rd (or 2nd) qubit depending on the state of the 2nd (or 3rd) qubit and SWAP1 exchanges the quantum state of the 2nd qubit with that of the 3rd qubit.

$$\mathrm{CNOT1} = \begin{pmatrix} 1 & 0 & 0 & 0 & 0 & 0 & 0 & 0 \\ 0 & 1 & 0 & 0 & 0 & 0 & 0 & 0 \\ 0 & 0 & 0 & 1 & 0 & 0 & 0 & 0 \\ 0 & 0 & 1 & 0 & 0 & 0 & 0 & 0 \\ 0 & 0 & 0 & 0 & 1 & 0 & 0 & 0 \\ 0 & 0 & 0 & 0 & 0 & 1 & 0 & 0 \\ 0 & 0 & 0 & 0 & 0 & 0 & 0 & 1 \\ 0 & 0 & 0 & 0 & 0 & 0 & 1 & 0 \end{pmatrix} \tag{4-3.1}$$

$$\mathrm{CNOT2} = \begin{pmatrix} 1 & 0 & 0 & 0 & 0 & 0 & 0 & 0 \\ 0 & 0 & 0 & 1 & 0 & 0 & 0 & 0 \\ 0 & 0 & 1 & 0 & 0 & 0 & 0 & 0 \\ 0 & 1 & 0 & 0 & 0 & 0 & 0 & 0 \\ 0 & 0 & 0 & 0 & 1 & 0 & 0 & 0 \\ 0 & 0 & 0 & 0 & 0 & 0 & 0 & 1 \\ 0 & 0 & 0 & 0 & 0 & 0 & 1 & 0 \\ 0 & 0 & 0 & 0 & 0 & 1 & 0 & 0 \end{pmatrix} \tag{4-3.2}$$

$$\mathrm{SWAP1} = \begin{pmatrix} 1 & 0 & 0 & 0 & 0 & 0 & 0 & 0 \\ 0 & 0 & 1 & 0 & 0 & 0 & 0 & 0 \\ 0 & 1 & 0 & 0 & 0 & 0 & 0 & 0 \\ 0 & 0 & 0 & 1 & 0 & 0 & 0 & 0 \\ 0 & 0 & 0 & 0 & 1 & 0 & 0 & 0 \\ 0 & 0 & 0 & 0 & 0 & 0 & 1 & 0 \\ 0 & 0 & 0 & 0 & 0 & 1 & 0 & 0 \\ 0 & 0 & 0 & 0 & 0 & 0 & 0 & 1 \end{pmatrix} \tag{4-3.3}$$

4-4. Results and Discussions of Molecular Orientations

Fidelity of each quantum gate is simulated with the molecular orientations (φ, θ) corresponding to the static magnetic field B_0 (φ, θ) direction. Orientation plots of fidelity is simulated with intervals of 5 degrees, where Fig. 4-4.1 (a), (b) and (c) are for the KHM radical and Fig. 4-4.2 (a), (b) and (c) for the malonyl radical are the orientation plots of CNOT1, CNOT2 and SWAP1, respectively. In section 4-4, the other parameters were set to the reference conditions and spin Hamiltonian parameters, especially hyperfine tensors, are discussed in *XYZ* coordinate because of B_0 (φ, θ) // *Z*.

In the orientation study, fidelity reflects controllability and control difficulty. Control difficulty is low if fidelity is high, vice versa, the system is hard or impossible to be controlled if fidelity is low, i.e. unsuitable conditions to control. Here, I discuss two physical aspects of low fidelity orientations (φ, θ) (see subsection (4-4-1 and 4-4-2) and (4-4-3 and 4-4-4)), which can quantitatively establish the fidelity plots.

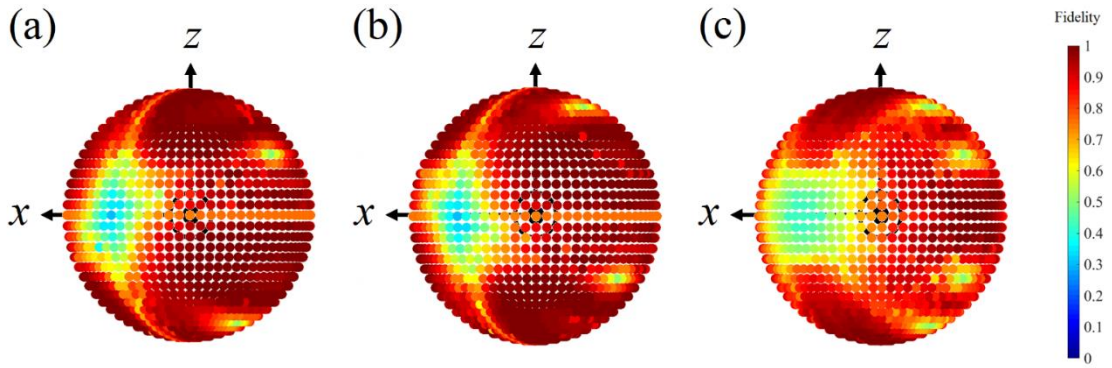

Figure 4-4.1. Fidelity plots with respect to orientations of static magnetic field in the KHM radical. Each sphere indicates each two qubit gate manipulating two hydrogen nuclear qubits. The direction of static magnetic field is applied from the original points to the plotted point and the color shows fidelity. (a) CNOT1 gate. (b) CNOT2 gate. (c) SWAP1 gate.

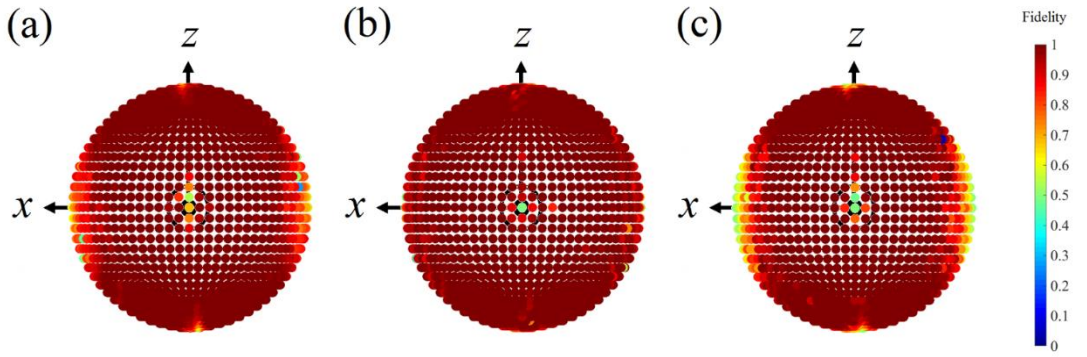

Figure 4-4.2. Fidelity plots with respect to orientations of static magnetic field in the malonyl radical. Each sphere indicates each two qubit gate manipulating two hydrogen and ^{13}C nuclear qubits. The direction of static magnetic field is applied from the original points to the plotted point and the color shows fidelity. (a) CNOT1 gate. (b) CNOT2 gate. (c) SWAP1 gate.

4-4-1. Controllability and Distinguishability

Distinguishability of qubits is a key to QCs. If two qubits (spin-1/2) cannot be controlled individually, the system is no longer able to be manipulated as two qubits (spin-1/2), and then the system behaves one qubit (spin-1). As a result, the spin degree of freedom is decreased from 2^2 (two spin-1/2 qubits) to 3^1 (one spin-1 qubit), and then controllability of 4 states disappears in the latter case. Thus, it is essential to distinguish qubits to acquire controllability. Since individual quantum operations are supposed by non-symmetric operations, symmetric control and molecular Hamiltonian between two spins lead the spins impossible to distinguish.

In the case of indirect control of nuclear spins via microwave, symmetrical molecular Hamiltonian makes hard to distinguish nuclear qubits due to the symmetry of control Hamiltonian of any nuclei (see Eqs. (4-2.2) and (4-2.3)). Therefore, the non-symmetric nuclear Zeeman and hyperfine interaction terms are the key to acquire nuclear spin distinguishability.

4-4-2. First Unsuitable Orientations: Lack of Distinguishability

The ^{13}C-labeled malonyl radical has distinguishability of two nuclear qubits due to the heteronuclear feature different from the homonuclear system of the KHM radical. Thus, heteronuclear spins are always possible to be distinguished with each other. For CNOT1 and CNOT2 gates with the KHM radical, fidelity is low suggesting high control difficulty in two arcs which orientations of (φ = 50°, θ = arbitrary) and orientations of (φ = arbitrary, θ = 90°) are depicted in Fig. 4-4.3 (a) and (b) (see also Fig. 4-4.1 (a) and (b)). Table 4-4.1 shows the hyperfine tensors in several orientations. It is clear that the absolute values of tensors are same at ^{1}H2 and ^{1}H3 in low fidelity orientations, thus these arcs are

given rise to the lack of distinguishability of the two nuclear qubits. Furthermore, the arc feature is originated of symmetry of the hyperfine tensors since absolute principal values of two hyperfine tensors are same as described in Eqs. (4-2.4).

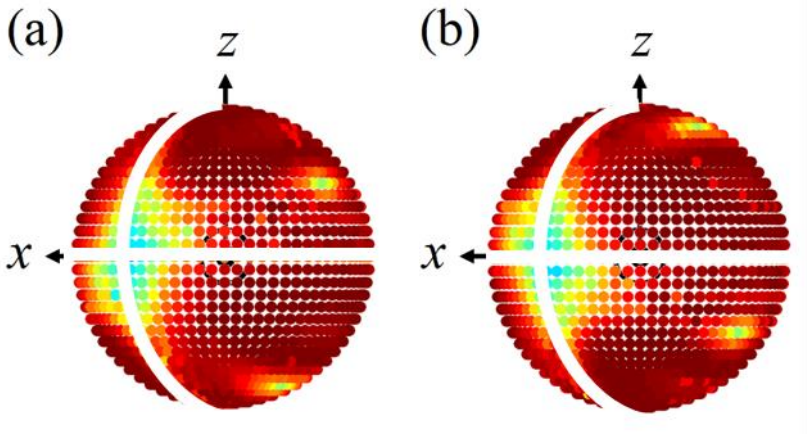

Figure 4-4.3. Fidelity plots with respect to orientations of static magnetic field in the KHM radical. The direction of static magnetic field is applied from the original points to the plotted point and the color shows fidelity. White two lines shows low fidelity conditions of two arcs which orientations are (φ = 50°, θ = arbitrary) and (φ = arbitrary, θ = 90°) (a) CNOT1 gate. (b) CNOT2 gate.

Referring gate dependence, there are still performable operations for nuclear spins even in lack of distinguishability, i.e. in lack of controllability. SWAP1 gate which does not require to distinguish two qubits has no low fidelity arcs of φ = 50° and θ = 90° at the KHM radical in contrast to the CNOT gate simulations. This is because SWAP gates exchange quantum states of two qubits and then the gates are symmetrically in the acting two qubits (see Eq. (4-3.3)). Note that the molecular orientations without distinguishability/controllability are impossible to implement UQG, therefore these are unsuitable orientations for quantum computing.

Table 4-4.1. Tensor conditions and distinguishability. Table shows orientations, hyperfine tensors and fidelity in the KHM radical of CNOT1. Excepting the reference orientation (φ = 10° and θ = 150°), fidelity is lower than 0.8 due to the lack of distinguishability. Control and Target qubits are the 2nd and 3rd qubits of hydrogen atoms.

Orientations		Qubits	Hyperfine tensor parameters			Fidelity
φ /°	θ /°		A_{ZX}/MHz	A_{ZY}/MHz	A_{ZZ}/MHz	
50	30	Control	1.7	-8.4	-22.1	≈ 0.75
		Target	1.7	8.4	-22.0	
50	90	Control	0.0	-0.1	-19.0	≈ 0.30
		Target	-0.0	-0.1	-19.0	
140	90	Control	9.7	0.1	-11.5	≈ 0.75
		Target	-9.7	0.1	-11.5	
10	150	Control	0.0	4.6	-26.6	0.99
		Target	-6.2	-8.3	-15.9	

4-4-3. Controllability and Interaction Strength.

The second conditions related to controllability are orientations with small interaction strength. As described in subsection 4-2-3, the controllability disappears if the system does not have off-diagonal elements of hyperfine tensors.[13] Here, I discuss the computational speed based on interaction strength. Assume a simple one electron and one nucleus (I = 1/2) system in which Hamiltonian is written by only one off-diagonal hyperfine interaction between an electron and a nucleus.

$$H = 2\pi A_{ZX} S_Z I_X \tag{4-4.1}$$

Then it takes time to flip the nuclear spin at least,

$$e^{-iHT} = -i\sigma_Z^e \sigma_X^n \;\Rightarrow\; T_{\min} = \frac{1}{A_{ZX}} \tag{4-4.2}$$

where T is computational time, σ_Z^e is Pauli matrix of Z direction for the electron and σ_X^n is Pauli matrix of X direction for the nucleus. The details of unit are described in introduction of chapter 3, and $\hbar$ is set to 1. When the coupling constant $A_{ZX} = 1$ MHz, the minimum computational time $T_{\min} =$ 1 μs. Since nuclear spin rotations in my systems depend on the off-diagonal elements of hyperfine interactions, the strength ($A_{\text{off}} = \sqrt{|A_{ZX}|^2 + |A_{ZX}|^2} \geq 2.0$ and 3.3 MHz) are essential to flip nuclear spins with 0.5 μs for the KHM radical and 0.3μs for the malonyl radical, respectively. In general, the strong off-diagonal elements, i.e. strong anisotropy of hyperfine tensors, are suitable for fast quantum computations.

4-4-4. Second Unsuitable Orientations: Lack of Interaction Strength.

The other aspect of control difficulty is governed by the interaction strength. In the KHM radical, fidelity of CNOT1 (see Fig. 4-4.1 (a) and Fig. 4-4.4) becomes low at the orientations (φ, θ) of (140°, 60°), (140°, 150°), and (50°, 90°) and the hyperfine parameters are shown in Table 4-4.2. It is obvious that the off-diagonal elements of the hyperfine tensor (A_{ZX} and A_{ZY}) of the nucleus ^{1}H3 are too small to flip the nuclear spin in the low fidelity orientations as discussed in section 4-4-3, i.e. the static magnetic field is applied from the principal axis of the hyperfine tensor of ^{1}H3.

However, the orientations of (140°, 30°) and (140°, 120°) with small off-diagonal hyperfine elements of ^{1}H2 have still high fidelity in CNOT1. Taking into account of the character of CNOT1, the nuclear spin ^{1}H2 does not require any spin rotations since ^{1}H2 is control qubit in contrast to the target qubit ^{1}H3. These results suggest that the required time and spin interactions depend on the quantum gates in numerical pulses.

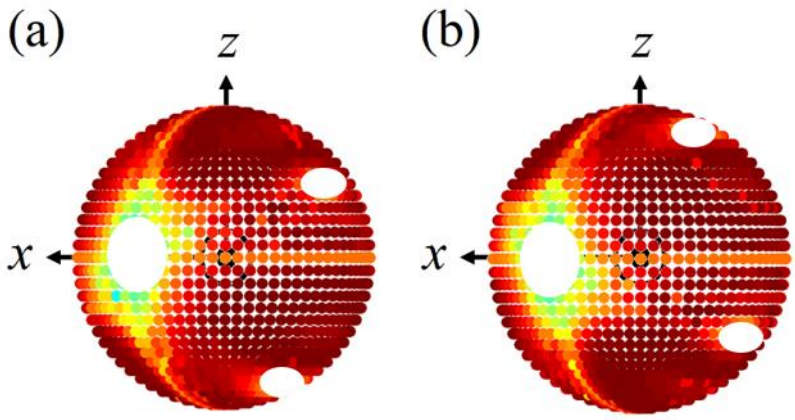

Figure 4-4.4. Fidelity plots with respect to orientations of static magnetic field in the KHM radical. The direction of static magnetic field is applied from the original points to the plotted point and the color shows fidelity. Five white circles shows low fidelity conditions of (140°, 30°), (140°, 60°), (140°, 120°), (140°, 150°), and (50°, 90°) depicted in Table 4-4.2. (a) CNOT1 gate. (b) CNOT2 gate.

Table 4-4.2. Tensor conditions and interaction strength. Table shows orientations, hyperfine tensors and fidelity in the KHM radical of CNOT1. Excepting the reference orientation (φ = 10° and θ = 150°), fidelity is lower than 0.8 due to the lack of distinguishability. Control and Target qubits are the 2nd and 3rd qubits of hydrogen (^{1}H2 and ^{1}H3) atoms.

Orientations		Qubits	Hyperfine tensor parameters			Fidelity
φ /°	θ /°		A_{ZX}/MHz	A_{ZY}/MHz	A_{ZZ}/MHz	
140	30	Control	0.1	0.1	-28.5	0.99
		Target	9.8	0	-11.7	
140	60	Control	9.8	0.1	-22.8	≈ 0.50
		Target	0.1	0.0	-6.0	
140	120	Control	-0.1	0.0	-6.0	0.99
		Target	-9.8	0.1	-22.8	
140	150	Control	-9.8	0	-11.7	≈ 0.50
		Target	-0.1	0.1	-28.5	
50	90	Control	0.0	-0.1	-19.0	≈ 0.30
		Target	-0.0	-0.1	-19.0	

Further evidence has been found in the orientation study of CNOT2 and SWAP1 (see Fig. 4-4.1 (b) and (c)). In CNOT2 (Fig. 4-4.4 (b)), low fidelity orientations are changed into (140°, 30°) and (140°, 120°), which are principal axes of the hyperfine tensor of ^{1}H2, from (140°, 60°) and (140°, 150°). The molecular orientations around (50°, 90°) still have low fidelity in CNOT2 since the orientation of (50°, 90°) has coaxial property in the hyperfine principal axes of ^{1}H2 and ^{1}H3. In the case of SWAP1, fidelity decreases both orientations at the principal axes of hyperfine tensors of ^{1}H2 and ^{1}H3 (see the orientations of (140°, 60°), (140°, 150°), (140°, 30°), (140°, 120°) and (50°, 90°)). The unsuitable orientations in SWAP1 are matched with connectivity as described in 4-2-3. As a result, all the dominant orientations with low fidelity depicted in the fidelity plots are characterized in the KHM radical, which make UQG hard or impossible.

This mechanism of the small interaction strength also appears in the malonyl radical as depicted in Fig. 4-4.5 (see also Fig. 4-4.2). Since the malonyl radical has coaxial properties for all principal axes of hyperfine tensors, the low fidelity orientation does not depend on those three gates, in which some nuclear spin rotations are included, and appeared in (0°, 0°), (0°, 90°) and (90°, 90°). Since those are all the low fidelity conditions at the malonyl radical, all the unsuitable orientations are characterized in the malonyl radical too. Thus, the heteronuclear malonyl radical system can decrease the unsuitable orientations based on the heteronuclear character, the coaxial property and large anisotropy of hyperfine tensors.

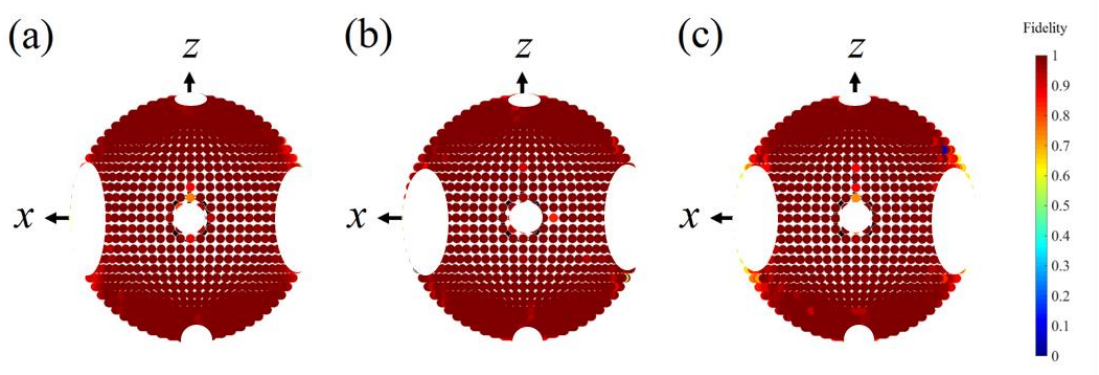

Figure 4-4.5. Fidelity plots with respect to orientations of static magnetic field in the malonyl radical. The direction of static magnetic field is applied from the original points to the plotted point and the color shows fidelity. Five white circles shows low fidelity conditions of (0°, 0°), (0°, 90°) and (90°, 90°). Due to the plotted orientations, (0°, 180°) and (90°, 150°) can also be seen but those are double count by the axial property. (a) CNOT1 gate. (b) CNOT2 gate. (c) SWAP1 gate.

4-4-5. Discussions of Molecular Orientations and Controllability

All the dominant orientations with low fidelity in Figs. 4-4.1 and 4-4.2 can be established from the view point of (1) distinguishability of qubits and (2) interaction strength. They are interpreted by controllability, and the orientations difficult to control are appeared around the orientations with lack of controllability. Each orientation is related with spin Hamiltonian of molecules directly, i.e. (1) principal values of each hyperfine tensor in homo-nuclear system and (2) the off-diagonal strength of the hyperfine tensors. From the view point of experiments, the static magnetic field should be applied with the distant direction far from those unsuitable orientations. It is because the orientations with high fidelity are predicted by complement groups of the unsuitable orientations depicted as Figs. 4-4.1 and 4-4.2.

Furthermore, it has proven that molecular designs are possible from quantum chemical/mechanical points of view even for numerical simulated pulses. Since there are the unsuitable orientations (1) and (2), to reduce these orientations is possible by molecular design. As a result, molecules should be designed as follows: (i) hetero-nuclei system or non-symmetric hyperfine principal values between nuclei, (ii) large anisotropy for hyperfine tensors and (iii) coaxial properties for hyperfine tensors.

4-5. Simulations of Time Evolution.

Time evolution of the one electron and two nuclear system is confirmed by numerical simulations. In the KHM radical, a GRAPE pulse of CNOT1 in the orientation (10°, 150°) is shown in Fig. 4-5.1. The computational time 1.2 μs is selected to decrease the control amplitude of the simulated pulse. The other conditions (the static magnetic field, offset frequency and time steps) are set to the reference conditions as discussed in section 4-3. In SAA Hamiltonian, fidelity is estimated at 0.9907.

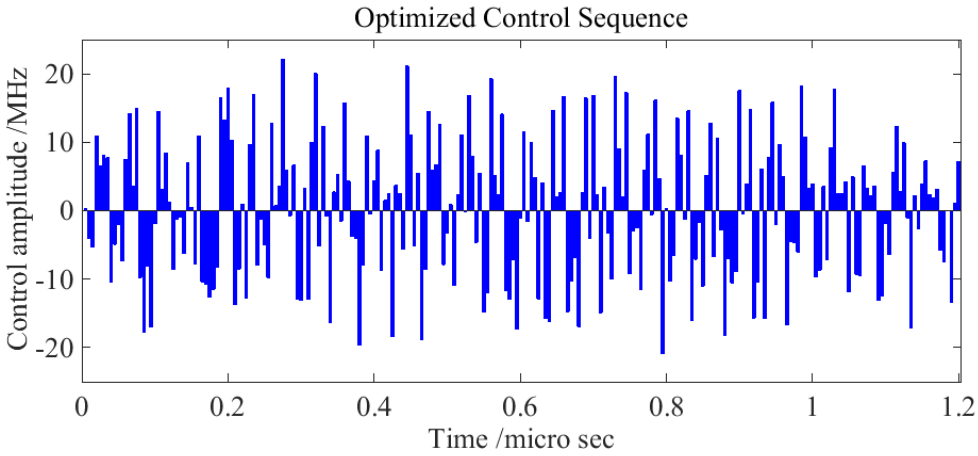

Figure 4-5.1. A GRAPE pulse sequence of the KHM radical in the orientation (10°, 150°).

Further simulations are invoked by assuming spin Hamiltonian without any approximation (SAA). In the simulations, time steps and microwave frequency are set to 0.1 ps and 30.856 GHz, respectively. With the transformation into the rotating frame, fidelity is estimated to 0.5654. However, correcting the phase of electron with Eq. (4-5.1),

$$U_{\text{corrected}} = U_{\text{calc}} \cdot \exp(-i\,\sigma_z \alpha/2)\,, \qquad 0 \le \alpha \le 4\pi \tag{4-5.1}$$

the best fidelity is increased to 0.9897 as depicted in Fig 4-5.2. Where α /rad is a correction coefficient (fitting parameter), U_{calc} is the simulated gate in Schrödinger picture and $U_{\text{corrected}}$ is the corrected gate. As a result, the 2-qubit gate operation succeeds except for the electron phase.

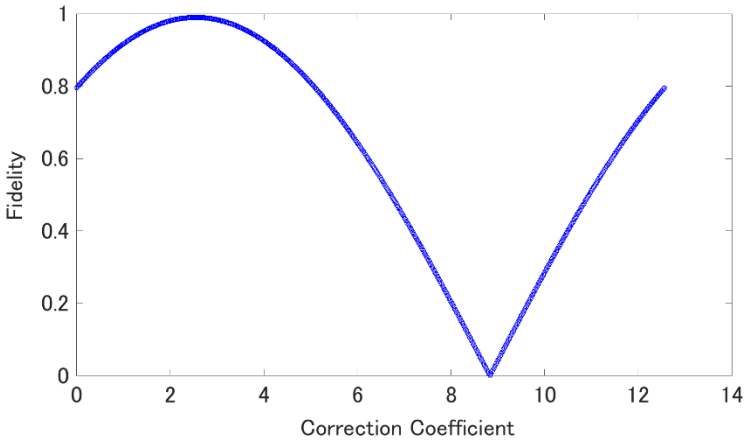

Figure 4-5.2. Fitted fidelity with Eq. (4-5.1). The maximum fidelity is 0.9897 at the correction coefficient = 2.564 /rad.

4-6. Conclusions

In this chapter, molecular orientation studies for the KHM and malonyl radicals with indirect quantum state control by numerical pulses have been invoked to estimate control difficulty for QC experiments and to optimize spin Hamiltonian of molecules. As a result, several molecular orientations which are not suitable to manipulate spins are found and have no distinguishability of qubits and/or small interaction strength of the hyperfine tensors. Since both are interpreted by the controllability of spin systems, the other parameters, e.g. transition rates, transition frequency, etc., are estimated as minor contributions. It is noteworthy that suitable molecular orientations can be predicted directly from the controllability of spin systems. Thus, feasible systems are characterized by (i) hetero-nuclei system or non-symmetric hyperfine principal values between nuclei, (ii) large anisotropy for hyperfine tensors and (iii) coaxial properties for hyperfine tensors.

From the QC/QIP point of view, to find the best orientation to control qubits is one of the significant problem. In this study, I have suggested several candidates for valid quantum control as the distinct orientations from the unsuitable conditions. This guideline must improve the numerical pulse experiments with molecular spin systems.

4-7. References

[1] M. A. Nielsen, I. L. Chuang, *Quantum Computation and Quantum Information*, Cambridge University Press, 2000; Wang, Y., *Statistical Science*, **2012**, *27*, 373.

[2] Y. Morita, Y. Yakiyama, S. Nakazawa, T. Murata, T. Ise, D. Hashizume, D. Shiomi, K. Sato, M. Kitagawa, K. Nakasuji, T. Takui, *J. Am. Chem. Soc*., **2010**, *132*, 6944-6946; H. Atsumi, K. Maekawa, S. Nakazawa, D. Shiomi, K. Sato, M. Kitagawa, T. Takui, K. Nakatani, *Chem. Eur. J*., **2012**, *18*, 178-183; H. Atsumi, S. Nakazawa, C. Dohno, K. Sato, T. Takui, K. Nakatani, *Chem. Commun*., **2013**, *49*, 6370-6372.

[3] S. Nakazawa, S. Nishida, T. Ise, T. Yoshino, N. Mori, R. Rahimi, K. Sato, Y. Morita, K. Toyota, D. Shiomi, M. Kitagawa, H. Hara, P. Carl, P. Höfer, T. Takui, *Angew. Chem. Int. Ed.*, **2012**, *51*, 9860-9864.

[4] T. Yoshino, S. Nishida, K. Sato, S. Nakazawa, R. D. Rahimi, K. Toyota, D. Shiomi, Y. Morita, M. Kitagawa, T. Takui, *J. Phys. Chem. Lett*., **2011**, *2*, 449–453.

[5] V. Ramakrishna, M. V. Salapaka, M. Dahleh, H. Rabitz, A. Peirce, *Phys. Rev. A*, **1995**, *51*, 960; S. G. Schirmer, H. Fu, A. I. Solomon, *Phys. Rev. A*, **2001**, *63*, 063410.

[6] V. F. Krotov, I. N. Feldman, *Eng. Cybern*., **1983**, *21*, 123; V. F. Krotov, I. N. Feldman, *Izv. Akad. Nauk. SSSR Tekh Kibern.* **1983**, *52*, 162-167. A. I. Konnov, V. F. Krotov, *Autom. Remote Control*, **1999**, *60*, 1427; J. P. Palao, R. Kosloff, *Phys. Rev. Lett*., **2002**, *89*, 188301. J. P. Palao, R. Kosloff, *Phys. Rev. A*, **2003**, *68*, 062308.

[7] M. S. Vinding, C. Laustsen, M. S. Vinding, L. V. Sogaard, J. H. Ardenkjaer-Larsen, N. C. Nielsen, *J. Magn. Reson*., **2013**, *227*, 57-61.

[8] M. S. Vinding, I. I. Maximov, Z. Tosner, N. C. Nielsen, J. Chem. Phys., 2012, 137, 054203.

[9] L. Hong-Sheng, T. Jia-Xin, Z. Shu-Na, W. Da-Xiu, *Acta. Physica. Sinica*, **2015**, *64*, 170301.

[10] N. Khaneja, T. Reiss, C. Kehlet, T. Schulte-Herbrüggen, and S. J. Glaser, *J. Magn. Reson*., **2005**, *172*. 296-305.

[11] Z. Wu, J. Li, W. Zheng, J. Luo, M. Feng, and X. Peng, *Phys. Rev. A*, **2011**, *84*, 042312.

[12] N. Xu, J. Zhu, D. Lu, X. Zhou, X. Peng, J. Du, *Phys. Rev. Lett*., **2012**, *108*, 130501.

[13] J. S. Hodges, J. C. Yang, C. Ramanathan, D. G. Cory, *Phys. Rev. A*, **2008**, *78*, 010303.

[14] *OBJECT-ORIENTED MAGNETIC RESONANCE; Classes and Objects, Calculations and Computations*, eds. M. Mehring and V. A. Weberruss, ACADEMIC PRESS, San Diego, **2001**.

[15] H. C. Heller, T. Cole, *J. Am. Chem. Soc*., **1962**, *84*, 4448-4451.

[16] D. K. Park, G. Feng, R. Rahimi, S. Labruyère, T. Shibata, S. Nakazawa, K. Sato, T. Takui, R. Laflamme, J. Baugh, *Quantum Inf. Process*., **2015**, *14*, 2435-2461.

[17] C. Altafini, J. *Math. Phys*., **2002**, *43*, 2051; G. Turinici, H. Rabitz, *Chem. Phys*., **2001**, *267*, 1.

[18] S. Machnes, U. Sander, S. J. Glaser, P. de Fouquières, A. Gruslys, S. Schirmer, T. Schulte-Herbrüggen, *Phys. Rev. A*, **2011**, ***84***, 022305.

Chapter 5

Quantum Algorithm of Configuration State Function (CSF) toward Quantum Chemical Calculations on Quantum Computers (QCCs on QCs)

5-1. Introduction

One of the ultimate goals of theoretical chemistry and physics is to conquer the exact solution of Schrödinger equation which governs stochastic and dynamical motions of atoms and molecules. The Schrödinger equation has been solved under various physical situations since quantum mechanics have born, and there are always challenging problem sizes to solve despite the development of computer technology. In quantum chemistry, although Hamiltonian of systems is defined rigorously,[1] in numerical calculation an astronomical number of operations must be performed for acquiring accurate solutions due to the two-body nature of interactions among electrons.

The best solution of the Schrödinger equation within a given basis set is referred to as the full configuration interaction (FCI) wavefunction. The computational costs for solving the FCI problem depends on the number of electrons in the atomic/molecular systems and the size of basis set. Great efforts have been made to develop theoretical frameworks as well as computational programs to obtain as accurate total energy and wavefunctions as possible of larger molecular systems with less computational costs. For example, the density matrix renormalization group (DMRG) is able to compute complete active space configuration interaction (CAS-CI) type wavefunctions for large active space up to 40 electrons and 40 orbitals.[2] The exact wavefunctions (beyond FCI limit) of small molecules can be calculated with supercomputers, by adopting the free complement theory proposed by Nakatsuji and co-workers.[3] The series of reports made a paradigm shift on the role of quantum chemistry to the truly predictive tool in chemical science, but their applications are still limited at the moment.

QCCs on QCs are based on the one suggestion by Feynman in 1982 that quantum systems can be efficiently simulated by using quantum devices by Feynman.[4] The first theoretical suggestion and application for QCCs on QCs were demonstrated in 2005 by Aspuru-Guzik and co-workers.[5] It was computation of FCI energies of molecules with quantum computing and quantum phase estimation (QPE) algorithm of Abrams and Lloyd (Eq. (5-1.1)).[6]

$$e^{-(iHt/\eta)}\left|\Psi\right\rangle = e^{-(iEt/\eta)}\left|\Psi\right\rangle = e^{-i2\pi\phi}\left|\Psi\right\rangle \qquad (5\text{-}1.1)$$

Experiments for QCCs on QCs have been reported since 2010, where FCI/STO-3G calculations of H_2 molecule are invoked in the photonic[7] and NMR-[8] QCs. Although this is a new research field even among quantum computing science, quantum FCI is now considered as near-future targets to realize.[9] However, the fundamental quantum algorithms are still limited against the vast research filed of quantum chemistry. Therefore new quantum algorithms, i.e. superpolynomial algorithms which can be run in polynomial time not with classical computers but with QCs, are still desired in order to perform efficient QCCs. It is noteworthy that quantum FCI based on QPE does not require the preparation of exact wavefunction (Ψ_{Exact}) but approximated wavefunction (Ψ_0).[5] Although the difference in the wavefunctions affects success probability of the algorithms proportional to

$|<\Psi_0|\Psi_{Exact}>|^2$, QPE is still available to calculate the FCI energy in the case of $|<\Psi_0|\Psi_{Exact}>|^2 > 0.5$.[5]

As describing the feature of quantum FCI, preparation of wavefunction is a still modifiable problem. In closed-shell molecules, a Hartree–Fock wavefunction Ψ_{HF} is a choice for Ψ_0 because a single determinant of orbitals is typically an good approximation of a ground state.[10] Needless to say, this approach is not valid for open-shell systems. In general, Ψ_{Exact} can have a strong multiconfigurational character resulting in a small overlap with Ψ_{HF}. It is known that a wavefunction of the open-shell molecule with antiferromagnetic interactions among electrons is composed of many Slater determinants due to a requirement satisfying the spin symmetry of operator $\boldsymbol{S}^2$ and S_z.[10] If the system has this multiconfigulational character, Ψ_{HF} is no longer a good approximation of Ψ_{Exact}. Thus an approximate wavefunction is desired to be properly prepared on the basis of spin nature.

Here, I introduce a new quantum algorithm to construct spin symmetry-adapted configuration state function (CSF). The CSF (Ψ_{CSF}) is considered to ensure a sufficiently larger overlap of Ψ_{CSF} with Ψ_{Exact} than that of Ψ_{HF} with Ψ_{Exact} in open-shell molecules due to symmetry of spin functions. The feature of CSF is discussed in section 5-2 and the algorithm details are shown in section 5-4 and 5-5. This quantum algorithm has a superpolynomial property against singly occupied β spins because it prepares an exponential number of determinants with polynomial time in QCs.

5-2. Effectiveness of CSF in QPE

Potency of CSF in QPE is depicted in the ground state (S = 10) of the first single molecule magnet $[Mn_{12}O_{12}(CH_3COO)_{16}(H_2O)_4]$.[11] The Mn cluster includes eight Mn^{III} (d^4) and four Mn^{IV} (d^3) magnetic centres with antiferromagnetic interactions between adjacent Mn^{III} and Mn^{IV} centres.[25] In this section, I describe the number of Slater determinants. I assume that the Mn cluster has a single CSF type of wavefunction, namely, that a single CSF, a minimum unit satisfying the symmetry of spin eigenfunction, is a better approximation of the exact wavefunction of the Mn clusters than a single Slater determinant. The number of primitive spin functions belonging to M_S = 10 is ${}_N\mathbf{C}_{N\beta}$ = ${}_{44}\mathbf{C}_{12} \approx 2.1 \times 10^{10}$, where N and N_β stand for the total number of unpaired electrons and the number of unpaired spin-βelectrons respectively. The number ${}_N\mathbf{C}_{N\beta}$ can easily diverge to the exponential number. In the QC, the CSF is possible to be prepared only with N_β of one-qubit rotations and N_β^2 of controlled NOT (CNOT) operations (see section 5-5).

Note that I do not mention that anytime a single CSF wavefunction is a proper approximation of the exact wavefunction but that a CSF can provide a better approximation than any single determinant. From the view point of QPE, the overlap between a 'best' single Slater determinant (e.g., Hartree-Fock) and the exact wavefunction is approximately proportional to the inverse of the number of Slater determinants necessary to properly approximate the exact wavefunction. As discussed above, it is clear that if Ψ_0 is a single determinant the success probability of QPE is attenuated exponentially fast against the number of unpaired electrons and the spin quantum number. However, if Ψ_0 is a single CSF, the success probability can be maintained even in this case due to its multi-determinant character.

The second point of this algorithm clarify current direction of QCCs on QCs. Although a CSF itself does not include the effects of electron correlation (i.e., beyond a mean-field approximation), QCs can prepare a better wavefunction easily than classical computers. The algorithm suggests at least that the first approximation toward exact wavefunction is the CSF on QCs. The Hartree-Fock approximation is widely used in ab initio calculations in classical computers, but in QCs the CSF or a better wavefunction than the CSF can take over this situation since the CSF is corresponding to the Hartree-Fock wavefunction for the closed shell molecules. Therefore, QCs can treat the closed shell and open-shell molecules almost equivalently.

5-3. Structure of Spin Eigenfunctions

Here, I describe the spin eigenfunction composing the spin part of the CSF. The same description is written in Pauncz's book.[12] The spin eigenfunction $\Psi_S(N, S, M_S)$ is defined by three parameters: N represents the number of unpaired spins and S, M_S represent eigenvalues of the $\boldsymbol{S}^2$ and $\boldsymbol{S}_Z$ operators, respectively. In the non-relativistic quantum chemistry, one usually focuses on the largest angular momentum sublevel of ($M_S = S$) as electron spin sublevels since the property of ($2S + 1$) sublevels of S with different M_S can be calculated from the reference sublevel by virtue of Wigner-Eckart theorem. Although I describe the spin eigenfunctions in a general fashion at this section, the usual restriction is utilized in the section of the quantum algorithm for the CSF.

The spin eigenfunction is proven by induction as follows. Adding one electron with its spin angular momentum α to the spin eigenfunction $\Psi_S(N, S, M_S)$, Eq. (5-3.1) is obtained due to the properties of the spin quantum number.

$$\Psi_S(N,S,M_S)|\alpha\rangle = C_{S+1/2}\Psi_S(N+1,S+1/2,M_S+1/2)+C_{S-1/2}\Psi_S(N+1,S-1/2,M_S+1/2) \tag{5-3.1}$$

Tow coefficients, $C_{S+1/2}$ and $C_{S-1/2}$, should be calculated with following Lowdin's projection operator $\mathbf{O}_{S+1/2}$ (5-3.4). It is simple in $M_S = S$ that the 2nd term of the right hand side vanishes in Eq. (5-3.1) because M_S value cannot exceed S value.

$$\mathbf{O}_{S+1/2} = \mathbf{S}^2 - \left(S-\frac{1}{2}\right)\left(S+\frac{1}{2}\right)\mathbf{1} \tag{5-3.2}$$

$$\Psi_S(N+1,S+1/2,M_S+1/2) = C\mathbf{O}_{S+1/2}\Psi_S(N,S,M_S)|\alpha\rangle \tag{5-3.3}$$

C denotes the normalization factor and the 2nd term is annihilated by the projection. The $\boldsymbol{S}^2$ operator is as follows:

$$\begin{aligned}\mathbf{S}^2 = {} & \mathbf{S}(1,2,\Lambda\ ,N)^2 + \mathbf{S}(N+1)^2 + \mathbf{S}_-(1,2,\Lambda\ ,N)\mathbf{S}_+(N+1) \\ & + \mathbf{S}_+(1,2,\Lambda\ ,N)\mathbf{S}_-(N+1) + 2\mathbf{S}_Z(1,2,\Lambda\ ,N)\mathbf{S}_Z(N+1)\end{aligned} \tag{5-3.4}$$

where, the operators S_i of (1,2,…,N) refer to the system of N-electrons, and the operators S_i of (N + 1) act to the added one electron. Calculating Eq. (5-3.3), Eq. (5-3.7) is obtained.

$$\Psi_S(N+1,S+1/2,M_S+1/2) = C\left\{\mathbf{S}^2 - \left(S-\frac{1}{2}\right)\left(S+\frac{1}{2}\right)\right\}\Psi_S(N,S,M_S)|\alpha\rangle \tag{5-3.5}$$

$$= C\left\{S(S+1)+\frac{3}{4}+M_S-\left(S^2-\frac{1}{4}\right)\right\}\Psi_S(N,S,M_S)|\alpha\rangle + C\sqrt{(S-M_S)(S+M_S+1)}\Psi_S(N,S,M_S+1)|\beta\rangle \tag{5-3.6}$$

$$= C\left\{(S+M_S+1)\Psi_S(N,S,M_S)|\alpha\rangle + \sqrt{(S+M_S+1)(S-M_S)}\Psi_S(N,S,M_S+1)|\beta\rangle\right\} \tag{5-3.7}$$

Considering a norm of wavefunction at the left side of Eq. (5-3.7), the normalization factor should be taken as Eq. (5-3.8).

$$C = \frac{1}{\sqrt{(S+M_S+1)(2S+1)}} \tag{5-3.8}$$

Thus, an additional equation of angular momentum is obtained.

$$\Psi_S(N+1,S+1/2,M_S+1/2)=\frac{\sqrt{S+M_S+1}\Psi_S(N,S,M_S)|\alpha\rangle+\sqrt{S-M_S}\Psi_S(N,S,M_S+1)|\beta\rangle}{\sqrt{2S+1}} \quad (5\text{-}3.9)$$

In the case of $M_S = S$, Eq. (5-3.9) has a very simple formula.

$$\Psi_S(N+1,S+1/2,S+1/2)=\Psi_S(N,S,S)|\alpha\rangle \quad (5\text{-}3.10)$$

Applying the same methodology, the following three relations are obtained with $\mathbf{O}_{S+1/2}$ and $\mathbf{O}_{S-1/2}$.

$$\Psi_S(N+1,S-1/2,M_S+1/2)=\frac{-\sqrt{S-M_S}\Psi_S(N,S,M_S)|\alpha\rangle+\sqrt{S+M_S+1}\Psi_S(N,S,M_S+1)|\beta\rangle}{\sqrt{2S+1}} \quad (5\text{-}3.11)$$

$$\Psi_S(N+1,S+1/2,M_S-1/2)=\frac{\sqrt{S-M_S+1}\Psi_S(N,S,M_S)|\beta\rangle+\sqrt{S+M_S}\Psi_S(N,S,M_S-1)|\alpha\rangle}{\sqrt{2S+1}} \quad (5\text{-}3.12)$$

$$\Psi_S(N+1,S-1/2,M_S-1/2)=\frac{-\sqrt{S+M_S}\Psi_S(N,S,M_S)|\beta\rangle+\sqrt{S-M_S+1}\Psi_S(N,S,M_S-1)|\alpha\rangle}{\sqrt{2S+1}} \quad (5\text{-}3.13)$$

The spin eigenfunction $\Psi_S(N + 1, S - 1/2, S - 1/2)$ is derived from Eq. (5-3.13). The Eqs. (5-3.9) and (5-3.11) to (5-3.13) suggest that one can add single electron with a spin to the spin system step by step and then the simplest couple of formulas in $M_S = S$ are given in Eqs. (5-3.10) and (5-3.14).

$$\Psi_S(N+1,S-1/2,S-1/2)=\frac{-\sqrt{2S}\Psi_S(N,S,S)|\beta\rangle+\Psi_S(N,S,S-1)|\alpha\rangle}{\sqrt{2S+1}} \quad (5\text{-}3.14)$$

5-4. Quantum Algorithm of Spin Eigenfunction

5-4-1. Algorithmic Scheme of Spin Eigenfunction

In order to establish the quantum algorithm of CSF, the fast preparation of spin eigenfunctions is the key. This is because the spin part of CSF is composed of the spin eigenfunctions as described above. The superpolynomial property is also helped with this part, and the spin eigenfunctions are composed of the superposition of exponential number of the S_z computational basis.

Assume that we have an N-spin system $\Psi_S(N, S, M_S = S)$. As discussed in section 5-3, the wavefunctions satisfy the following equations in the same way as Eqs. (5-3.10) and (5-3.14)

$$\Psi_S(N+1, S+1/2, S+1/2) = \Psi_S(N, S, S)|\alpha\rangle \tag{5-4.1}$$

$$\Psi_S(N+1, S-1/2, S-1/2) = \frac{-\sqrt{2S}\Psi_S(N, S, S)|\beta\rangle + \Psi_S(N, S, S-1)|\alpha\rangle}{\sqrt{2S+1}} \tag{5-4.2}$$

Remember that $\mathbf{S}_-$ operator can create $\Psi_S(k, S, S-1)$:

$$\Psi_S(k, S, S-1) = \frac{1}{\sqrt{2S}}\mathbf{S}_-\Psi_S(k, S, S) \tag{5-4.3}$$

Eq. (5-4.3) suggests that Eqs. (5-4.2) and (5-4.3) can calculated only with the $\Psi_S(N, S, S)$ and S_- operator. In QCs, one can apply unitary operators themselves as quantum operations i.e. as quantum gates therefore those equations can be performed with the direct formulas. However, this suggestion is impossible in classical computers not to have quantum superposition.

It is easy to perform Eq. (5-4.1) on QCs because this operation can be done with just to add single α-spin on the quantum register representing $\Psi_S(N, S, S)$. However, Eq. (5-4.2) should be taken in a different manner preparing Ψ_S1 first:

$$\Psi_S1 = \Psi_S(N, S, S) \otimes \frac{-\sqrt{2S}|\beta\rangle + |\alpha\rangle}{\sqrt{2S+1}} \tag{5-4.4}$$

The second term is prepared by a single qubit rotation. After the preparation of Eq. (5-4.4), the controlled S_- operation is performed by targeting the last α-qubit,

$$\Psi_S(N+1, S-1/2, S-1/2) = \frac{-\sqrt{2S}\Psi_S(N, S, S)|\beta\rangle + \frac{1}{\sqrt{2S}}\mathbf{S}_-\Psi_S(N, S, S)|\alpha\rangle}{\sqrt{2S+1}} \tag{5-4.5}$$

then the same equation as Eq. (5-4.2) is reached. Therefore, the remaining problem is how to apply the controlled S_- operator to $\Psi_S(N, S, S)$ (see section 5-4-2).

5-4-2. Controlled S- Operation

Let me consider the following case: I have wavefunction of $\Psi_S(N, S, S)$, then $\Psi_S(N, S, -S)$ is obtained by spin flip methods.

$$\Psi_S(N, S, S) = |f(\alpha, \beta)\rangle$$
$$<-> \quad \Psi_S(N, S, -S) = |f(\beta, \alpha)\rangle \tag{5-4.6}$$

where $f_N(\alpha, \beta)$ represents the sequence of α, β.

Examples1:

$$\Psi_S(3, 3/2, 3/2) = |f_1(\alpha, \beta)\rangle = |\alpha\alpha\alpha\rangle$$
$$<-> \quad \Psi_S(3, 3/2, -3/2) = |f_1(\beta, \alpha)\rangle = |\beta\beta\beta\rangle \tag{5-4.7}$$

Examples2:

$$\Psi_S(3, 1/2, 1/2) = |f_1(\alpha, \beta)\rangle = 1/\sqrt{6} \times(-2|\alpha\alpha\beta\rangle + |\alpha\beta\alpha\rangle + |\beta\alpha\alpha\rangle)$$
$$<-> \quad \Psi_S(3, 1/2, -1/2) = |f_1(\beta, \alpha)\rangle = 1/\sqrt{6} \times(-2|\beta\beta\alpha\rangle + |\beta\alpha\beta\rangle + |\alpha\beta\beta\rangle) \tag{5-4.8}$$

The simple relation between two spin eigenfunctions suggests that $\Psi_S(N, S, -1/2)$ is obviously calculated with $\Psi_S(N, S, 1/2)$ by spin flip methods. Obviously, Eq. (5-4-2-4) is obtained.

$$\Psi_S(N, 1/2, 1/2) = |f(\alpha, \beta)\rangle$$
$$<-> \quad \Psi_S(N, 1/2, -1/2) = |f(\beta, \alpha)\rangle \tag{5-4.11}$$

Thus, S- operator can be applied to the spin eigenfunction $\Psi_S(N, 1/2, 1/2)$, where automatically S is a half-integer. In quantum algorithm, the gate operation is written in Fig. 5-4.1.

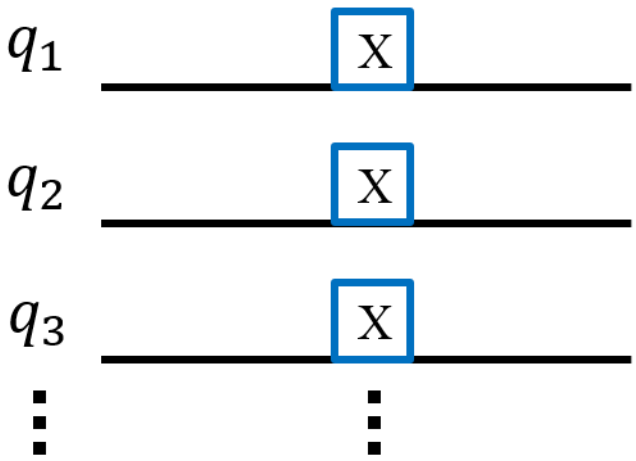

Figure 5-4.1. Quantum algorithm of the S- operator applying to the spin eigenfunction $\Psi_S(N, 1/2, 1/2)$. X is a flip operation of a qubit/qubits representing one spin of $\Psi_S(N, 1/2, 1/2)$.

5-4-3. Pathway of Quantum Computing to Reach Spin Eigenfunctions

In the following quantum algorithm, arbitrary spin eigenfunctions cannot be constructed but all eigenfunctions only for quantum chemical calculations are possible to be computed. It is due to S-operator forms.

First, I introduce a branching diagram (Fig. 5-4.2), in which pathway the spin eigenfunction is calculated. The branching diagram represents couplings of angular momentum and the circles are the set of spin eigenfunctions of $\Psi_S(N, S, S)$. Starting from the origin, the spin eigenfunctions to the final destination are calculated by selecting "sticks" connecting circles from the left to the right as the pathway. The sticks have two selections of up (red) and down (blue). Although each pathway corresponds to a spin eigenfunction one-to-one, any pathways are allowed to compute a set of spin eigenfunctions in quantum chemistry.

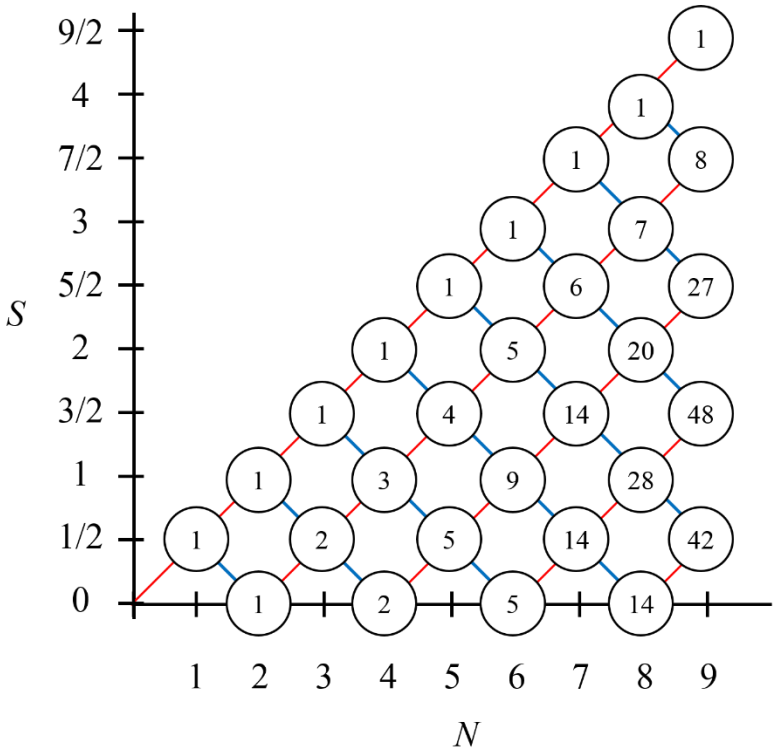

Figure 5-4.2. A branching diagram of the spin eigenfunction. The up (red) and down (blue) lines indicate the pathways to add one unpaired electron from N to $N + 1$. In the up line case, S changes to $S + 1$, and in the down line case, S changes to $S - 1$. The number of circles is the multiplicity of the spin state.

Utilizing two equations in section 5-3 and 5-4-2,

$$\Psi_S(N+1, S+1/2, S+1/2) = \Psi_S(N, S, S)|\alpha\rangle \tag{5-3.10}$$

$$\Psi_S(N, 1/2, 1/2) = |f(\alpha, \beta)\rangle$$
$$<-> \quad \Psi_S(N, 1/2, -1/2) = |f(\beta, \alpha)\rangle \tag{5-4.11}$$

it is possible to achieve spin eigenfunctions on QCs. As described in section 5-4-2, Eq. (5-4.11) suggests that S_- is possible by flipping spins. As a result, the following operations are possible: (1) *if S is 1/2* then use Eq. (5-4.11) to decrease spin number S or use Eq. (5-3.10) to increase S, (2) *otherwise* use Eq. (5-3.10). Thus, there is one pathway leading to $\Psi_S(N, S, S)$ which repeats up $\Psi_S(k + 1, 1/2, 1/2)$ and down $\Psi_S(k + 1, 1/2, -1/2)$ until $k = N - S$ and then repeats up $\Psi_S(k + 1, 1/2, 1/2)$ until $k = N$. The nine pathways leading to $\Psi(6, 1, 1)$ are shown in Fig. 5-4-3.2. The pathway (9) is the one which can be realized by the above quantum operations.

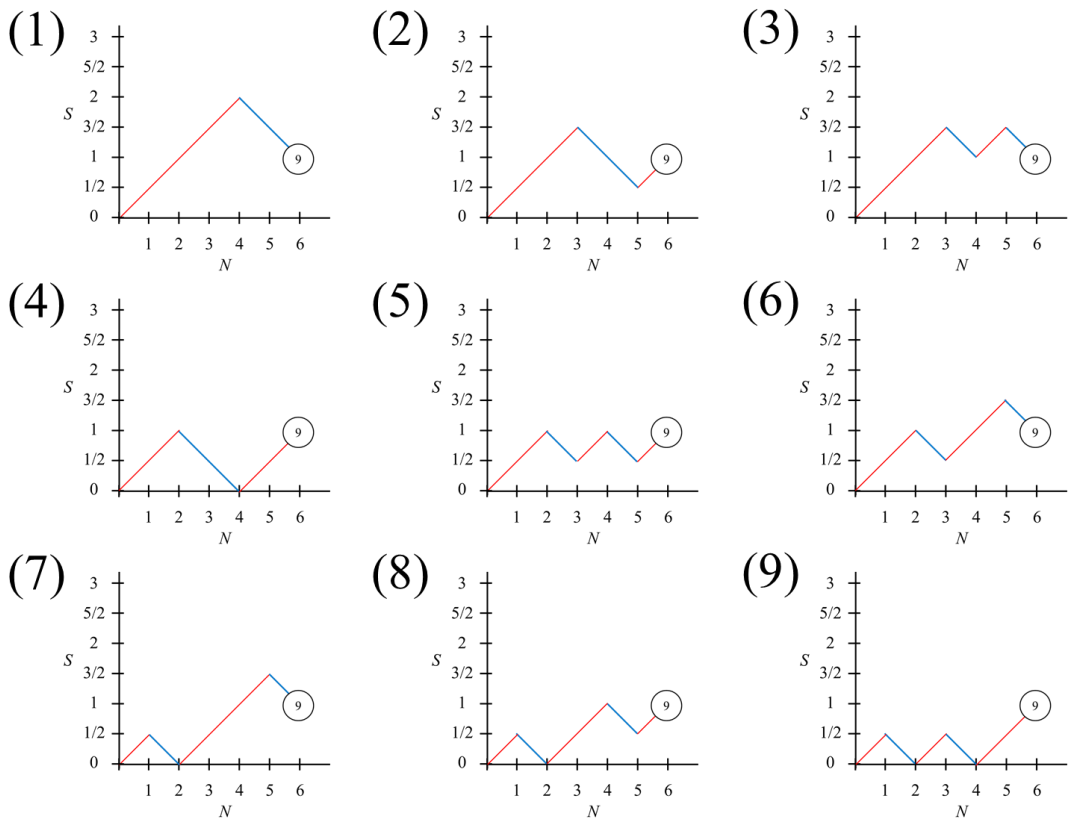

Figure 5-4.3. Pathways in a branching diagram to reach $\Psi(6, 1, 1)$. Pathway (9) is suitable to compute the spin eigenfunction.

5-4-4. Computational Complexity

From the view point of computational complexity, I revisit Eqs. (5-4.1), (5-4.4) and (5-4.5).

$$\Psi_S(N+1,S+1/2,S+1/2)=\Psi_S(N,S,S)|\alpha\rangle \tag{5-4.1}$$

$$\Psi_S 1=\Psi_S(N,S,S)\otimes\frac{-\sqrt{2S}|\beta\rangle+|\alpha\rangle}{\sqrt{2S+1}} \tag{5-4.4}$$

Applying controlled S$_-$ operators to Ψ_S1, I obtain.

$$\Psi_S(N+1,S-1/2,S-1/2)=\frac{-\sqrt{2S}\Psi_S(N,S,S)|\beta\rangle+\frac{1}{\sqrt{2S}}\mathbf{S}_-\Psi_S(N,S,S)|\alpha\rangle}{\sqrt{2S+1}} \tag{5-4.5}$$

Since Eq. (5-4.1) indicates just to add one α spin with no computational costs, the computational complexity is evaluated by Eqs. (5-4.4) and (5-4.5). In S = 1/2, both are transformed into following equations respectively.

$$\Psi_S 1=\Psi_S(N,1/2,1/2)\otimes\frac{-|\beta\rangle+|\alpha\rangle}{\sqrt{2}} \tag{5-4.12}$$

$$\Psi_S(N+1,1/2,-1/2)=\frac{-\Psi_S(N,1/2,1/2)|\beta\rangle+\mathbf{S}_-\Psi_S(N,1/2,1/2)|\alpha\rangle}{\sqrt{2}} \tag{5-4.13}$$

Eq. (5-4.12) suggests that the NOT and Hadamard gates into the β spin are required. The computational cost is N_β. Then, Eq. (5-4.13) achieves the NOT operation into $\Psi_S(N, 1/2, 1/2)$ controlled by the last α qubit with the cost of N_β^2. Therefore, the algorithm preparing exponential number of Slater determinants against N_β just requires N_β times of the NOT and Hadamard gates and N_β^2 times of CNOT gates, which is obviously polynomial number of quantum operations.

5-5. Quantum Algorithm of CSFs

A CSF is described by one spin eigenfunction as discussed in section 5-4 and a set of molecular orbitals. In quantum computing, both spin and orbital information labelling singly occupied orbitals (SOMOs) should be mapped onto quantum registers. Here, I discuss direct mapping (DM)[5] and spin coordinate mapping (SCM).

5-5-1. Map to Qubits (SCM and DM)

Let me assume that the molecule has three components of orbitals: 1) Doubly occupied orbitals, 2) SOMOs and 3) unoccupied orbitals (Fig. 5-5.1). SCM is simple mapping technique of spin and orbital information of SOMOs, in which one SOMO has α-/β- spin then assigns one qubit as |0>/|1>, respectively. There is a state $\Psi_{SCM} = |o_3\alpha, o_4\alpha, o_5\beta, o_6\alpha\rangle_{SCM}$ mapped into the quantum register of SCM: $R_{SCM} = |0010\rangle_{SCM}$, where o_i is the orbital number.

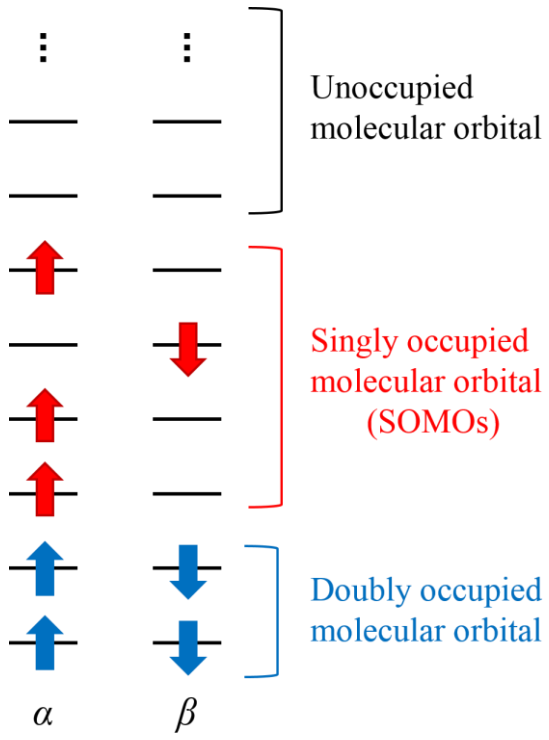

Figure 5-5.1. Schematic view of molecular orbital of open-shell systems. There are three types of molecular orbitals: doubly occupied molecular orbitals, singly occupied molecular orbitals and unoccupied molecular orbitals.

Qubits in DM correspond to ket-vectors in Fock space due to treating creation and annihilation operators. Most quantum algorithms with phase estimation algorithm are written in the DM approach. When one state is occupied/unoccupied, the corresponding qubit is 1/0, respectively. In Fig. 5-5.1, a state $\Psi_{DM} = |o_1\alpha, o_1\beta, o_2\alpha, o_2\beta, o_3\alpha, o_4\alpha, o_5\beta, o_6\alpha, 0, 0\ldots\rangle_{DM}$ is mapped into the quantum register as $R_{DM} = |11110100\ldots, 11001000\ldots\rangle_{DM}$ in a DM manner. It is obvious that qubits in SCM can transform into DM by the feature of Fock space with initialized qubits in $|00\ldots\rangle$. Prepare R(SCM) in the quantum register,

$$R(\mathrm{SCM}) = (|00\rangle\otimes|0000\rangle\otimes|00\ldots\rangle)\otimes(|00\rangle\otimes|0010\rangle_{SCM}\otimes|00\ldots\rangle) \quad (5\text{-}5.1)$$

applying the CNOT gates to SOMOs,

$$R_1 = (|00\rangle\otimes|1101\rangle\otimes|00\ldots\rangle)\otimes(|00\rangle\otimes|0010\rangle_{SCM}\otimes|00\ldots\rangle) \quad (5\text{-}5.2)$$

and applying the NOT gates to doubly occupied orbitals,

$$R_{DM} = (|11\rangle\otimes|1101\rangle\otimes|00\ldots\rangle)\otimes(|11\rangle\otimes|0010\rangle_{SCM}\otimes|00\ldots\rangle) \quad (5\text{-}5.3)$$

then R_{DM} is obtained. The same approach is also possible when the wavefunction has a multi-determinant character.

5-5-2. Whole Procedure of the Quantum Algorithm of CSFs

The whole quantum algorithm of the CSF in SCM is described in Fig. 5-5.2. Since the transformation from SCM to DM is easy (in section 5-5-1), the algorithm is written in the SCM mapping in first. The next step is to apply quantum algorithm of spin eigenfunctions. It costs N_β for the NOT and Hadamard operations, and N_β^2 for the CNOT operations (see section 5-4-4). At the end of this procedure, the SCM wavefunction in CSF is conquered. Therefore, CSFs composed of the exponential number of deteminants can be prepared in polynomial time by QCs.

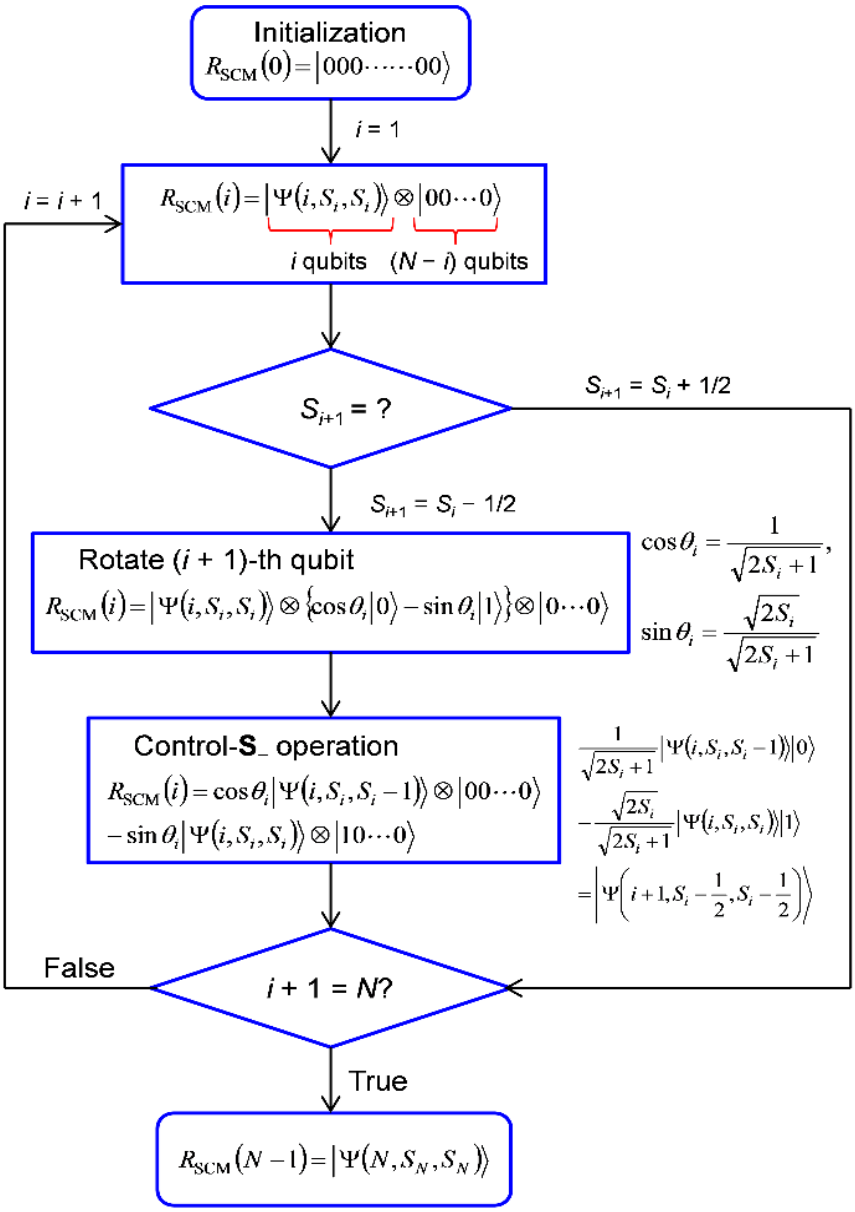

Figure 5-5-2.1. Scheme of quantum algorithm to compute CSF wavefunction of $\Psi_S(N, S, S)$. Due to S_- operators, the pathway is limited as described in subsection 5-4-3: Until $i = N - 1$, compute $S_{i+1} = S_i - 1$ if i is odd, $S_{i+1} = S_i + 1$ if i is even, and then compute $S_{i+1} = S_i + 1$ until $i + 1 = N$.

5-6. Conclusions

I have established one quantum algorithm to generate a CSF wavefunction as an approximate wavefunction of QCCs based on QPE. The quantum algorithm has two aspects: 1) superpolynomial property and 2) starting point of quantum chemical calculations. The former one indicates the fast computational ability in QCs and the latter one suggests a new paradigm in QCCs on QCs. As described in introduction, it is proven that the CSF wavefunction is the starting point of ab initio calculations on QCs because the approximate wavefunction is prepared as easily as the Hartree-Fock wavefunctions. In my prediction, the same computational difficulty both for open-shell and for closed-shell molecules in QCs is implied. Although the superpolynomial algorithm for QCCs on QCs is very few with proven computational speed, e.g. phase estimation algorithm and ours, the spin structures of molecules can play the significant role on this field in the near future. Thus, the construction of the CSF wavefunctions is one of the most fundamental problem in future quantum chemistry.

I have shown one result, but the unsolved problems are increased. First, there may be simpler algorithms to construct the CSF, i.e., the proven algorithm described above may not be optimized in terms of computational complexity. Second, it is unknown whether the CSF of the other pathways in branching diagram can be constructed in polynomial time or not. Furthermore, there is also fundamental problem whether one can compute the interactions between two CSFs efficiently on QCs or not. Those are the significant tasks related in fundamental theory for future QCCs on QCs.

5-7. References

[1] P. A. M. Dirac, *Proc. R. Soc. London, Ser. A*, **1929**, *123*, 714-733.

[2] S. R. White, R. L. Martin, *J. Chem. Phys.*, **1999**, *110*, 4127-4130; S. Wouters, D. Van Neck, *Eur. Phys. J. D*, **2014**, *68*, 272.

[3] H. Nakatsuji, *Phys. Rev. Lett*., **2004**, *93*, 030403; H. Nakatsuji, H. Nakashima, *TSUBAME e-Science J.*, **2014**, *11*, 8-13.

[4] R. P. Feynman, *Int. J. Theor. Phys.*, **1982**, *21*, 467-488.

[5] A. Aspuru-Guzik, A. D. Dutoi, P. Love, M. Head-Gordon, *Science*, **2005**, *309*, 1704-1707.

[6] D. S. Abrams, S. Lloyd, *Phys. Rev. Lett.*, **1997**, *79*, 2586-2589; D. S. Abrams, S. Lloyd, *Phys. Rev. Lett.*, **1999**, *83*, 5162-5165.

[7] B. P. Lanyon, J. D. Whitfield, G. G. Gillet, M. E. Goggin, M. P. Almeida, I. Kassal, J. D. Biamonte, M. Mohseni, B. J. Powell, M. Barbieri, A. Aspuru-Guzik, A. G. White. *Nat. Chem*., **2010**, *2*, 106–111.

[8] J. Du, N. Xu, X. Peng, P. Wang, S. Wu, D. Lu, *Phys. Rev. Lett*., **2010**, *104*, 030502.

[9] L. Veis, J. Pittner, *J. Chem. Phys*., **2010**, *133*, 194106; L. Veis, J. Višňák, T. Fleig, S. Knecht, T. Saue, L. Visscher, J. Pittner, *Phys. Rev. A*, **2012**, *85*, 030304; J. T. Seeley, M. J. Richard, P. J. Love, arXiv:1208.5986; N. Cody Jones, J. D Whitfield, P. L. McMahon, M-H. Yung, R. Van Meter, A. Aspuru-Guzik and Y. Yamamoto. *New J. Phys*., **2012**, *14*, 115023; B. Toloui, P. Love, arXiv:1312.2579; D. Wecker, B. Bauer, B. K. Clerk, M. B. Hastings, M. Troyer, *Phys. Rev. A*, **2014**, *90*, 022305. A. Peruzzo, J. McClean, P. Shadbolt, M-H. Yung, X-Q. Zhou, P. J. Love, A. Aspuru-Guzik, J. L. O'Brien, *Nat. Comm*., **2014**, *5*, 4213; J. R. McClean, R. Babbush, P. R. Love, A. Aspuru-Guzik, *J. Phys. Chem. Lett.*, **2014**, *5*, 4368-4380; R. Babbush, P. R. Love, A. Aspuru-Guzik, *Sci. Rep*., **2014**, *4*, 6603; R. Babbush, J. McClean, D. Wecker, A. Aspuru-Guzik, N. Wiebe, *Phys. Rev. A*, **2015**, *91*, 022311.

[10] G. W. Jr. Pratt, *Phys. Rev*. **1953**, *92*, 278-288.

[11] R. Sessoli, D. Gatteschi, A. Caneschi, M. A. Novak, *Nature*, **1993**, *365*, 141-143.

[12] R. Pauncz, *The construction of spin eigenfunctions. An exercise book*, Kluwer Academic/Plenum Publishers, **2000**.

Appendix (Abbreviation List)

Abbreviations	Descriptions (Chapter)
A	A-tensor: hyperfine coupling (2, 3, 4)
AQC	Adiabatic Quantum Computer (3)
AQUA	Adiabatic QUantum Algorithm (3)
B_0, B_z	Static magnetic field strength in ESR (3, 4)
BQP	Bounded-error Quantum Polynomial time (3, 5)
CAS-CI	Complete Active Space Configuration Interaction (5)
CC	Classical Computer (3, 4, 5)
CNOT	Controlled NOT (3, 4, 5)
CPW	Co-Planar Waveguide (1)
CSF	Configuration State Function (5)
D	D-tensor: zero field splitting/fine structure coupling (2, 3, 4)
DEER	Double Electron-Electron Resonance (2)
DM	Direct Mapping (5)
DMRG	Density Matrix Renormalization Group (5)
DPNO	DiPhenylNitrOxide (1)
ELDOR	Electron Double Resonance (2)
ENDOR	Electron Nuclear DOuble Resonance (1)
ESR	Electron Spin Resonance (2, 3, 4, 5)
F, f	Fidelity: success probability of quantum operations (3, 4)
FA	Floquet Approach (3)
FCI	Full Configuration Interaction (5)
g	g-tensor (2, 3, 4)
GB/SA	Generalized Born/Surface Area (2)
GRAPE	Gradient Ascent Pulse Engineering (4)
Group X (X = A, B, C)	Abandoned structure group composed of several types of spin-labeled DNAs (2)
$\widehat{H}_{\mathrm{f}}$	Final Hamiltonian in an adiabatic path (3)
$\widehat{H}_{\mathrm{i}}$	Initial Hamiltonian in an adiabatic path (3)
$\widehat{H}_{\mathrm{MSQC}}$	Spin Hamiltonian of MSQC (3, 4)
J	J-tensor: exchange coupling (3)
KHM	potassium Hydrogen Maleate (4)
LLMOD	Large-scale-Low MODe sampling (2)

MAXCUT	MAXimum CUT (1)
MCMM	Monte Carlo Multiple Minimum (2)
MM	Molecular Mechanics (2)
MMFF	Merk Molecular Force Field (2)
MSQC	Molecular Spin Quantum Computer (2, 3, 4, 5)
NA	Naphyridine-Azaquinolone (2)
NCD	Naphthyridine Carbamate Dimer (2)
NMR	Nuclear Magnetic Resonance (2, 3, 4)
NN	Nitronyl Nitroxide (2)
NP	Non-deterministic Polynomial time (3, 5)
O_S	Lowdin's projection operator (5)
PELDOR	Pulsed ELDOR (Electron Double Resonance) (2)
QC	Quantum Computer (2, 3, 4, 5)
QCC	Quantum Chemical Calculation (5)
QCCs on QCs	Quantum Chemical Calculations on Quantum Computers (5)
QIP	Quantum Information Processing (2, 3, 4, 5)
QPE	Quantum Phase Estimation (5)
RMSD	Root-Mean-Squares Deviation (2)
SAA	Secular Averaging Approach (3, 4)
SCM	Spin Coordinate Mapping (5)
SU(N)	Special unitary group of N dimension (4, 5)
SWAP	A gate swaps two qubits (4)
TEMPO	Tetramethylpiperidine (2)
TNCG	Truncated Newton Conjugate Gradient (2)
TWT	Traveling Wave Tube (2)
Type A	A minor structure type with 6-7 nm spin distances (2)
Type B	A abandoned structure type with strong steric repulsion (2)
Type C	A major structure type around 5 nm spin distances (2)
Type D	A major structure type around 5 nm spin distances (2)
Type E	A abandoned/minor structure type due to 3 nm spin distances (2)
Type X (X = A, B, C, D, E)	A structure type of spin-labeled DNAs (2)
U	A unitary operator in time evolution (3, 4)
UQG	Universal Quantum Gate (2, 3, 4, 5)
X_f	A conformational searched structure of type X (2)
X_i	An initial structure of type X (2)

β_e	Bohr magneton (3, 4)
β_n	Nuclear magneton (3, 4)
Ψ_{DM}	Wavefunction in DM (5)
$\Psi_S(N, S, Ms)$	Spin eigenfunction (5)
Ψ_{SCM}	Wavefunction in SCM (5)
ω_0	Larmor angular frequency of each spin in ESR (3, 4)
ω_1	Rabi (control) angular frequency of each spin in ESR (3, 4)
ω_{MW}	Microwave angular frequency in ESR (4)

Concluding Remarks

The author has investigated MSQCs in terms of molecular structures, experimental methods for adiabatic quantum computing, molecular design for numerical pulses and a new quantum algorithm. In chapter 2, steric structures of spin-labeled DNA duplex were studied, in which the control of orientations about attached spin sources were significant in applications for MSQCs. By the virtue of MM calculations, the attached four spin sites can be controlled individually because of the different orientations of the radical moieties, and the orientations should be manipulated with a more sophisticated manner toward 1D-QCs such as Lloyd model QCs.

The two studies in chapter 3 and 4 are related to spin control properties of open-shell molecules. In chapter 3, the procedure to perform AQCs by MSQCs was investigated under the assumption of SAA, where the pulse sequences were calculated by analytical techniques. MSQCs composed of both electrons only and electrons with nuclei have capacity to scale up the computational speed from NMR-QCs in AQCs. However, pulse intervals in analytical sequences can be too short to perform the practical QC experiments from the view point of both experimental restrictions and SAA theory. The solution was suggested by numerical simulations. By modifying Trotter decompositions, the pulse intervals can be increased proportional to required time, i.e. computational time. Although the computational speed is sacrificed, the method surely relaxes experimental restrictions and matches theoretical assumptions. Excepting the relaxation picture, the author has proven the pulse sequences and analytical calculation methods to AQCs by MSQCs.

In chapter 4, the author has established molecular design toward indirect spin manipulations of nuclei by MSQCs. In this calculation, two nuclear spins of a potassium hydrogen maleate (KHM) radical and a ^{13}C- labeled malonyl radical are controlled via one electron by microwave. As a result, two objectives for the molecular design are suggested. (1) Heteronuclear spin systems are easy to control by the numerical pulses. In homonuclear systems, the large difference in principal values of hyperfine tensors can decline the disadvantage. (2) Large anisotropy and coaxial property of hyperfine tensors make a system control fast. Since both conditions are directly connected to the controllability, it is proven that the control difficulty is interpreted by controllability of the molecular system.

A quantum algorithm to generate CSFs is investigated for QCCs on QCs. In chapter 5, the author has suggested that the quantum algorithm has a superpolynomial property and is possible to compute the exponential number of Slater determinants in polynomial time. The CSFs in QCs are wavefunctions easy to prepare in open-shell molecules replacing Hatree-Fock wavefunctions.

The author has investigated MSQCs with various theoretical points of view in this dissertation. Theory in chemistry, physics and mathematics is applied to MSQCs for molecular designs (chapters 2, 3 and 4), control properties by ESR (chapters 3 and 4) and complexity of quantum algorithms

(chapters 5). Concerning experimental difficulties, the new quantum algorithm described in chapter 5 is significantly easy to implement among quantum algorithm of QCCs on QCs. As discussed in those chapters, the development of theory can help experiments and solves fundamental problems in quantum computing.

January, 2016

Satoru Yamamoto

Acknowledgments

The author should thank for many people who have been supported the work and life. First, the author would like to express his supervisor Prof. Kazunobu Sato. He has been supported his academic life and given discussions and advice from the experimental point of view. The author also expresses his gratitude for Prof. Takeji Takui who have taught the author well at experimental and historical science and the researching manner. Research collaborators, Associated Professor Shigeaki Nakazawa, Aassociated Professor Kenji Sugisaki and Mr. Taiki Shibata are mercy men who were directly supported the author's work and shared long time with the author.

Outside the university, the author has grateful thanks to the sample provider Prof. Kazuhiko Nakatani, Dr. Kensuke Maekawa (Osaka University) and Dr. Hiroshi Atsumi (Massachusetts Institute of Technology). In study abroad program, Prof. Olav Schiemann, Assistant Professor Hideto Matsuoka and Mr. Andreas Berndnaeuser in Bonn university and Dr. Daniel Burgarth gives guidance to the author very well. The author thanks them for the lecture of researching field (synthetic organic chemistry, mathematics and theoretical physics), English language and European culture.

The author is very grateful to Associate Professor Daisuke Shiomi, Lecturer Kazuo Toyota, Lecturer Koji Maruyama, Dr. Kenji Sugisaki, Dr. Yuki Kanzaki and Dr. Shinsuke Hayashi (Osaka City University) for their invaluable discussions and advice. In addition author is also grateful to the members of Professor Sato's research group; Dr. Tomohiro Yoshino, Dr. Kazuki Ayabe, Mr. Mikito Nozaki, Ms. Ayaka Tanaka, Mr. Yusuke Taniji, Mr. Takeshi Yamane for their valuable discussions, encouragement and academic life. The author is also extremely thankful to the entire staffs and faculty of the chemistry department, Graduate School of Science of Osaka City University for providing their professional support and sharing their knowledge.

The author acknowledges financial support of scholarship from Graduate School of Science, Osaka City University for students in the doctorial course, and study abroad program of JASSO and Prof. Yoshihiro Ohnita.

Finally, the author deeply appreciates his family for their support, encouragement and patience during the study.